POLITECNICO
MILANO 1863

SCUOLA DI INGEGNERIA INDUSTRIALE
E DELL'INFORMAZIONE

Toward operando NMR studies of SEI in lithium ion batteries

Tesi di Laurea Magistrale in
Engineering Physics- Ingegneria Fisica

Author: **Samuele Comizzoli**

Student ID: 225555
Advisor: Prof. Rafael Omar Ferragut
Co-advisors: Dr. Katharina Märker
Academic Year: 2023-2024

Dedicated to Francesco
D'altronde il biliardo è anche questo.

Abstract

The Solid Electrolyte Interphase (SEI) is a crucial element for the stability and performance of lithium-ion batteries, but its characterization remains challenging due to its complex nature and the very small quantity in which it is present. Operando NMR spectroscopy emerges as an innovative technique for monitoring the formation and evolution of the SEI in real-time without interrupting the battery's operation. However, its application to lithium batteries is still in its early stages and requires optimizing dedicated probes and advanced experimental strategies. This thesis explores the potential of ex situ NMR spectroscopy in studying the SEI, particularly focusing on silicon anodes, which, due to their cyclic volumetric expansions, allow the accumulation of significant amounts of SEI for detailed analysis. A key aspect is the use of $^{1}H-^{7}Li$ cross-polarization to selectively detect the organic components of the SEI, overcoming challenges related to its low quantity and signal overlap. Compared to other operando characterization techniques like XPS or Raman spectroscopy, NMR offers the advantage of being non-destructive, providing detailed information about the local chemistry without altering the material structure. Additionally, unlike XRD, NMR is particularly sensitive to amorphous materials like the SEI. Thanks to its ability to detect nuclei specifically without the need invasive treatments, NMR represents one of the most promising methods for studying the SEI under realistic conditions. As a future evolution of this approach, the introduction of ^{19}F spectral measurements is anticipated for monitoring inorganic species, further expanding the potential of NMR in operando SEI characterization. The experimental approach developed represents a first step toward operando NMR experiments with double-channel probes, opening new prospects for the design of electrolytes and SEI stabilization strategies, with the aim of improving life and efficiency of lithium-ion batteries.

Keywords: SEI; NMR; batteries; cross-polarization; silicon

Abstract in lingua italiana

La Solid Electrolyte Interphase (SEI) è un elemento cruciale per la stabilità e le prestazioni delle batterie a ioni di litio, ma la sua caratterizzazione rimane una sfida a causa della sua natura complessa e della quantità ridotta in cui è presente. La spettroscopia NMR in operando emerge come una tecnica innovativa per monitorare in tempo reale la formazione e l'evoluzione della SEI senza interrompere il funzionamento della batteria. Tuttavia, la sua applicazione alle batterie al litio è ancora agli albori e richiede l'ottimizzazione di sonde dedicate e strategie sperimentali avanzate. Questa tesi esplora le potenzialità della spettroscopia NMR ex-situ nello studio della SEI, concentrandosi sugli anodi di silicio, che, grazie alle espansioni volumetriche cicliche, permettono l'accumulo di una quantità significativa di SEI per analisi dettagliate. Un aspetto chiave è l'uso della cross-polarizzazione $^{1}H -^{7} Li$ per la rilevazione selettiva dei componenti organici della SEI, superando le difficoltà legate alla scarsa quantità di SEI e alla sovrapposizione dei segnali negli spettri. Rispetto ad altre tecniche di caratterizzazione in operando, come la spettroscopia XPS o Raman, l'NMR offre il vantaggio di essere una tecnica non distruttiva e capace di fornire informazioni dettagliate sulla composizione chimica senza alterare la struttura del materiale analizzato. Inoltre, a differenza della diffrazione XRD, l'NMR è sensibile ai materiali amorfi, come la SEI. Grazie alla sua capacità di rilevare specificamente i nuclei senza necessità di trattamenti invasivi, l'NMR rappresenta una delle metodologie più promettenti per lo studio della SEI in condizioni realistiche. Come futura evoluzione, si prevede di introdurre la misurazione degli spettri ^{19}F per monitorare le specie inorganiche, ampliando ulteriormente il potenziale dell'NMR nella caratterizzazione della SEI. L'approccio sviluppato rappresenta un primo passo verso esperimenti NMR in operando con sonde a doppio canale, aprendo nuove prospettive per la progettazione di elettroliti e strategie di stabilizzazione della SEI, con l'obiettivo di migliorare la vita e l'efficienza delle batterie a ioni di litio.

Parole chiave: SEI; NMR; batterie, cross-polarizzazione, silicio

Contents

1 | Introduction

1.1. Introduction

The 20th century has been characterized by significant progress, largely driven by the widespread use of fossil fuels as an affordable energy source. However, these advances have come at the cost of environmental degradation, contributing to global warming and its potentially devastating consequences. As a result, climate change has become a top priority on the political agenda in Europe and worldwide. To mitigate its impact, governments have committed to reduce their carbon footprint, identified as a key factor in this process. According to the Paris Climate Agreement, achieving the targeted 50% reduction in CO_2 emissions by 2030, necessitates a complete transformation of the energy production landscape [73]. A shift toward renewable energy sources and electric vehicles is essential to replace most fossil fuel-based technologies. However, this transition is a complex and time-consuming process that requires strong dedication, as modern society is strongly reliant on the conveniences provided by fossil fuels. Meanwhile, the continuous growth of the global population, coupled with rapidly evolving lifestyles, continues to increase the energy demand [22]. Although renewable energy sources are attractive, they face a significant challenge due to their dependence on meteorological conditions. Electricity generation occurs mainly during specific periods when weather conditions are favorable. Therefore, the achievement of climate targets is closely connected to advancements in existing energy storage technologies or the development of new solutions [77]. Various energy storage techniques have been developed and optimized based on their specific applications. Figure 1.1 illustrates a Ragone plot comparing different energy storage systems. The horizontal axis represents energy density, indicating the amount of energy that a given volume of active materials can store, while the vertical axis represents power density, measuring how quickly energy can be delivered. At the two extremes are capacitors and fuel cells: capacitors provide high power but have limited energy storage capacity, whereas fuel cells can store large amounts of energy but cannot release it on a fast time scale. Among the available options, Li-ion batteries offer a trade-off between these two properties. Additionally, they are characterized by high energy efficiency, low

self-discharge rate, and no memory effect.

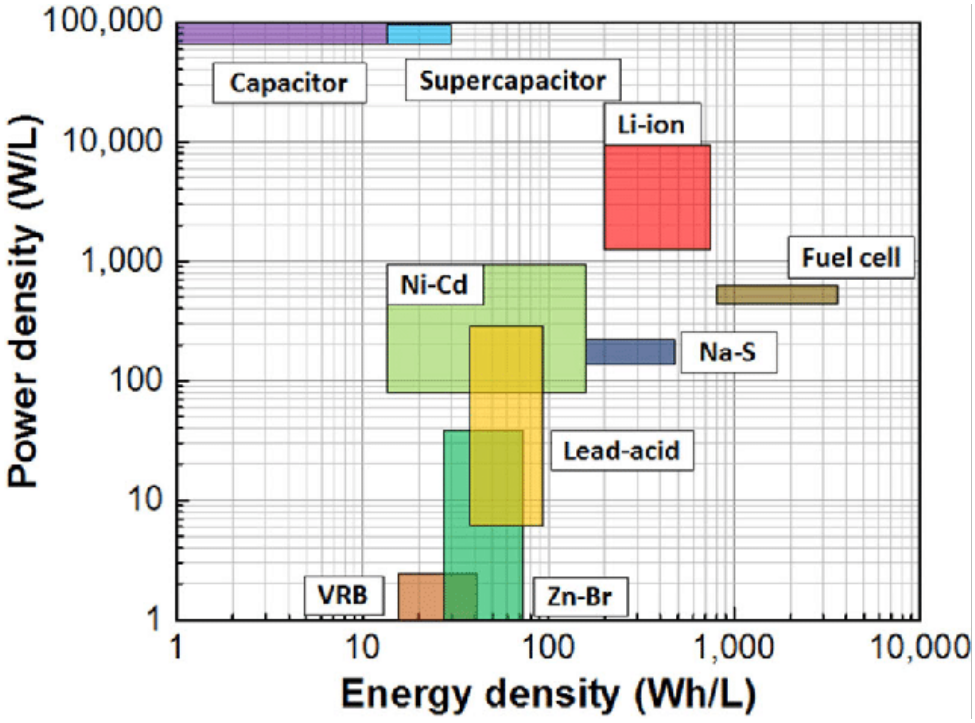

Figure 1.1: Ragone plot for energy storage systems [52].

The first non-rechargeable lithium-ion battery was created in the early 1970s [61]. Being one of the lightest elements, lithium provides the highest energy density per unit volume, allowing for large storage capacities in compact sizes. In the late 70s of the last century, M. Stanley Whittingham introduced the idea of a lithium-based rechargeable battery [63]. However, due to safety concerns, the chosen approach failed and research moved away from using metallic lithium as an electrode itself [6]. Finally, Sony introduced the first commercial lithium ion battery (LIB) in 1991 [20], choosing graphite and lithium cobalt oxide ($LiCoO_2$) as electrodes. Originally, the applications were limited to small electronic devices, but today they range from portable electronics like laptops and smartphones to large-scale electric vehicles and power grids. The global market for Li-ion batteries is projected to reach $107.6 billion by 2025, primarily guided by the rising demand for plug-in vehicles and the expanding use of automation and battery-powered industrial machinery [41]. Among all industrial field Lithium-ion batteries have become a key technology in the automotive sector. The widespread adoption of electric vehicles (EVs) will represent a solution for greenhouse gas reduction and contribute to a cleaner energy future. However, to compete with traditional internal combustion engine (ICE) vehicles and achieve broad market acceptance, several obstacles remain. Larger, lower cost, batteries with higher energy density are essential to meet consumer demands. A major challenge is the

significantly longer charging times of electric vehicles compared to the quick refueling of internal combustion vehicles, which hinders the widespread acceptance of electrified vehicles. To address this issue and remain competitive in the automotive market, EVs must be able to charge in a time comparable to the refueling of an ICE vehicle [31]. To reach this objective, the selection of materials for LIBs must be optimized. Specifically, active materials for both anodes and cathodes that enable batteries with high energy density and high specific energy are needed, allowing for more batteries to be packed into a given volume while minimizing the battery overall mass.

1.2. Working principles of Li-ion batteries

Lithium is a monovalent ion, which represents the smallest charge an ion can possess. However, its diffusion rate is considerably higher than that of multivalent ions or other alkali metals, owing to its small ionic radius and much lower mass (e.g., >3x smaller than Na^+ or Mg^{2+}, >6x smaller than K^+ or Ca^{a+}). Lithium is also advantageous because of its low reduction potential, which is lowest among all metals, enabling LIBs with high voltages. These factors are the main reasons why LIBs are characterized gravimetric and volumetric energy, and power density [47]. Each electrochemical cell in a modern LIB consists of the following main components depicted in Figure 1.2: two electrodes (anode and cathode), electrolyte, separator, and an external circuit connected to the electrodes via current collectors. Additional components such as polymeric binders or carbon black are neglected here for simplicity. The former is typically used to keep the active materials together, while the latter acts as conductive filler material [50]. The electrolyte represents an ionic carrier for Li ions between the anode and cathode without giving any contribution to the actual electrochemical reactions. The separator is permeable for the Li ions, while it blocks electrons and therefore prevents short-circuit between the electrodes [9]. At the beginning of the cell operation, the anode is fully lithiated, meaning that all active Li ions are sitting inside the anode. During discharge, positively charged Li ions (Li^+) generated from an oxidation process travel from the anode to the cathode through the electrolyte. Once Li ions reach the counter electrode, they recombine through a reduction reaction with the electrons, which were simultaneously flowing through the external circuit during Li ions diffusion via the electrolyte. This electron flow is the responsible of the necessary electrical energy to power any device. The driving force of the whole mechanism is the chemical potential difference between the two electrodes. Once the equilibrium condition is reached, and the cathode is then fully lithiated, the flow stops and the battery is "empty". During the charge, an externally applied voltage forces the opposite movement of both Li ions and electrons. Consequently, the anode is refilled, the potential difference

restored, and energy accumulated. Obviously, for this process to work, the two electrodes must be made of materials that can capture lithium so that Li^+ can move in and out.

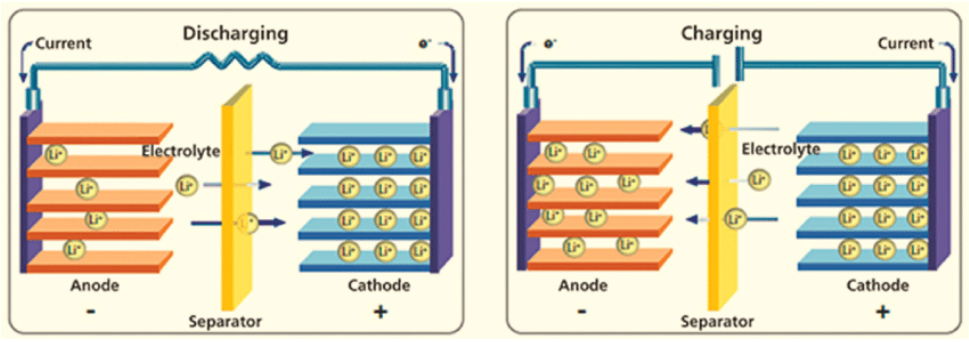

Figure 1.2: Working principles of Li-ion batteries during discharge and charge [4].

Three main mechanisms of Li insertion have been identified: intercalation, alloying, and conversion. Each of them depends on the structure of the electrode [70]. Intercalation happens if unfilled vacancies are present and can be occupied by Li ions without changing the host material form the chemical point of view (Figure 1.3a). Alloying implies that the inserted Li ion directly bonds to the host material and creates a new alloy in the process, typically involving a volume expansion (Figure 1.3b). The last reaction is conversion, where the inserted lithium splits up a binary compound MX (M is a transition metal) and reduces M to M_0, while forming LiX at the same time (Figure 1.3c) [72].

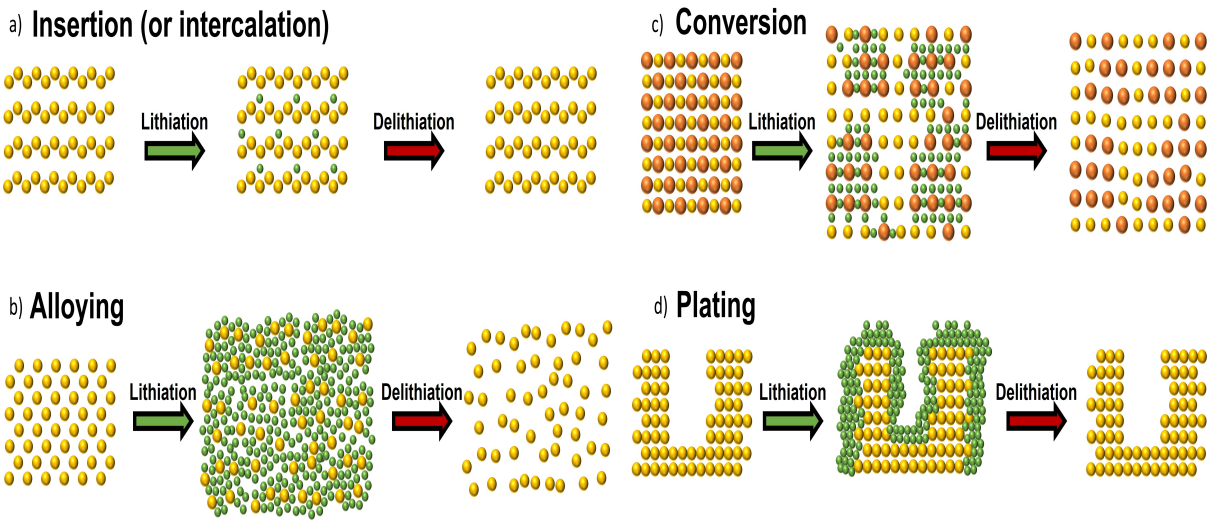

Figure 1.3: Lithiation mechanisms for (a) intercalation, (b) alloying, (c) conversion electrodes and d)plating [23].

1.2.1. Key aspects for performances

Electrodes in a battery define the identity of the redox reaction. In particular, electrode materials choice and design have to be properly chosen such that the listed performance requirements are fulfilled

- Electrode kinetics: insertion and removal of lithium should be fast allowing high rate capabilities. This requires that both ionic and electronic conductivities must be high. This is achievable by using nanostructured electrodes which increase the effective area of reaction and facilitate Li ions bulk diffusion;
- Free energy of reaction: reactions with large driving force translates to higher voltage and energy density. On the other hand, electrode materials have to be selected in order to face electrochemical stability associated to the electrolyte.
- Capacity: the amount of lithium stored in the electrodes must be maximized.
- Cyclability: electrode lithiation and delithiation introduces volume expansions that results in undesired stress which strains the electrode material and leads to performance degradation after repeated cycling.
- Scalabilty and cost: material costs should be low in order to compete with other technologies and be scalable to enable price reduction by high-throughput manufacturing.
- Safety and stability: the battery is expected to be stable under anticipated operating conditions

1.2.2. Cathodes

For lithium ion batteries, the cathode represents the positive electrode that hosts lithium ions from the anode.Three main families of cathode compounds can be identified: layer, spinel and olivine. Layered oxides like $LiCoO$, represent a well established solution and offer an operating voltage of about 4 volts versus Li/Li^+ [64], [59] (Figure 1.4). Layered oxides operate like a multiple-story parking lot, where lithium is packed into the parking spaces between the "concrete" layers that represent the redox-active transition metals. While $LiCoO_2$ is the standard cathode material of choice, research into higher voltage cathodes is on progress. One example of spinel is $LiMn_{1.5}Ni_{0.5}O_4$. It offers a flat operating potential at 4.8V vs Li/Li^+ due to the Ni_{2+}/Ni^{4+} transition, moderate capacity (147 Ahg^{-1} theoretical), and good rate capabilities due to its stable spinel structure [54], [75]. Finally, another important cathode is $xLi_2MnO_3+(1-x)LiMn_{0.33}Ni_{0.33}Co_{0.33}0_2$

which shows reasonable capacities of over 200 Ahg^{-1} . However, these cathodes both suffer from a reduction in lithiation voltage with extended cycling meaning lower operating voltage over cycles [76]. Stabilization of high capacity cathodes has focused on using nanostructured engineered coatings, core-shell particles, and careful selection of composition to balance capacity with stability [58]. By combining cathodes and anodes with a compatible electrolyte, a full Li-ion battery can be assembled. Currently, at least three types of Li-ion batteries have been developed for different applications summarized below in Figure 1.4.

High energy density (150–210 W h kg^{-1})	$LiCoO_2$ $LiNi_{1/3}Co_{1/3}Mn_{1/3}O_2$	Si, Sn graphite
High power density (1000–4000 W kg^{-1})	$LiMn_2O_4$ $LiFePO_4$	Hard carbon graphite
Long cycle life (3000–10000 cycles)	$LiFePO_4$	$Li_4Ti_5O_{12}$ graphite

Figure 1.4: Typical cathode/anode electrode combinations used in lithium ion batteries based on application [78].

1.2.3. Anodes

Graphite has been the preferred material for the negative electrode and still remains the primary anode material in commercial Li-ion batteries. While this study focuses on silicon, it is essential to compare and emphasize the key differences between these anode materials. Graphite is lithiated via an intercalation mechanism, to LiC_6 where Li ions lie within spaces between the sheets of graphene. During lithiation the maximum volume expansion is small ($\sim$ 13%), making this material mechanically stabile and able to mitigate cracking of the electrode surface during cycling [53]. This mechanism can sustain remarkable capacity retention over many cycles, but the number of intercalation sites for, Li ions within the host lattice is low. Indeed, intercalation reaction occurs preferentially at the edge planes of the graphite particles, as opposed to basal planes that form most of the area of the flake-like graphite particles [38]. At low C-rates (applied currents to the cell), the intercalation mechanism has proven to be sufficient, however in fast-charging regime (high C-rates), lithium can plate onto the surface instead of diffuse into the material. At high currents, lithium ions will accumulate on the surface of the anode instead of intercalating into the material. Under this circumstances, the flux of ions diffusing in the electrode is too slow compared to the flux of ions arriving on the electrode surface. Diffusion is then "bottleneck" from the kinetics point of view. The irreversibly plated lithium

can cause major technical risks, such as increased cell resistance, electrolyte degradation and loss of active Li ions resulting in capacity fade [19]. Consequently, because of the slow graphite intercalation mechanism, low specific capacity and lack of performance during fast charging other materials with higher capacity and better fast charging capabilities are of greater interest for LIBs.

An ideal anode for Li-ion batteries is pure lithium metal, which offers a high specific capacity of about 3860 $mAhg^{-1}$ [7]. Nevertheless, issues associated to electrolyte reactivity, dendrite formation during cycling, and battery safety have restricted the use of pure lithium metal in modern batteries. Consequently, the pursuit of safer alternatives to lithium, while offering higher capacities than carbon, has led researchers to explore various anode materials, including group IV elements such as silicon, germanium, and tin.

Silicon is a material of interest because of its extremely high gravimetric (3572 $mAhg^{-1}$) and volumetric (8322 $mAhcm^{-3}$) capacities, ten times that of graphite [16]. Its increased energy density makes it an ideal material for LIBs. In contrast to graphite, silicon undergoes an alloying mechanism, where lithium insertion involves the breaking and reformation of bonds within the host structure, rather than a reversible intercalation process. During electrochemical cycling, silicon forms alloys with lithium, leading to structural expansion, which contribute to its high volumetric and gravimetric capacities [40], [79]. This volume expansion turns out to be a major drawback of silicon anode materials as the dramatic change, up to 300% upon lithiation, causes the electrode to lose its structural integrity. During cycling a phase change in the silicon material from crystalline to amorphous occurs when the most lithiated state ($Li_{15}Si_4$) is reached at the top of charge leading to a stoichiometry of 3.75 lithium per one silicon atom. The reverse is also true during the discharge process. The $Li_{15}Si_4$ crystalline phase is transformed into an amorphous lithium silicide (a-Li_xSi) during discharge, decreasing the lithium content in the silicon material. During the alloying mechanism many different Li_xSi phases can form such as $Li_{12}Si_7$, Li_7Si_3, $Li_{13}Si_4$, $Li_{15}Si_4$ and $Li_{21}Si_5$ as reported in Figure 1.5. On top of all, the $Li_{15}Si_4$ phase is the most electrochemically lithiated phase that can be obtained, limiting the practically achievable capacity to 3578 $mAhg^{-1}$. In $Li_{15}Si_4$ crystalline phase, 15:4 ratio of Li:Si leads to the build up of huge stress on the Si particles resulting in cracking at the surface. This brings to direct exposure of the electrolyte to the strongly reducing anode, causing the degradation of the reduction of the former. During electrolyte reduction, Li ions are irreversibly consumed resulting in subsequent loss of capacity. As the LIB is charged and discharged the repetitive volume expansion/contraction bring to

repeated exposure of the electrolyte to fresh, uncoated anode surface leading to thickening of the SEI layer. Such volume expansion also has the effect of dirsrupt the conductive network between silicon particles provided by the addition of binder and active to the anode material. If this happens anode particles become isolated and current collection at the anode will inevitably worsen.

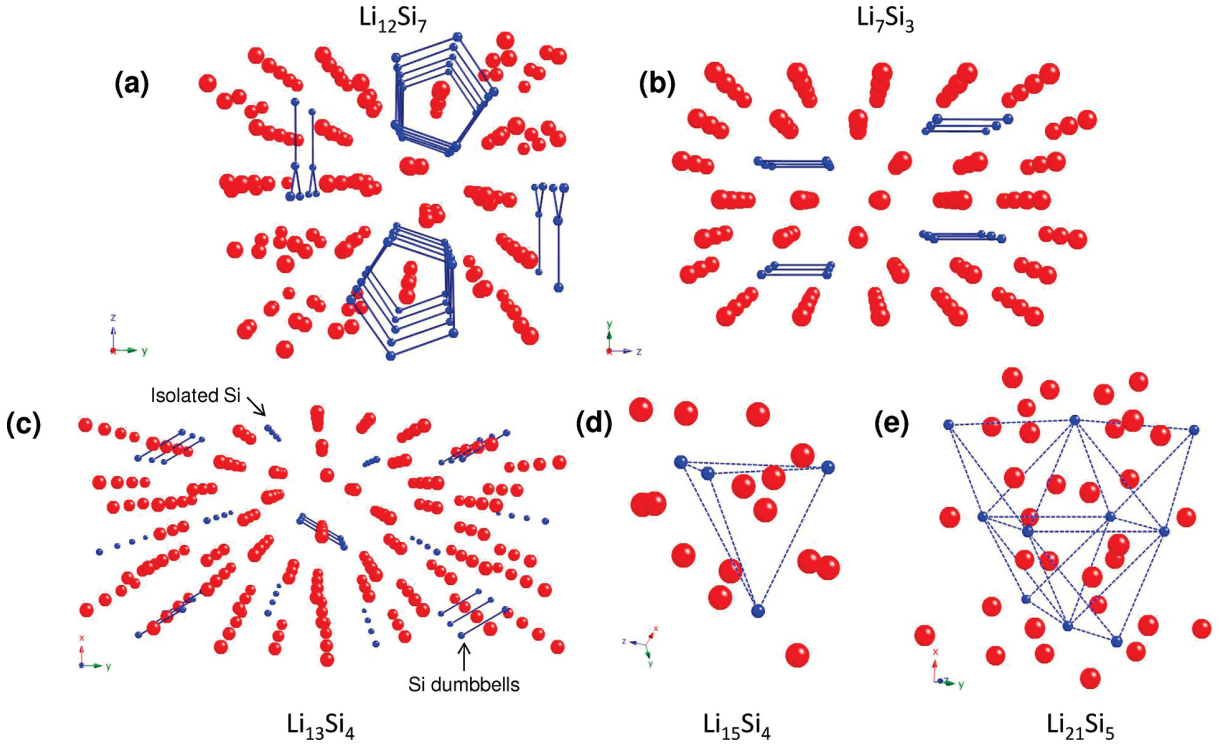

Figure 1.5: Structural representation of the different Li_xSi crystallographic phases (a)$Li_{12}Si_7$, b) Li_7Si_3, c) $Li_{13}Si_4$, d) $Li_{15}Si_4$ and e) $Li_{21}Si_5$). Lithium and silicon atoms are shown in red and blue respectively. The blue lines indicate Si – Si bonds while the blue dashed lines inidicate the closest Si – Si distances $>$ 3.0 Å [15].

Changing the electrochemical cycling parameters to limit the voltage window (to avoid the formation of $Li_{15}Si_4$ phase) [12], adding nano-sized silicon particles [65], [49], and optimizing different binder materials/electrolyte additives are all areas of study for the optimization of silicon anodes [28], [62].

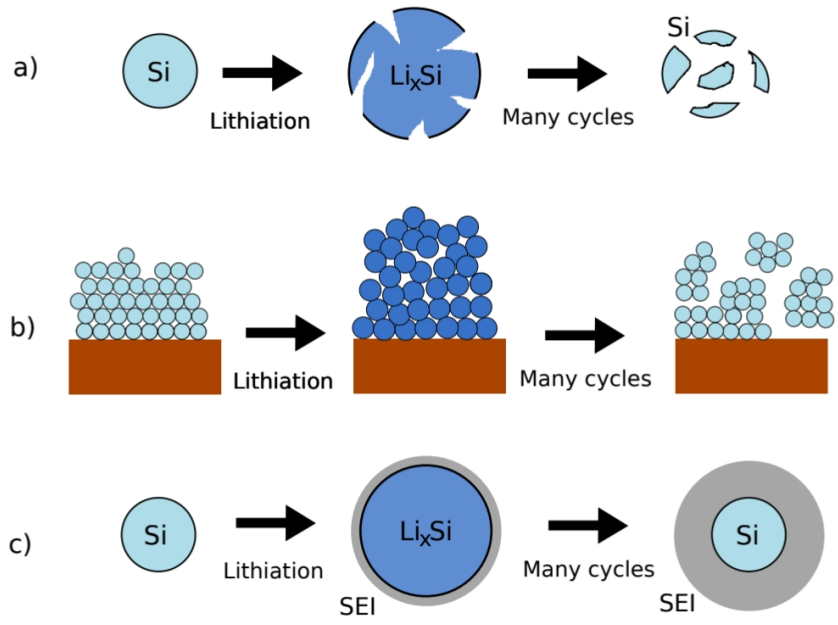

Figure 1.6: Illustration of the material challenges related to the large volume change in Si anodes; a) material pulverization, b) morphology and volume change of the whole electrode, c) unstable solid electrolyte interphase [48].

Considerable effort has been put in studying nanoscale and nanostructured electrode materials as a means to improve the cycle life. The increased surface area per unit volume and smaller dimensions allow nanoscale materials to easily accommodate lithium minimizing internal strain. This approach has been applied to lithium alloying anodes as silicon [10], germanium [11] and tin [60], [1]. For silicon, studies using nanopowders ($<$ 100 nm) showed reversible capacities of 1730 Ahg^{-1} after 10 cycles [25]. Powdered anodes are produced by mixing a binder such as polyvinylidene fluoride, a conductive additive like carbon, and an organic solvent to make a slurry which is then deposited onto a metal current collector (usually copper). In contrast to bulk materials, nanoscale materials have a lower packing density and are characterized by a more porous structure, which can face the significant volume expansions that occur during lithiation. In addition, the shorter electron and lithium ion path lengths allows for higher sustained charge/discharge rates. Another advantage of nanoscale materials is that their time for diffusion is short given their small dimensions. In bulk electrodes slow solid-state kinetics causes gradients in lithium concentration, whose in turn produce gradients in strain. Conversely, in nanoscale materials, shorter diffusion path and increased surface area allow for a more uniform lithiation and thus are less likely to create strain unbalances.

1.2.4. Electrolyte

The electrolyte acts as a bridge that lithium ions transverse during electrochemical cycling. The electrons, in contrast, are unable to cross it through due to its high electronic resistivity and are consequently forced to move through the external circuit.
In the case of lithium ion batteries, the Li_+ ion is ideally the only ion traversing the electrolyte. In addition to high ionic conductivity, the electrolyte needs to have close contact with the electrodes to ensure a suitable electrolyte-electrode interface that is favorable for charge transfer [68]. While liquid electrolyte can wet complex electrode geometries, solid state electrolytes cannot and thus must be designed carefully. Electrolytes undergoes redox reactions with the electrodes due to the highly oxidizing conditions at the cathode and the strongly reducing conditions at the anode. This effect worsens when using high surface area nanostructured electrodes due to the higher reactivity associated to the wider reactive surface [71]. To control electrolyte reduction, choosing an appropriate electrolyte is important. Electrodes are by their electrochemical potentials μ_A (anode) and μ_C (cathode), which are equal to their Fermi energies (Figure 1.7). If μ_A is above the lowest unoccupied molecular orbital (LUMO) of the electrolyte, the anode will reduce the electrolyte. This reduction decomposes the electrolyte unless a passivating layer, referred to as the solid electrolyte interphase (SEI) layer, forms [2]. According to this model, SEI introduces an energetic barrier preventing further electrons migration from the anode to the electrolyte. Growth of the SEI generally stops after a few cycles once the anode surface is passivated, resulting in stable battery performance. Similarly, if μ_C lies below the highest occupied molecular orbital (HOMO) of the electrolyte, the cathode will oxidize the electrolyte unless a passivating SEI layer is formed, electronically insulating the electrode from the electrolyte and preventing further oxidation. The energy gap between the LUMO and HOMO hence defines the electrochemical stability window of the electrolyte. This should ideally be larger than the difference between the chemical potentials of the electrodes. If a stable electronically-insulating layer is formed the SEI can passivate the electrodes and suppress decomposition reactions enabling the cell to operate outside the electrolyte stability voltage window. The key is that the SEI layer growth should self-terminate in subsequent cycles since SEI formation is an irreversible process consuming part of the electrolyte and lithium ions in the battery [66]. Excessive growth of the SEI can worsen battery performance leading to increase of ionic resistance. If this is the case, diffusion of Li ions through the SEI becomes the limiting process in battery operation. As a consequence, proper combinations of electrodes and electrolytes are necessary for high performance batteries.

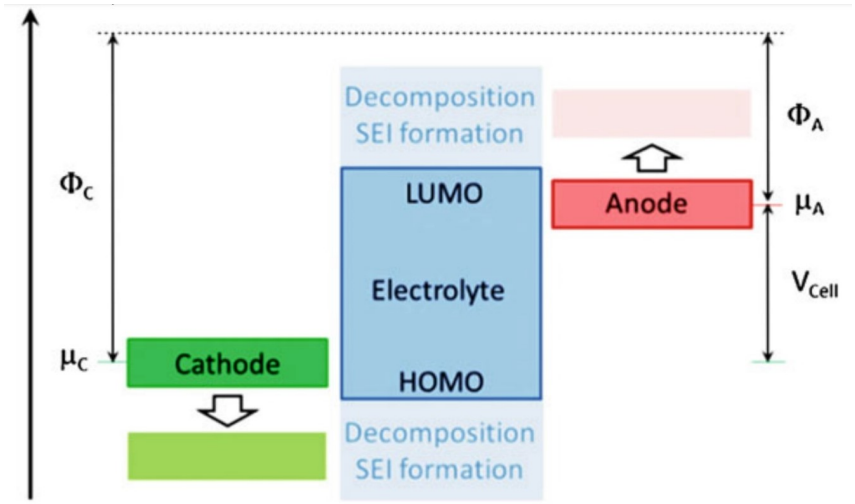

Figure 1.7: Schematic energy diagram of an electrolyte as well as the cathode and anode work functions, Φ_C and Φ_A, respectively (equal to the electrode electrochemical potentials, the difference of which is the open-cell voltage of the battery, V_{Cell}). The difference between the LUMO and the HOMO is the stability window of the electrolyte. If the electrode electrochemical potentials fall outside this stability window the electrolyte will decompose, which SEI layer formation can passivate, leading to the kinetic stability of the electrolyte and making the light areas (lower left and upper right) accessible [14].

When using liquid electrolytes, separators are needed to physically divide the electrodes preventing shorting. The separator is an inert, porous membrane that allows ions to freely pass through it and is designed to seal shut if the battery temperature becomes too high. The membrane must be thin enough to allow proper ion flow while being thick enough to maintain mechanical strength. The separators are soaked in an organic solvent containing dissolved lithium salts. Typical organic solvents used in Li ion batteries include ethylene carbonate (EC), propylene carbonate (PC) and dimethyl carbonate (DMC). Typical lithium salts are $LiPF_6$, $LiClO_4$, $LiCF_3SO_3$, and $LiBF_4$ with lithium hexafluoride ($LIPF_6$) being the most common due to its high ionic conductivity. A prototypical electrolyte mix is a 1 molar solution of $LiPF_6$ in a 1:1 EC/DMC, which offers an ionic conductivity of 10.9 mS/cm at 25°C [67].

1.2.5. Solid Electrolyte Interphase (SEI)

As previously mentioned SEI is formed during first charge-discharge cycles due to electrolyte decomposition on the surface of the strongly reducing anode. SEI must have good lithium-ion conductivity and be electrically insulating to prevent further reduction of the electrolyte by the surface of the lithiated silicon. This enables lithium-ion batteries to

reversibly charge and discharge for hundreds of cycles. The SEI on silicon anodes has been reported to consist of a combination of lithium silicate (Li_xSiO_y), lithium carbonate (Li_2CO_3), lithium fluoride (LiF), lithium alkyl carbonates and other decomposition products of the electrolyte [55], [45]. Although the composition of the SEI is generally known, the formation of the initial SEI formed on silicon anodes, and the changes it undergoes during cycling, still remains unclear. In particular, a general understanding of the correlation between chemical composition of SEI and battery performances are poorly understood. However, it has been reported that the stability of the SEI on silicon anode is very problematic, due to the previously mentioned large changes in surface area during cycling [24]. The detailed mechanism behind the evolution and thickening of the SEI is not fully understood. Since the knowledge of SEI instability on silicon anodes is well-established, one approach to address this issue is the use of electrolyte additives that promote SEI formation. While various electrolyte additives have been explored for silicon anodes, fluorinated additives have shown the most promise results [69], [74], especially fluoroethylene carbonate (FEC) [43], [35]. However, while many investigations have been conducted on the functional mechanism of FEC , the reason why FEC is able to produce a "better" SEI still remains an open problem. However, previous researchers have reported that incorporation of FEC causes the formation of compact surface films containing polymeric species and high concentrations of LiF [34], [32].

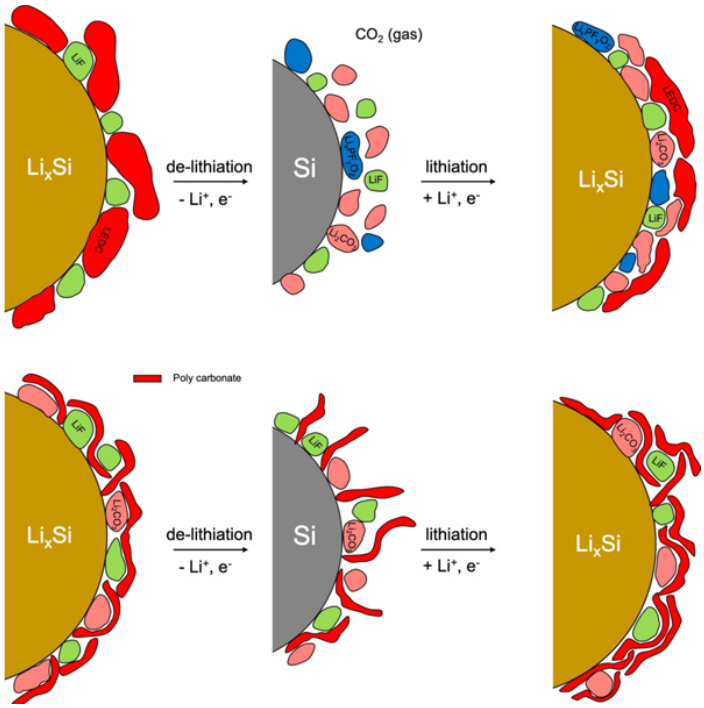

Figure 1.8: Schematic diagram for the initial generation and evolution of SEI layers on silicon electrodes derived by EC electrolytes (top) and FEC based electrolytes (bottom) [18].

In EC based electrolytes on silicon anodes, initial SEI is composed of the reduction products of the electrolyte such as $LEDC$ and LiF. As the SEI components fracture , because of volume expansions, the surface area of the SEI particles is increased. Unstable SEI component as $LEDC$ are exposed to the acidic species in the electrolyte making SEI decomposition more likely to occur. The initial SEI, composed of $LEDC$ and LiF, degrades to generate Li_2CO_3, lithium alkoxides, CO_2, and oligoethylene oxide according to the reaction shown in Figure 1.9.

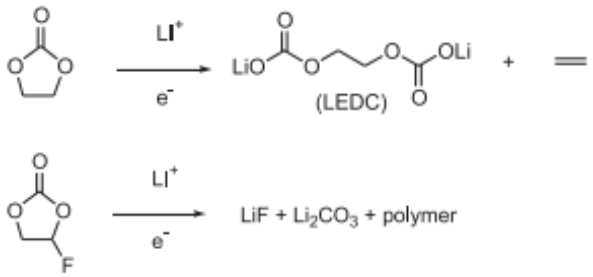

Figure 1.9: Primary initial electrolyte reduction products of EC and FEC [18].

A critical aspect of these decomposition reactions is that most of these products are ei-

ther soluble in the electrolyte or gaseous. This brings to an increase in the porosity of the SEI, allowing more electrolyte to interact with its surface and consequently promoting further electrolyte reduction. The overall effect is the thickening of the SEI [33], [3]. The continuous decomposition and reformation of the SEI on the surface of silicon particles creates an insulating layer, worsening electrode conductivity. As a result, lithium ions are trapped within the anode, contributing to significant capacity fading.
Incorporation of FEC in electrolytes results in a significant change in the composition and stability of the SEI. The initial SEI generated from FEC electrolytes is primarily composed of Li_2CO_3, polycarbonate, and LiF. An investigation utilizing HAXPES (Hard X-ray Photoelectron Spectroscopy) revealed that, upon cycling, an inner layer of lithium silicate and silica is still observed also in FEC based electrolytes, but the composition of the outer layer of the SEI does not change significantly as shown according the reaction in Figure 1.9 [17]. The outer SEI layer is still characterized by a mixture of LiF, Li_2CO_3, and polycarbonate. This suggests that the SEI components generated from the reduction of FEC are more stable and do not decompose. When the SEI is made of more stable compounds, such as Li_2CO_3, similar mechanical fracturing will occur, but the lower reactivity of Li_2CO_3 with the electrolyte slows the rate of SEI evolution. Moreover, the presence of polycarbonate enhances the elasticity of the SEI, thereby improving its mechanical strength. Additionally, there an increased concentration of LiF in the form of nanostructured particles is observed.

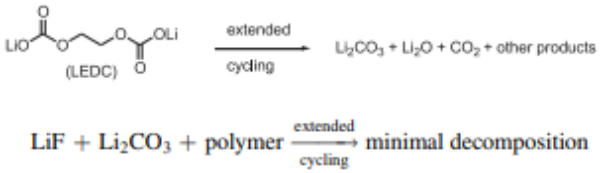

Figure 1.10: Primary initial SEI reduction products from EC and FEC electrolytes [18].

Another way to improve the performance of silicon anodes involves the investigation of surface modifications. Specifically, incorporating binders with alcohol or carboxylic acid functional groups, such as polyacrylic acid (PAA), into the electrolyte can result in significantly better performance compared to traditional binders like polyvinylidene fluoride (PVDF) [42], [46]. To understand why PAA binders significantly improve the capacity retention of silicon anodes, the interaction between the binders and the silicon particle surface has been studied. Such investigation shows that the surface of silicon reacts with PAA through the carboxylic acid groups before cycling [26]. In view of this result, citric acid (CA) was used as a surface-modifying agent for silicon particles to enhance this reaction [27], [44]. Specifically, the carboxylic acid and alcohol functional

groups in citric acid (CA) react with the surface of silicon nanoparticles before cycling, forming silyl esters (–Si–O–C(O)–C–) on the surface. This interaction was confirmed through a combination of IR-ATR and TGA analyses. Furthermore, during the first lithiation, the surface layer of citric acid (CA) is reduced to lithium citrate, forming a stable SEI layer. This minimizes formation of electrolyte decomposition products, such as LEDC and Li_2CO_3, both after the initial formation cycling and during extended cycling. Surprisingly, the cycling performance of silicon anodes with CA shows improvements similar to those observed with PAA binders.

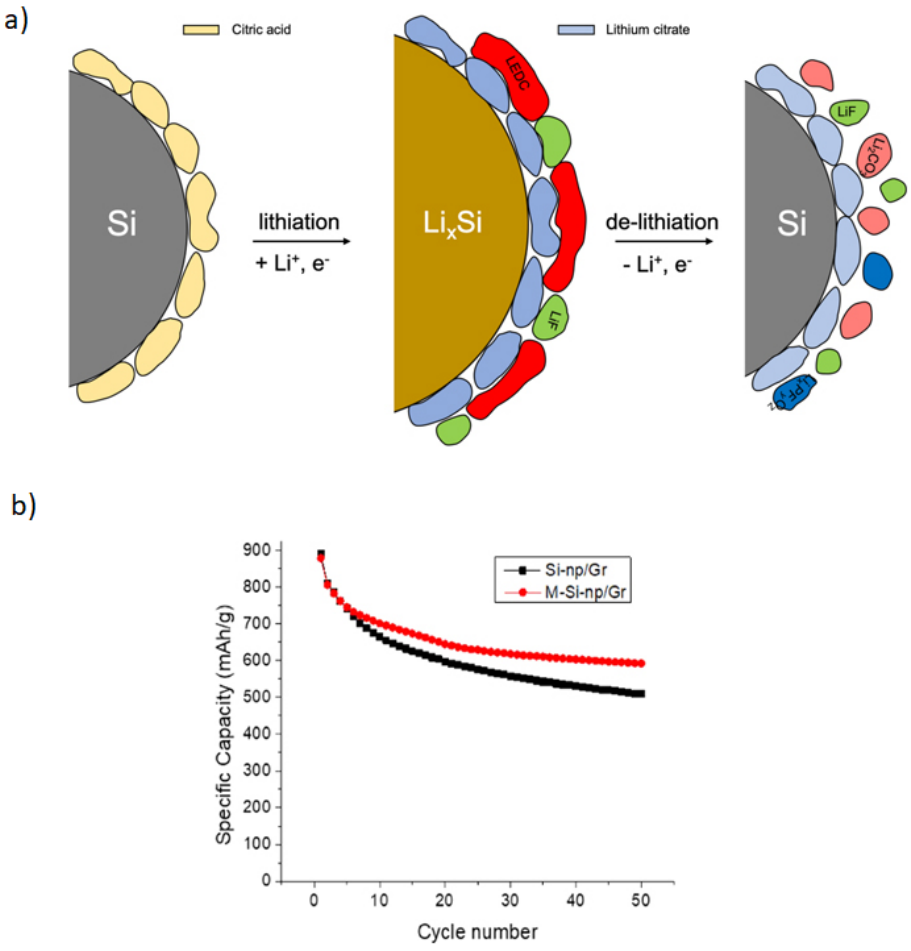

Figure 1.11: a) Schematic diagram for the initial generation and evolution of the SEI layers on silicon electrodes with citric acid as a surface modifying agent. The citric acid modification results in the generation of a pre-SEI which stabilizes the surface of silicon electrodes. b)Specific capacity retention of silicon graphite composite electrodes with silicon nanoparticles (Si-np/Gr) and silicon nanoparticles surface modified with citric acid (M-Si-np/Gr) [18].

1.3. Role of NMR in detecting SEI species

As glimpsed from the previous discussion, the dynamics of stable SEI formation and subsequent correlation with performance in a lithium-ion battery remains unclear to this day. An important step in understanding this problem could be made if we were able to develop an experimental methodology that enables simultaneous tracking of the chemical composition of the SEI and the electrochemical cycling data on a working battery. Such kind of experiments are called *in operando* measurements. In operando experiments are conducted while a system is actively operating, allowing real-time monitoring of changes as they occur under normal device operation. In contrast, *in situ* experiments also observe systems during operation; however, the operating conditions are temporarily interrupted during measurements, and the experiments are conducted without disassembling the sample. Fnally *ex situ experiments* are performed once the system has been removed from its operational state, providing insights about changes post-operation, but lacking the real-time, dynamic perspective offered by in operando and in situ methods.
Operando solid-state NMR spectroscopy can be a solution for real-time monitoring of SEI species. In particular, Nuclear magnetic resonance (NMR) spectroscopy is well-suited for operando measurements on electrochemical cells due its noninvasive, nondestructive features. Moreover, NMR experiments on ^7Li (spin-3/2), because of its high natural abundance (92.4%) are characterized by high sensitivity levels. In addition to this, compared to other experimental operando setups, operando NMR cells are closer, from a physical point of view, to daily lives batteries. Despite this, at the current state of art, operando NMR experiments have been performed only using single-channel probes in which one nucleus is directly excited, precisely ^7Li. As a consequence, measured spectra on a working battery are characterized by resonance peaks associated to ^7Li in the cathode, anode, electrolyte and, due to its expected negligible quantity with respect to the previously mentioned components, a peak associated to the SEI. In particular, both electrolyte and SEI have chemical shift at about 0 ppm, but due to the liquid state and much higher quantity of electrolyte compared to the SEI, signal from the latter will be obscured by the sharp liquid-state peak coming from the electrolyte.

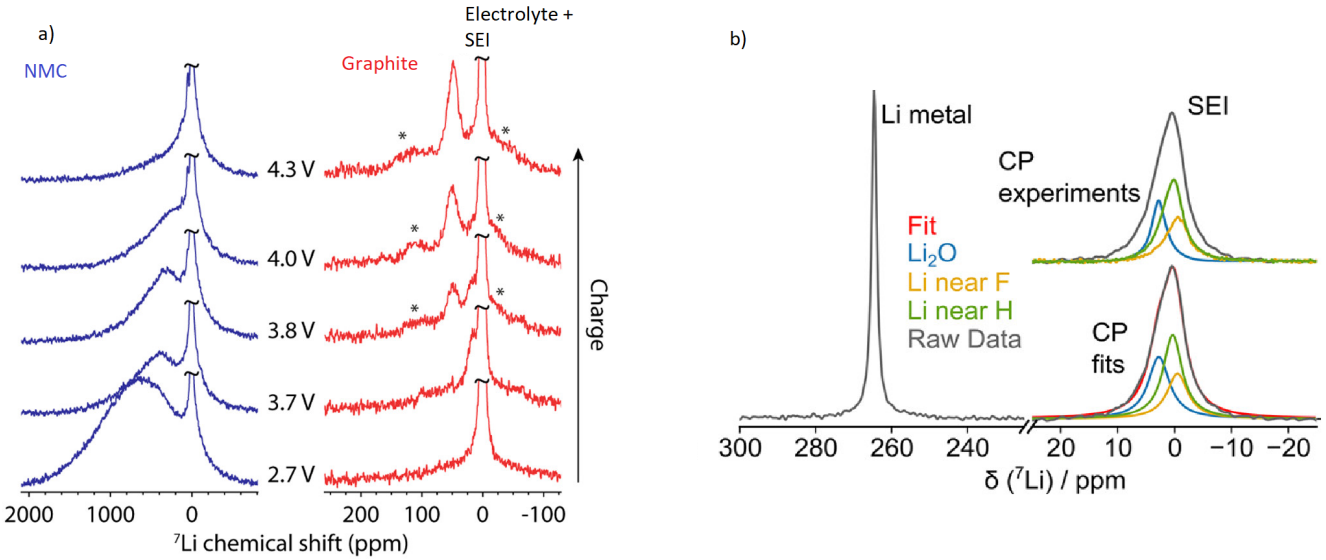

Figure 1.12: a) Representative NMC (blue) and graphite (red) spectra evolution of NMR spectra under operando conditions [68] b)^7Li SSNMR spectrum (gray) along with SEI peak deconvolutions corresponding to Li_2O (blue), Li near F (yellow), Li near H (green), and the peak deconvolution sum (red) for a representative sample of Li metal cycled in 0.5 M $LiTFSI$ + 0.5 M $LiNO_3$ electrolyte. The inset above the SEI peak shows the weighted CP experiments along with the Li_2O single-pulse experiment (measured for bulk Li_2O) used to deconvolute the full SEI peak in gray [36].

Moreover, due to SEI heterogeneity and impossibility to use magic angle spinning in operando NMR experiments, SEI signal under operando conditions is expected to be broad and almost comparable to background noise. It is therefore necessary to implement a technique aimed at suppressing anode, cathode and electrolyte signals and selectively detect SEI. As previously discussed SEI is composed by both organic and inorganic Li salts, whose main representative compound for the seconds is LiF. By implementing $^1H -^7 Li$ polarization transfer in operando measurements, it is possible to detect NMR signal coming from ^7Li in close proximity to ^1H nuclei in an rigid environment only. This condition is surely fulfilled by organic SEI components. In this way organic SEI components are selectively detected. Moreover, the well-separated LiF peak from other fluorinated compounds in the ^{19}F spectrum allows for a powerful approach to monitoring inorganic SEI formation dynamics under operando conditions. By combining the tracking of organic SEI components through $^1H -^7 Li$ polarization transfer with the detection of inorganic SEI compounds via ^{19}F direct excitation, this method provides a comprehensive tool for studying SEI evolution in real time. As future developments of this projects operando NMR experiments will be performed for the first time using a dedicated double-channel

resonance probe. Beside the important breakthrough that such technique could bring to, several considerations have to be made. When working in operando conditions, magic angle spinning cannot be used. As a consequence small SEI quantity and broad peaks of static experiments will represent a challenge for the scopes of operando NMR. Moreover, due to simultaneous presence of RF fields and electrochemical cycling circuit inside the NMR probe, magnetic field inhomogeneities can arise, making polarization-transfer not easy to calibrate. Finally, lithiation and delithiation change magnetic permeability of the anode (and consequently the one of the coil), causing off-resonances of the radio frequency pulses sent to the sample. Because of this, automatic tuning-matching (ATM) facility will be installed on the probe.

Before jumping into the darkness of operando experiments, a preliminary $^{1}H -^{7} Li$ CP calibration will have to be performed on reference sample to verify reliability of cross-polarization between these nuclei on a standard double channel NMR probe. CP quality and feasibility will then be tested on cycled Si anodes. This latter will be the heart of the discussion presented in this work. In addition, due to the small quantity expected from the SEI, further signal enhancement technique will be investigated. It is worth mentioning that to compensate small SEI quantity, Si anodes, subjected continuous SEI thickening, are chosen in order to maximize the amount of SEI formed. This is needed to guarantee reasonable sensitivity in NMR spectra

If these experiments on ex-situ samples verify organic SEI selectivity in static conditions, operando experiments on a dedicated double channel probe can then be ran and optimized.

2 | NMR theory

NMR spectroscopy can probe local chemical structures in molecules and materials based on the interaction of the magnetic moment of a nucleus with a magnetic field. The nucleus can be imagined as a charged particle spinning around its axis. While spinning the charged particle creates an electric current, producing a small magnet. The charged particle is not actually rotating from spinning, but the spin itself is rather an intrinsic physical property first derived by Dirac in his study of quantum mechanics and relativity.

2.1. Larmor precession

All nuclei that have a non-zero angular momentum, I, also are characterized by magnetic dipole moment, μ expressed by:

$$\mu = \gamma_I I$$

where γ_I is the gyromagnetic ratio of the nuclei's magnetic moment to its angular momentum. The overall magnetization in a material, arising from the nuclei in the sample, is $\mathbf{M}$ and is given by vectorial sum of all the individual magnetic moments associated with all the nuclei:

$$\mathbf{M} = \sum_i \mu_i$$

Thus we can write the net magnetization of the sample as:

$$\mathbf{M} = \gamma_I \mathbf{J}$$

where $\mathbf{J}$ is the net nuclear spin angular momentum of the sample giving rise to the *bulk magnetization*. From a classical point of view, when a nucleus (with $I > 0$) is placed in a magnetic field $\mathbf{B_0}$, its magnetic dipole moment interacts the magnetic field, making the nuclei precess about the direction of the field due to the presence of a mechanical torque

$\mathbf{T}$ equal to:

$$\mathbf{T} = \mathbf{M} \times \mathbf{B_0}$$

According to the second cardinal equation of motion, $\mathbf{J}$ evolves as:

$$\frac{d\mathbf{J}}{dt} = \mathbf{T} = \mathbf{M} \times \mathbf{B_0}$$

which is equivalent to:

$$\frac{d\mathbf{M}}{dt} = \gamma_I \mathbf{T} = \gamma_I \mathbf{M} \times \mathbf{B_0}$$

It can be shown that this last equation predicts that $\mathbf{M}$ precesses about the magnetic field $\mathbf{B_0}$ at a constant angular speed $\omega = \gamma_I B_0$.
In NMR the applied field is assumed to be along the z axis of the laboratory reference frame, i.e. $\mathbf{B_0} = (0, 0, B_0)$ in the above equations. The frequency with which the magnetization precesses about this field is defined as ω_0, the *Larmor frequency*:

$$\omega_0 = -\gamma_I B_0$$

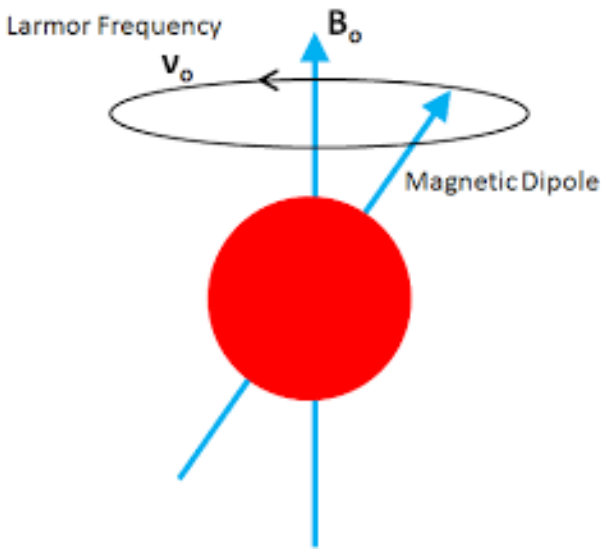

Figure 2.1: Schematic representation of Larmor precession around external static magnetic field B_0.

2.2. Equilibrium magnetization

In presence of an external magnetic field $\mathbf{B_0}$ dipoles acquire an energy which is dependent on their relative orientation with respect to the field given by:

$$E = -\boldsymbol{\mu} \cdot \mathbf{B_0}$$

Using a quantum mechanical description of the angular momentum of the nucleus, its modulus can be rewritten as $J = \hbar\sqrt{I(I+1)}$ where I is the nuclear spin quantum number. Since the magnetic field $\mathbf{B_0}$ is taken to be along the z axis of the laboratory frame, it introduces a quantization axis in such a way that the nuclear angular momentum can be projected along this direction. The z-projection of the nuclear momentum is then equal to $J_z = \hbar m_I$ where m_I can assume all values between $-I$ and $+I$ equally spaced by 1. In this context, the interaction with the field results in a quantization of the energy of each dipole described by the so-called *Zeeman effect* for which:

$$E = -\hbar\gamma_I m_I B_0$$

In particular, considering the case of spin-1/2 nuclei, the difference in energy between the two discrete levels resulting from Zeeman interaction is proportional to Larmor frequency:

$$\Delta E = E_{-1/2} - E_{+1/2} = \frac{1}{2}\hbar\gamma_I B_0 + \frac{1}{2}\hbar\gamma_I B_0 = \hbar\gamma_I B_0$$
$$\Delta E = -\hbar\omega_0$$

Considering an ensamble of spin-1/2 nuclei at temperature T in presence of an external field $\mathbf{B_0}$, the magnetic interaction will try to align the dipoles along the direction of the field (thus making the lower energy state more populated) while thermal fluctuations will try to randomize this process. As a overall the relative population of the two energetic levels resulting from Zeeman interaction is driven by a Boltzmann statistics such that:

$$\frac{n_{-\frac{1}{2}}}{n_{+\frac{1}{2}}} = e^{-\frac{\Delta E}{K_b T}}$$

where $n_{-\frac{1}{2}}$ and $n_{+\frac{1}{2}}$ represent the density of nuclei in the $-1/2$ and $+1/2$ spin state respectively. The dipoles direction in the xy plane are instead randomly distributed.
We can conclude that the more the energetic levels are far in energy, the bigger the

unbalance in relative population will be, thus creating an excess in the population of one of the two energy levels. This brings to the formation of an intrinsic magnetization, always present in thermal equilibrium conditions, also called *equilibrium magnetization* M_z (also called *longitudinal magnetization*) that represents the starting point of all NMR experiments.

2.3. RF pulse effect

According to a classical vector model of the equilibrium magnetization, by applying a radio-frequency field $\mathbf{B_1}(t)$, with pulsation ω_{rf}, along a direction orthogonal to the static $\mathbf{B_0}$ field it is possible to perturb the equilibrium magnetization making it precess about the RF field direction. The effect of this field is more easily seen by transforming the whole problem into a rotating frame of reference which rotates at the same frequency of the RF field ω_{rf} around $\mathbf{B_0}$. If $\omega_{rf} = \omega_0$, then the magnetization vector $\mathbf{M}$ appears stationary in the rotating frame, thus removing the effects of the static $\mathbf{B_0}$ field. The result of this interaction is that the magnetization vector $\mathbf{M}$ precesses about $\mathbf{B_1}$ at a frequency $-\gamma_I B_1$ defined as the *nutation frequency*. In the following discussion of experimental results, this frequency will be defined by the power sent to the probe through the ^1H (or ^7Li) channel.

The RF field is able to rotate the longitudinal magnetization by an angle θ_{rf} called *nutation angle* (or *flip angle*) which is equal to $\theta_{rf} = \omega_{rf}\tau_{rf} = -\gamma_I B_1 \tau_{rf}$, where τ_{rf} represents the time duration of the RF pulse. In most of NMR experiments, one of the first steps is to convert the longitudinal magnetization into *transverse magnetization*. This is done by the application of a so called $90°$*pulse* where the RF field is able to nutate the equilibrium magnetization from the z to the x (or y) axis.

The system is now out of its equilibrium conditions and in order to reach this situation again it starts precessing, with Larmor frequency, about the static $\mathbf{B_0}$ field causing a gradual re-appearing of the equilibrium magnetization and decaying of the transverse one as reported in Figure 2.2. These processes are called *longitudinal* and *transverse relaxation* and are characterized by the time constants T_1 and T_2 respectively known as $spin - lattice$ and *transverse relaxation* times. M_z and M_y (or M_x) vary over time according to exponential laws of the form:

$$M_z = M_0(1 - e^{-\frac{-t}{T_1}})$$

$$M_y = M_0 e^{-\frac{-t}{T_2}}$$

From the experimental point of view, what is actually measured in an NMR experiment is the signal coming from the transverse magnetization. During relaxation, transverse magnetization precession about the static magnetic field induces a varying magnetic field inside the RF coil (that behaves as both transmitter and receiver) that translates in an electronic signal and represents the so-called *free induction decay* (FID) of the spin-system. Finally, by Fourier transforming the acquired signal it is possible to retrieve the actual spectrum of the sample.

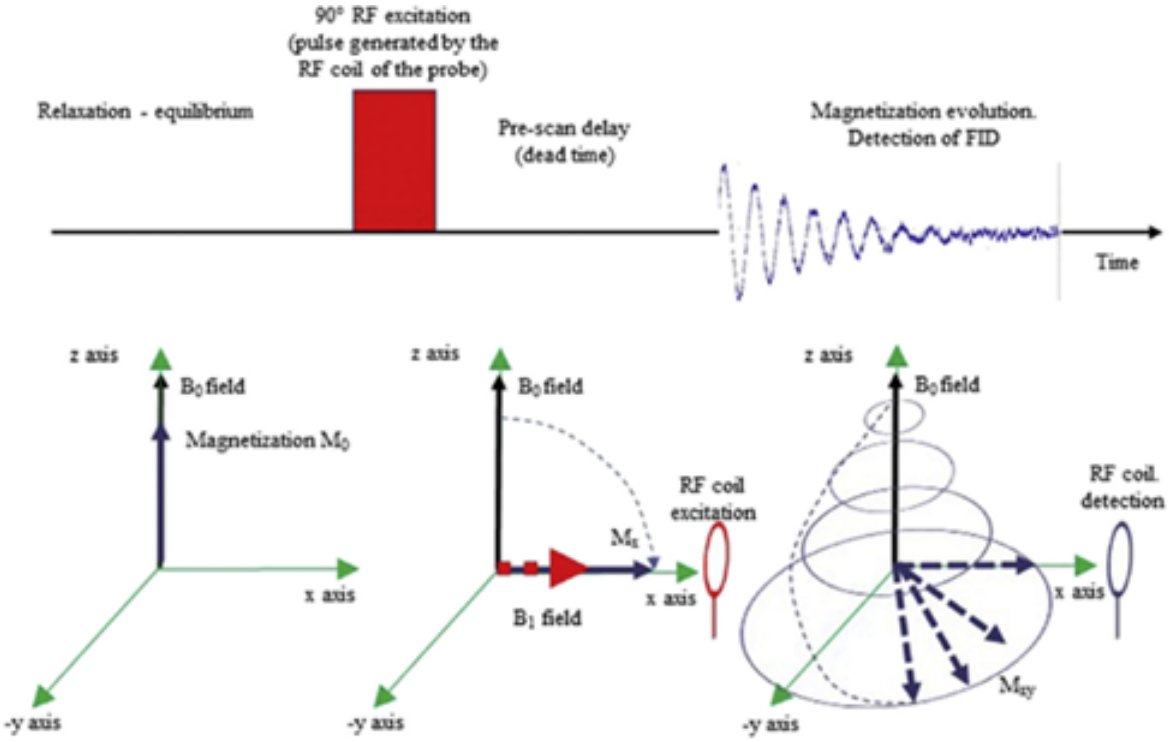

Figure 2.2: Schematic representation of NMR effect of RF pulse, relaxation and FID signal acquisition [29].

2.4. Relaxation

Relaxation is a complex topic for NMR describing energy exchange between nuclei and external environments. In particular, such energy transfer is triggered by local fluctuations of magnetic field in along parallel directions of the external static magnetic field $\mathbf{B_0}$ that oscillate with frequency close to the Larmor frequency. One of the causes of fluctuations is related to random rotational and translational motion of molecules. Usually for bigger and

mechanically inert molecules, motions occurs on a slower time scale compared to smaller ones. The latter, in particular, are more likely to feel fast varying magnetic fields, making relaxation happen on a shorter time scale. As additional consideration, also chemically heterogeneous environments are expected to produce local field fluctuations due to the bigger variety of interactions involved, thus relaxation will easily manifest. In solid state NMR, relaxation mechanisms are significantly different from those in liquid-state NMR due to the restricted molecular motion and strong dipolar interactions. Various interactions govern relaxation in solid-state NMR, including dipole-dipole interactions, chemical shift anisotropy (CSA), quadrupolar coupling, and spin diffusion. The primary relaxation processes in solid-state NMR are longitudinal relaxation (T_1), transverse relaxation (T_2), and rotating frame relaxation ($T_{1\rho}$). Longitudinal relaxation (T_1) describes the recovery of magnetization along the external magnetic field (B_0) due to energy exchange with the surrounding lattice. Transverse relaxation (T_2) represents the loss of phase coherence among spins, influenced by dipolar couplings and local field inhomogeneities. Rotating frame relaxation ($T_{1\rho}$) occurs under a spin-locking field and provides insights into slow molecular motions and interactions.
From practical point of view, longitudinal relaxation time T_1 represents a crucial parameter for NMR spectroscopy experiments since defines the recycle delay, which represents the time that has to be waited between the acquisition of one scan and the following. Depending on T_1 overall experimental time will be different. In particular, for spectra in which signal to noise ratio per square root of time (such quantity represents sensitivity of NMR signal) has to be maximized, recycle delay has to be set to $1.3{*}T_1$ in order to wait shortest possible time for the system to sufficiently relax and restore a reasonable amount of equilibrium magnetization. In case instead of quantitative spectra, full relaxation is needed and because of this recycle delay has to be set to $5{*}T_1$.

2.5. Nuclear spin interactions

In the NMR experiment, the applied static field $\mathbf{B_0}$ is much larger than any local field arising within the sample generated by other nuclear magnetic dipoles and chemical shielding. As a result $\mathbf{B_0}$ remains as the quantization axis for the nuclear spins in the sample and many of these local fields have negligible effects on the spin states. From a quantum mechanical point of view, the hamiltonian describing the interaction between any local field $\mathbf{B_{loc}}$ and a nuclear spin is given by:

$$\hat{\mathbf{H}} = -\gamma_I \hat{\mathbf{I}} \cdot \hat{\mathbf{B}}_{loc}$$

where we can express the local magnetic field in the interaction as $\mathbf{B_{loc}} = \mathbf{A_{loc}} \cdot \mathbf{J}$, where $\mathbf{A_{loc}}$ is a second-rank cartesian tensor (also called *coupling tensor*) describing the nuclear spin interaction and its orientation dependence. The vector $\mathbf{J}$ is the general source of $\mathbf{B_{loc}}$ at the nucleus (i.e. another nuclear spin in the case of dipole-dipole coupling, or $\mathbf{B_0}$ itself in case of chemical shielding), hence the general form of the interaction hamiltonian is given by:

$$\hat{\mathbf{H}} = \hat{\mathbf{I}} \cdot \ \hat{\mathbf{A}}_{loc} \cdot \hat{\mathbf{J}}$$

In solid state NMR spectroscopy, the three main interactions arise from *chemical shielding*, the source of chemical shift, *dipole-dipole coupling* and *quadrupolar coupling*.

Chemical Shielding

The interaction hamiltonian of chemical shielding is:

$$\hat{H}_{cs} = -\gamma_I \hat{\mathbf{I}} \cdot \hat{\boldsymbol{\sigma}} \cdot \hat{\mathbf{B_0}}$$

where $\hat{\boldsymbol{\sigma}}$ is the so called *anisotropic chemical shielding tensor* describing the perturbation caused by electrons subjected to $\mathbf{B_0}$ field around a nuclear spin $\mathbf{I}$. Orientation dependence arises because electrons react in different ways according to the orientation of the external static field, producing a secondary magnetic field on the nucleus. This secondary field contributes to the total field felt by the latter, and therefore can change the resonance frequency of the nucleus.

Dipole-dipole Coupling

In case of dipolar coupling, the hamiltonian acting on the system has form:

$$\hat{H}_{dd} = -2\hat{\mathbf{I}} \cdot \hat{\mathbf{D}} \cdot \hat{\mathbf{S}}$$

where now the dipolar-coupled spin $\mathbf{S}$ is the source of local magnetic field acting on spin $\mathbf{I}$, $\mathbf{D}$ represents the *dipolar coupling tensor* which describes the strength and orientation dependence of the interaction between $\mathbf{I}$ and $\mathbf{S}$. The interaction between the two spins arises because of the magnetic field each creates around itself. The orientation dependence arises due to the fact that the applied magnetic field $\mathbf{B_0}$, orientates both spins $\mathbf{I}$ and $\mathbf{S}$ and consequently the field that each creates. Hence the interaction between them then depends on the relative position of the two spins in space with respect to $\mathbf{B_0}$ in a similar manner to the chemical shielding described before.

Quadrupolar Coupling

Quadrupolar coupling is an internal interaction, that is present only in nuclei showing nuclear momentum $I \geq 1$, between the nuclear electric quadrupole momentum and an electric field gradient. Nevertheless, the hamiltonian describing the quadrupole interaction can be expressed in a similar manner to the previous ones:

$$\hat{H}_Q = -2\frac{eQ}{2I(2I-1)\hbar}\hat{\mathbf{I}} \cdot \hat{\mathbf{V}} \cdot \hat{\mathbf{I}}$$

where $\hat{\mathbf{V}}$ is the electric field gradient tensor and Q is the nuclear electric quadrupole momentum.
It is worth noticing that such interaction is expected to be stronger in systems characterized by an higher degree of asymmetry of the electronic environment.

2.5.1. Principal axis frame

As previously discussed, nuclear spin interactions depend on molecular orientation hence their size must be described by a second-rank tensor. For example, considering anisotropic chemical shielding in cartesian coordinates, the associated second-rank tensor is given by:

$$\hat{\boldsymbol{\sigma}} = \begin{bmatrix} \sigma_{xx} & \sigma_{xy} & \sigma_{xz} \\ \sigma_{yx} & \sigma_{yy} & \sigma_{yz} \\ \sigma_{zx} & \sigma_{zy} & \sigma_{zz} \end{bmatrix}$$

The meaning of the shielding tensor becomes clearer when expressing the shielding tensor in the laboratory frame (defined by $\mathbf{B_0}$ along z). The local magnetic field at a nucleus with a shielding tensor σ^{lab} , i.e. expressed within the laboratory frame, is:

$$\begin{aligned} \mathbf{B_{loc}} &= \boldsymbol{\sigma}^{lab} \cdot \mathbf{B_0} \\ &= \begin{bmatrix} \sigma_{xx} & \sigma_{xy} & \sigma_{xz} \\ \sigma_{yx} & \sigma_{yy} & \sigma_{yz} \\ \sigma_{zx} & \sigma_{zy} & \sigma_{zz} \end{bmatrix} \cdot \begin{bmatrix} 0 \\ 0 \\ B_0 \end{bmatrix} \\ &= \begin{bmatrix} \sigma_{xz}B_0 \\ \sigma_{yz}B_0 \\ \sigma_{zz}B_0 \end{bmatrix} \end{aligned}$$

For instance $\sigma_{xz}B_0$ is the local shielding field in the laboratory x-direction, when $\mathbf{B_0}$ is applied along z.
Dipolar and quadrupolar coupling tensors can be understood in a similar way: $D_{xz}^{lab}\hat{S}_z$ is the local magnetic field at spin $\mathbf{I}$ in the laboratory x-direction arising from the z-component of the $\mathbf{S}$ spin.
The usefulness of this representations relies on the fact that it is possible to choose a particular axis frame, on which interaction tensor defined, such that the interaction tensor is represented by a diagonal matrix. This axis frame is the so called *principal axis frame* and the numbers along the resulting diagonal of $\boldsymbol{\sigma}^{PAF}$ are the *principal values*: σ_{xx}^{PAF} is the principal axis frame x-axis. The principal axis frame of the shielding tensor is determined by the electronic structure of the molecule containing the considered nucleus and remains fixed with respect to the molecule. We can thus picture an interaction tensor as being represented by an ellipsoid fixed within the molecule and centered on the nucleus it applies to. The principal axis of the ellipse coincide with the principal axis frame of the tensor and the length of each principal axis of the ellipsoid is proportional to the magnitude of the principal value of the interaction tensor associated to that principal axis.

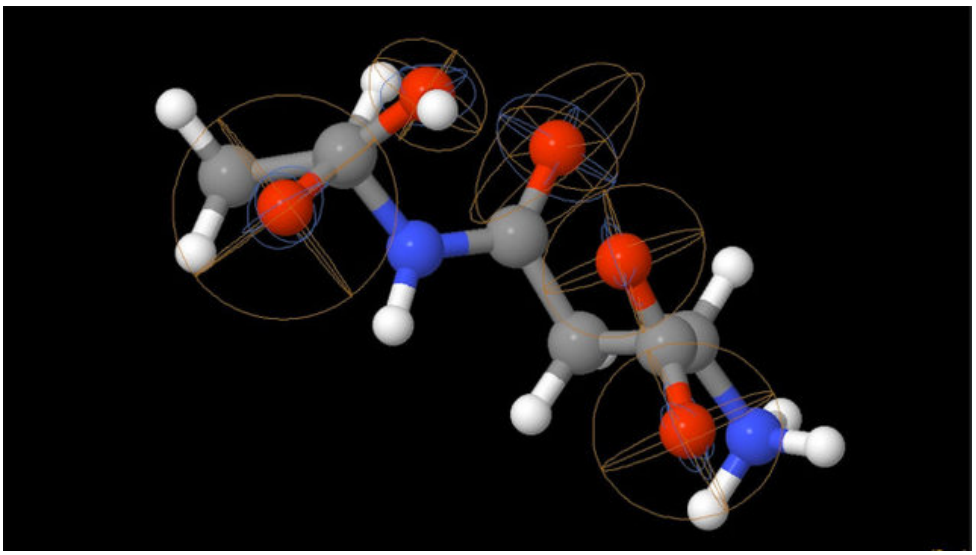

Figure 2.3: Schematic representation of electric field gradient (blue) and shielding (orange) tensors in -aspartyl-alanine of ^{17}O [57].

If the molecular orientation in the laboratory frame changes, so does the orientation of the interaction tensor. If the nucleus is at a crystallographic site of symmetry, then the interaction tensor reflects this symmetry. For instance, the shielding tensor for a nucleus at a site of axial symmetry has a principal axis frame in which the z^{PAF}-axis coincides

with the symmetry axis and the principal values are such that $\sigma_{xx}^{PAF} = \sigma_{yy}^{PAF} \neq \sigma_{yy}^{PAF}$. The three principal values of an interaction tensor $A_{\alpha\alpha}^{PAF}$ are expressed as *isotropic value* A_{iso}, *anisotropy* Δ_A and *asymmetry* η_A of the interaction and all are expressed as:

$$A_{iso} = \frac{1}{3}(A_{xx}^{PAF} + A_{yy}^{PAF} + A_{zz}^{PAF})$$

$$\Delta_A = A_{zz}^{PAF} - A_{iso}$$

$$\eta_A = \frac{A_{xx}^{PAF} - A_{yy}^{PAF}}{\Delta_A}$$

Effectively, anisotropy is related to the elongation of the ellipsoid describing the interaction tensor and the asymmetry is a measure of how far a cross-section through the ellipsoid (parallel to the x^{PAF}-y^{PAF} plane) deviates from circular [5], [39].

3 | Solid state NMR

High-resolution solution-state NMR spectra are a result of the fast isotropic molecular tumbling. In the solid state, this motion is almost absent and anisotropic interaction lead inevitably to a broadening of the resonances. These anisotropic interactions, on the one hand, have the significant disadvantage of hindering the resolution of distinct sites, but on the other hand, contain valuable structural and dynamical information (specifically CSA and quadrupolar interactions provide insight into electronic structure and bonding, while dipolar coupling offers direct access to internuclear distances).
In an NMR experiment, the sensitivity, i.e. the signal to noise ratio (S/N) per square root of time, depends on the natural abundance, i.e. the number of NMR-active nuclei in the sample, as well as the gyromagnetic ratio γ_I . Between all nuclei, protons, ^1H have the best sensitivity. However, unlike in solution-state NMR where ^1H NMR is of central importance, in solid-state NMR there exists a major complication with this nucleus: the abundance of protons in organic solids means that strongly dipolar-coupled proton network will always be present,bringing to line broadening of the order of 50 kHz.

3.1. The orientation dependence of the NMR resonance frequency

In solid-state NMR the resonance frequency of a given nucleus within a particular crystallite depends on the orientation of the crystallite itself. As already discussed, orientation dependence of CSA, dipolar and (first-order) quadrupolar coupling can all be represented by a second-rank tensor. This means that the interaction can be mathematically described by a 3x3 matrix. For such a second rank tensor, there exists a principal axes system (PAS) that transforms the interaction tensor into a diagonal matrix.
Specifically the mathematical expression for the dependence of the resonance frequency that takes into account crystallite orientation is given by:

$$\omega = \omega_0(\sigma_{xx}^{PAS} cos^2(\phi) sin^2(\theta) + \sigma_{yy}^{PAS} sin^2(\phi) sin^2(\theta) + \sigma_{zz}^{PAS} cos^2(\theta))$$

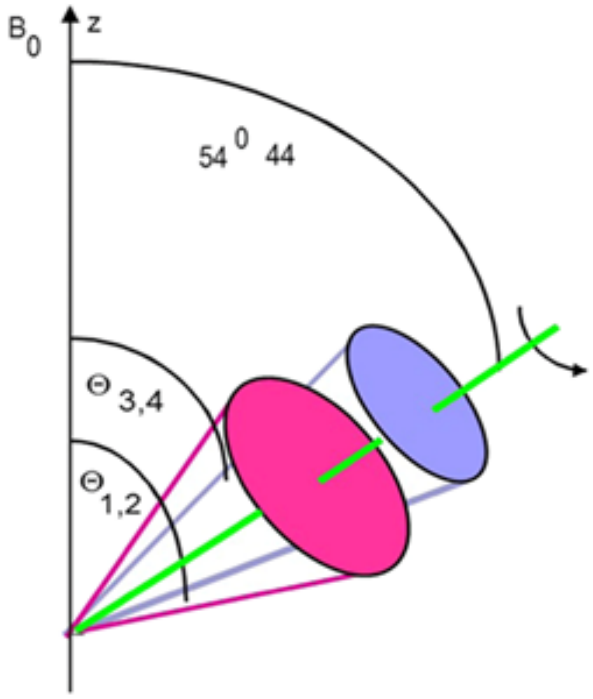

Figure 3.1: Schematics of directional averaging effect of MAS.

where θ and ϕ are the polar Euler angles defining the transformation of the PAS onto the laboratory frame defined by B_0.
In solid-state NMR, it is usual to deal with powdered samples characterized by a uniform distribution of molecular orientation in space. The NMR spectrum for a powdered sample, therefore consist of a superposition of many lines, corresponding to all the possible resonance frequencies, where each line originates from a given nucleus in a particular crystallite. This makes powder spectrum extremely broad because the chemical shift of each crystallite is different and consequently resolution can result problematic in solids.
In solution samples, isotropic tumbling of molecules averages to zero all anisotropic interactions. To achieve such high resolution also in the case of powdered samples, solid-state NMR spectroscopist would like to mimic this averaging process. It can be shown that a physical rotation of the whole sample around an axis inclined at an angle of $arctan(\sqrt{2}) = 54.7°$ to B_0 suffices to average any second-rank interaction to zero. This is actually achieved with so called magic-angle-spinning (MAS). To understand why magic-angle-spinning is so successful mean of line narrowing, it is first necessary to recognize that chemical shift anisotropy, dipolar and first-order quadrupolar interaction all have the same orientational dependence.

For an axially symmetric tensor (as in the case of dipolar interaction, CSA or first-order quadrupolar interaction with a zero asymmetry parameter) the orientation dependent

part of the frequency of a particular crystallite can be expressed in the form:

$$\omega = \frac{1}{2}(3cos^2(\theta) - 1)$$

where θ denotes the angle between the tensor PAS direction and B_0.
To illustrate the effect of MAS consider the "two-cones" model in Figure 3.2 showing the specific case of dipolar coupling between two spins. The two cones represent the range of positions adopted over the course of one rotor period for two different orientations of the internuclear vector relative to the rotor axis. In each case, the sample rotation leads to those components perpendicular to the rotor axis being zero on average and only component parallel to the rotation axis remains non-zero on average. Thus for any original orientation, rotation around an axis yields an "average orientation" parallel to the axis of rotation. If the rotation angle is inclined at the magic angle to B_0 this parallel component has an anisotropic frequency shift equal to zero for all cases. Thus under MAS the anisotropic broadening is averaged to zero by the sample rotation for all crystallite orientation.

3.2. Mathematical treatment of Magic Angle Spinning

Mathematical description of magic angle spinning can be given considering chemical shielding in the rotor frame described by the tensor σ_R for a given crystallite orientation with respect to the rotor axis frame as reported in Figure 3.2. The contribution of chemical shielding to the observed frequency frequency from a molecular orientation defined by Euler angles $\Omega = (\alpha, \beta, \gamma)$ at time t is:

$$\omega(\Omega; t) = -\omega_0 \mathbf{b_0^R} \sigma_R \mathbf{b_0^R}$$

where $\mathbf{b_0^R} = (sin(\theta_R)cos(\omega_R t), sin(\theta_R)sin(\omega_R t), cos(\theta_R))$, with θ_R representing the angle between the z-axis of the rotor frame and the static magnetic field $\mathbf{B_0}$ and ω_R is the spinning rate of MAS. By rewriting the shielding tensor in terms principal axis representation

$$\sigma_R = \mathbf{R^{-1}}(\alpha, \beta, \gamma) \begin{bmatrix} \sigma_{xx}^{PAF} & 0 & 0 \\ 0 & \sigma_{yy}^{PAF} & 0 \\ 0 & 0 & \sigma_{zz}^{PAF} \end{bmatrix} \mathbf{R}(\alpha, \beta, \gamma)$$

where $\mathbf{R}(\alpha, \beta, \gamma)$ is the rotation matrix that transforms from principal axis frame to rotor frame. Using the previously given definition of $\omega(\Omega; t)$ and the fact that $\theta_R = 54,7°$ we

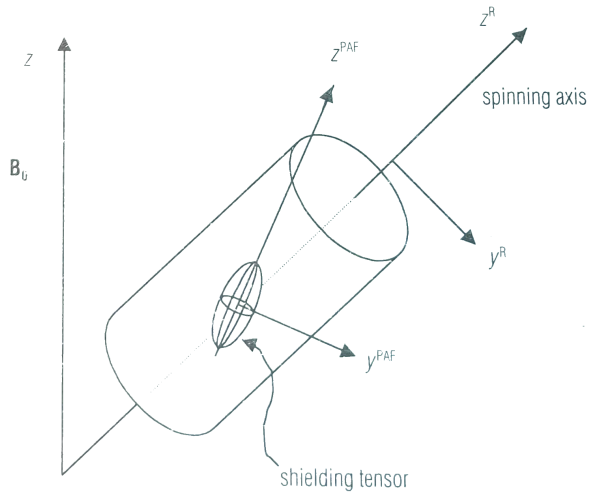

Figure 3.2: Illustration of axis frame used in the discussion of MAS. Shown here is the so called laboratory frame whose z-axis defines the direction of B_0, the rotor frame (superscript ^{R}) whose z^R axis is parallel to the spinning axis and the principal axis frame , the frame in which the shielding tensor is diagonal (superscript ^{PAF}).

obtain:

$$\omega(\Omega;t) = -\omega_0\{\sigma_{iso}+[A_1cos(\omega_R t+\gamma)+B_1sin(\omega_R t+\gamma)][A_2cos(2\omega_R t+\gamma)+B_2sin(2\omega_R t+\gamma)]\}$$

where

$$A_1 = \frac{2}{3}\sqrt{2}sin(\beta)cos(\beta)\{(\sigma_{xx}^{PAF} - \sigma_{zz}^{PAF})cos^2(\alpha) + (\sigma_{yy}^{PAF} - \sigma_{zz}^{PAF})sin^2(\alpha)\}$$

$$B_1 = \frac{2}{3}\sqrt{2}sin(\alpha)cos(\alpha)sin(\beta)(\sigma_{xx}^{PAF} - \sigma_{yy}^{PAF})$$

$$A_2 = \frac{1}{3}\{(cos^2(\beta)cos^2(\alpha)-sin^2(\alpha)(\sigma_{xx}^{PAF}-\sigma_{zz}^{PAF})+(cos^2(\beta)sin^2(\alpha)-cos^2(\alpha)(\sigma_{yy}^{PAF}-\sigma_{zz}^{PAF})\}$$

$$B_2 = -\frac{2}{3}sin(\alpha)cos(\alpha)cos(\beta)(\sigma_{xx}^{PAF} - \sigma_{yy}^{PAF})$$

Terms A_1, B_1, A_2, B_2 in the equation of ω are characterized by $\pm\omega_R, \pm 2\omega_R$ oscillating factors representing effective resonances at integer numbers of spinning frequencies. When the spinning rate ω_R is much greater than the chemical shift anisotropy Δ_{CSA} these terms have a negligible effect on NMR spectrum. However, when $\omega_R \leq \Delta_{CSA}$, these terms create spinning sidebands.

Dipolar coupling formalism Considering the case of dipolar coupling between two spins I and S, the hamiltonian describing this interaction is written in the form:

$$\hat{\mathbf{H}}_D = \frac{\mu_0}{4\pi}\hbar\gamma_j\gamma_k\left(\frac{\mathbf{I}\cdot\mathbf{S}}{r^3} - 3\frac{(\mathbf{I}\cdot\mathbf{r})(\mathbf{S}\cdot\mathbf{r})}{r^5}\right)$$

Moving to spherical coordinates and expanding scalar products, the following expression is obtained:

$$\hat{\mathbf{H}}_D = \frac{\mu_0}{4\pi}\frac{\hbar\gamma_j\gamma_k}{r^3}(A + B + C + D + E + F)$$

where $\gamma_{j,k}$ are the gyromagnetic ratios of the j,k-th spins and r represents the distance between the spins j and k. In particular:

$$A = I_z S_z(3cos^2(\theta) - 1)$$

$$B = -1/4(I^+S^- + I^-S^+)(3cos^2(\theta) - 1)$$

$$C = 3/2(I_zS^+ + I^+S_z)sin(\theta)cos(\theta)e^{-i\phi}$$

$$D = 3/2(I_zS^- + I^-S_z)sin(\theta)cos(\theta)e^{+i\phi}$$

$$E = 3/4(I_+S_+)sin^2(\theta)e^{-2i\phi}$$

$$F = 3/4(I_-S_-)sin^2(\theta)e^{+2i\phi}$$

where $I_\pm = I_x \pm iI_y$ and $S_\pm = S_x \pm iS_y$ are the lowering and raising operators for the I and S spins respectively and the angles θ and ϕ are the polar angles defined in Figure 3.3. To better understand the effects of dipolar coupling it is necessary to move to a rotating frame at the Larmor frequency. Given an hamiltonian in the form $\hat{H} = \hat{H}_0 + \hat{H}_D$, where $\hat{H}_0 = \omega_0\hat{I}_z + \omega_0\hat{S}_z$ represents the Zeeman interaction hamiltonian for spins I and S, in order to move to the rotating frame it is necessary to apply a rotation, described by the propagator $\hat{R}_z(\omega_0 t) = e^{-i\omega_0\hat{I}_z t}$, to the hamiltonian $\hat{H}$ around the quantization z-axis:

$$\hat{H}^* = \hat{R}_z^{-1}(\omega_0 t)\hat{H}\hat{R}_z(\omega_0 t)$$

The initial hamiltonian is then transformed into:

$$\hat{H}^* = -d([A + B] + \hat{R}_z^{-1}(\omega_0 t)[C + D + E + F]\hat{R}_z(\omega_0 t))$$

where $d = \frac{\mu_0}{4\pi}\frac{\hbar\gamma_I\gamma_S}{r^3}$. It is worth noticing that the A, B terms are unaffected by such transformation, while C, D, E, F acquire a periodic time dependence. The best way to deal with this time dependence is by using *average hamiltonian theory*. This allows us to

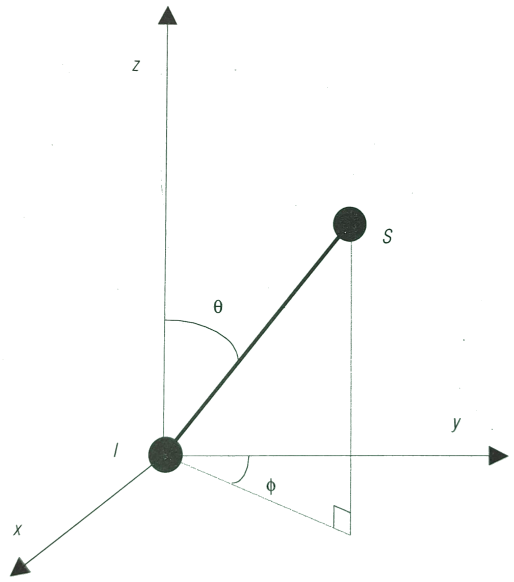

Figure 3.3: Definition of the polar angles θ and ϕ specifying the orientation of I-S internuclear vector with respect to B_0 field which is along the laboratory frame z-axis.

approximate the periodically time-dependent hamiltonian $\hat{H}^*$ as sum of successively high order terms. In particular it can be proven that the lowest order term $\overline{H}^0 = \frac{1}{t_p}\int_0^{t_p} \hat{H}(t)\,dt$ is a sufficiently good approximation for understanding the effects of dipolar coupling hamiltonian. This holds providing that dipolar-coupling interaction in frequency units is small compared to Larmor rotation frequency ω_0 of the rotating frame. This latter is actually called *secular approximation* and can be used in high field regimes where Larmor precession has the fastest dynamics compared to all other interactions. After calculations it is finally obtained the dipolar coupling contribution to the first-order average hamiltonian in the rotating frame:

$$\begin{aligned}\hat{H}_D^{homo} &= -d(3cos^2(\theta)-1)[I_zS_z - 1/2(I_xS_x + I_yS_y)] \\ &= -\frac{d}{2}(3cos^2(\theta)-1)[3I_zS_z - \mathbf{I}\cdot\mathbf{S}]\end{aligned}$$

This is the result obtained for homonuclear coupling. Heteronuclear coupling can be faced in the same way, the only difference relies in the fact that $\hat{R}_z(\omega_0 t)$ acts only on the I spin and the transformed hamiltonian results in:

$$\hat{H}^* = -d(A + \hat{R}_z^{-1}(\omega_0 t)[B + C + D + E + F]\hat{R}_z(\omega_0 t))$$

whose first order hamiltonian in high field regime (secular approximation holding) leads

to

$$\hat{H}_D^{hetero} = -d(3cos^2(\theta) - 1)I_z S_z$$

It is worth pointing out that in average hamiltonian theory all interactions that, once transformed, present time dependence are completely averaged out during the time period t_p (representing MAS rotation period). To better understand why B-term containing $\mathbf{I} \cdot \mathbf{S}$ has no influence on the first-order hamiltonian for heteronuclear coupling one can think that this term represents the effect of transverse components of the local field due to spin S. In general, transverse magnetic fields (as in the case of simple RF pulses) have no effects on spin systems when these are out of resonance with respect to the Larmor frequency of nucleus I. In case of heteronuclear coupling the two involved nuclei precess at different Larmor frequencies thus the B term disappear. Conversely, in homonuclear dipolar coupling, since the two involved nuclei are of the same species, Larmor frequencies are the same and, as a consequence, B term is present.
As final remark, a general rule that can be extracted is that every interaction that can be described by a rank-2 spherical tensor is characterized by the presence of the term $(3cos^2(\theta) - 1)$ in the first-order average hamiltonian. Knowing that θ is a fixed quantity (in the laboratory frame) representing the angle between the quantization axis and the rotation axis of the sample, by setting $\theta = 54.7°$ (magic angle) it is possible to suppress all these rank-2 interactions.

3.3. Effects of homonuclear and heteronuclear dipolar coupling

Consider for simplicity the case of two spin-1/2. Before any dipolar coupling is introduced, the energy levels are represented as shown in Figure 3.4.

Homonuclear coupling The first-order average hamiltonian for homonuclear dipolar coupling is characterized by terms containing operators $I_z S_z$ and $\mathbf{I} \cdot \mathbf{S}$ having different effects on the energy levels:

- $I_z S_z$ produces a first-order correction of energy to all the states. For example, it causes an energy shift of $\frac{\mu_0}{4\pi}\frac{\hbar\gamma_j\gamma_k}{r^3}(3cos^2(\theta) - 1)\langle\alpha\alpha|I_z S_z|\alpha\alpha\rangle$ for the $|\alpha\alpha\rangle$ state. The eigenfunctions of this operator are simply product Zeeman states $|\alpha\alpha\rangle, |\alpha\beta\rangle, |\beta\alpha\rangle, |\beta\beta\rangle$
- $\mathbf{I} \cdot \mathbf{S}$ contains $|I_+ \otimes S_- + I_- \otimes S_+|$ spin operator term, associated to a matrix of the

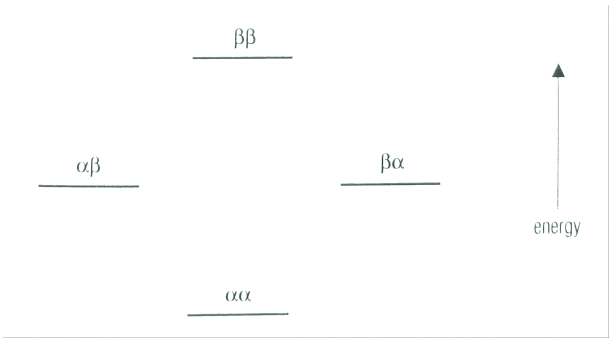

Figure 3.4: The energy levels and wavefunctions in a two spin-1/2 system before dipolar coupling is considered i.e. Zeeman levels. The $\alpha\beta$ and $\beta\alpha$ levels are degenerate in a homonuclear spin system and are mixed by dipolar coupling.

form

$$\mathbf{B} = -1/2(3cos^2(\theta) - 1) \begin{bmatrix} 0 & 0 & 0 & 0 \\ 0 & 0 & 1 & 0 \\ 0 & 1 & 0 & 0 \\ 0 & 0 & 0 & 0 \end{bmatrix}$$

This tensor is obtained by the application of tensor product between Pauli matrices describing operators $\mathbf{I} \cdot \mathbf{S}$. This has the effect of mixing the $|\alpha\beta\rangle, |\beta\alpha\rangle$ states. Hence the eigenfunctions are linear combinations of $|\alpha\beta\rangle, |\beta\alpha\rangle$. In general, for many-spin systems, $\mathbf{I} \cdot \mathbf{S}$-type terms in the homonuclear dipolar coupling will mix degenerate Zeeman levels, bringing to eigenfunctions for the multispin system which are linear combinations of degenerate Zeeman levels. This has as immediate consequence the energy splitting of degenerate states resulting in many different transition frequencies whose selection rules are $\Delta M = \pm 1$.

From this, it is possible to see that even without molecular orientation dependence there is a huge range of transitions that cause line broadening of the spectrum. In particular, for large enough spin systems the lineshape approximates a gaussian.

It is worth noting that since eigenstates are linear combinations of $|\alpha\beta\rangle, |\beta\alpha\rangle$ states, by performing repeated observations on (ideally) one particular spin, the wavefunction will collapse into one of the many $|\alpha\beta\rangle, |\beta\alpha\rangle$ states. This means that sometimes we will measure state $|\alpha\rangle$, sometimes state $|\beta\rangle$ for the same spin. Such fluctuations on the same spin will make it look like it is constantly changing its spin function, meaning that a continual exchange of longitudinal magnetization is occurring.In particular, in the case of multispin system, during these transitions, the total z-component of spin $M = m_1 + m_2 + m_3 + ...m_N$ is conserved, but individual spin components m_i are allowed to vary.

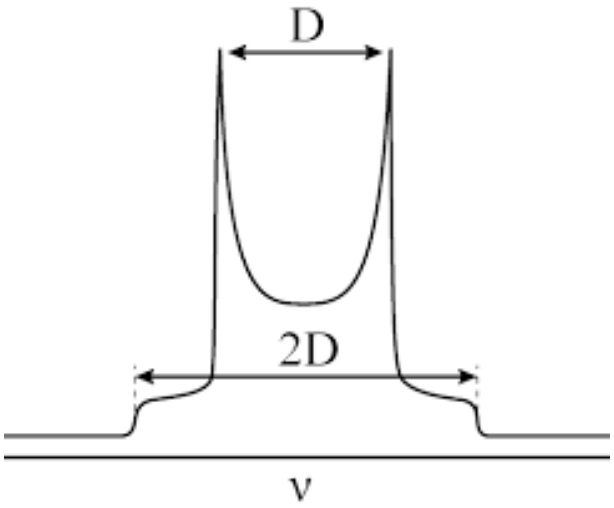

Figure 3.5: Representation of powder spectrum of coupled spins.

Heteronuclear coupling Line broadening due to $\mathbf{I} \cdot \mathbf{S}$-like terms is now absent and no mixing of spin states is expected. As a consequence spin states remain unchanged from the initial Zeeman states. The resulting dipolar contributions to the energy levels of the IS spin system are therefore:

$$\begin{aligned} E_D^{hetero}/\hbar &= \langle Im_I; Sm_S|\hat{H}_D^{hetero}|Im_I; Sm_S\rangle \\ &= -d(3cos^2(\theta) - 1)m_I m_S \end{aligned}$$

where m_I, m_S are the z-components of spin for spin I and S. From selection rule $\Delta m_I = \pm 1$ for I spectrum and $\Delta m_S = \pm 1$ for S spectrum it is possible to retrieve the transition frequencies of both dipolar-coupled nuclei:

$$\omega_D^I(\theta) = \omega_0^I \pm 1/2d(cos^2(\theta) - 1)$$

where ω_0^I is the transition frequency in absence of coupling.
If both I and S are spin-1/2 nuclei, there are two I spin (and two S spin) transitions each with a $(3cos^2(\theta) - 1)$ dependence, and so for powder samples each gives rise to the powder spectrum. However one transition has a $+(3cos^2(\theta) - 1)$ while the other has a $-(3cos^2(\theta) - 1)$ dependence, so the powder pattern reported in Figure 3.4 is given by the superposition of two mirrored powder spectra.

Heteronuclear spin dipolar-coupled to a homonuclear network of spins A particular case of heteronuclear dipolar coupling occurs when a spin I is coupled to a spin S

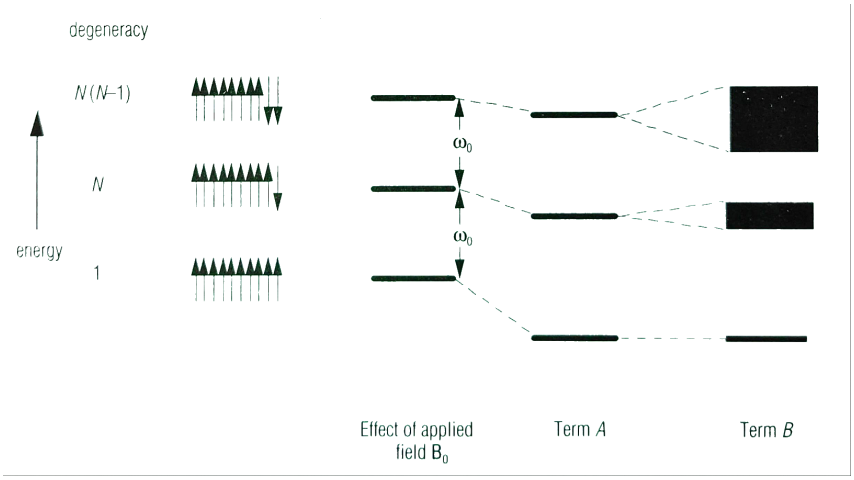

Figure 3.6: In an N-spin, homonuclear system, there may be many Zeeman levels with the same M quantum number ($M = m_1 + m_2 + ... + m_N$); these are degenerate in absence of dipolar coupling. Dipolar coupling has the effect of mixing these degenerate states and splitting their energy.

which is in turn part of a homonuclear coupled network of S spins. Suppose S_1 to be the closest spin to I and therefore the most strongly coupled to it. As previously discussed, because of the presence of homonuclear-coupled S spin network, longitudinal magnetization changes after repeated observation. It is evident that due to I-S heteronuclear coupling, such fluctuations will have an effect on the I spin leading to line-broadening in its spectrum, reminiscent of those expected in the S spin spectrum.

Heteronuclear decoupling Broadening due to heteronuclear coupling between a low-γ nucleus and an high-γ one, coupled to a network of high gamma nuclei, can worsen an already weak spectrum even under the use of MAS. Fortunately, this effects can be removed by RF irradiation.
Specifically *high-power decoupling* is the simplest technique able to remove heteronuclear coupling effects. In order to have a immediate idea of how this technique works, consider a system made by ^{13}C coupled to ^{1}H, which is homonuclearly coupled to a network of ^{1}H. The method consists of applying continuous irradiation of very high power at the proton Larmor frequency. This pulse is has to be applied during acquisition of the ^{13}C FID. Because of homonuclear coupling between protons, the effects of an RF pulse applied to any of the ^{1}H nuclei present in the network are propagated between all the coupled nuclei. This can be understood considering that the RF radiation affects the z-component of the "bombarded" nucleus which, due to homonuclear dipolar coupling, will affect all the other z-components of the nuclei that are interacting with it. From a more formal

point of view it is possible to say that the RF pulse causes ^1H spins to undergo repeated transitions $\alpha \leftrightarrow \beta$ with a rate dependent on the amplitude on the RF pulse ω_1. After this consideration, from now on, power will be expressed in kHz. From equation for E_D^{hetero} there is a dependence on m_H, the z-component of spin of proton in the dipolar coupled spin pair. By applying an RF pulse on ^1H nuclei the average z-component of that specific nucleus will be averaged out and consequently, heternuclear dipolar coupling too. However, in real samples molecular motion can interfere with heteronuclear decoupling. If molecular motion occurs on a similar timescale (i.e. the inverse of correlation time is comparable with decoupling RF frequency), an interference between the two decoupling process will occur resulting in an increase of the spectrum broadening. Based on the same idea, if high-power decoupling is used simultaneously with MAS (i.e. the amplitude of the pulse is comparable with the spinning frequency) the two decoupling methods (RF pulse and MAS) can interfere making decoupling ineffective. This can leave the spectrum unchanged, or reduce the peak intensity and increase of peak broadening. This will be in contradiction to the expected line narrowing. Precisely, for very high spinning rates $\geq 40kHz$ it can be more effective to use *low-power decoupling* adopting SPINAL 64 as decoupling pulse sequence rather than simple continuous wave pulse on proton channel.

3.4. Cross-polarization

Cross-polarization is used to help in observing low concentrated spins and retrieve information on which spins that are in close spatial proximity. Observing dilute spins presents two main issues:

1. Low abundance of nuclei means that signal to noise is very small
2. Longitudinal relaxation times of low abundance nuclei tend to be very long. This because strong homonuclear dipolar network interactions, which can stimulate relaxation transitions, are largely absent. Only weaker heteronuclear dipolar interaction are present.

Both problem can be solved using a pulse sequence of the form shown in Figure 5.9 on which the dilute nucleus X derives its magnetization from a close network of abundant and highly sensitive spins (generally ^1H nuclei).

3.4.1. Theory of cross-polarization(CP)

A proper formal explanation of cross-polarization involves the use of average hamiltonian theory [51], but, for the scope of this work, it is not necessary to know all details. There are, however, several considerations that can be made, on all that cross-polarization transfer is mediated by heteronuclear dipolar interaction between ^1H and X spins. In order to explain such process we need to move into a *double rotating* frame where ^1H (and X) spins are in a frame that rotates about B_0 at the frequency of ^1H (and X) RF radiation exactly on resonance for the spins to which they are applied.
An initial 90°_x pulse rotates ^1H equilibrium magnetization toward -y axis and an on-resonance, -y ^1H *contact pulse* is then applied. This last applied field is known as the *spin lock field* $\mathbf{B}_1(^1H)$ and acts to keep the ^1H magnetization along -y direction. Since spin-lock pulse is on ^1H resonance it acts also as quantization axis for spin states during contact pulse. New spin states, also called *rotating frame states*, for ^1H are then created and labeled α^*_H, if parallel, and β^*_H, if antiparallel with respect to $\mathbf{B}_1(^1H)$. In a similar way a contact pulse is also applied on the X-channel generating a field $\mathbf{B}_1(X)$ that introduces a quantization axis for X spins and creates new Zeeman states α^*_X, β^*_X.
In order to work, cross-polarization has to fulfill so-called $Hartman - Hahn\ matching\ condition$ for which $\mathbf{B}_1(^1H)$ and $\mathbf{B}_1(X)$ have to be tuned according to

$$\gamma_H \mathbf{B}_1(^1H) = \gamma_X \mathbf{B}_1(X)$$

This condition brings the energy gaps between the spin states of ^1H and X spins to be equal within the doubly rotating frame.
Dipolar coupling operator describing interaction between these two nuclei has form $\hat{H}_{HX} = -\sum_i d_i(3cos^2(\theta_i) - 1)\hat{I}^H_{iz}\hat{S}^X_z$, considering each single coupled i-th nuclei of ^1H. This operator is unaffected by rotations about z-axis due to the presence of $\hat{I}^H_{iz}, \hat{S}^X_z$ terms. Now, considering that both ^1H and X spins are quantized in directions perpendicular to z, dipolar coupling cannot affect the energy of the system in the rotating frame, since the energy of the system is determined by fields that are parallel to the quantization axis (which thanks to $\mathbf{B}_1(^1H)$ and $\mathbf{B}_1(X)$ is now lying in the xy-plane) and, as a consequence, dipolar coupling is not allowed to alter net polarization. So dipolar coupling operator couples the ^1H and X nuclei and acts in such a way to preserve energy and net magnetization of the system. When Hartman-Hahn matching condition is met, the energy gaps between ^1H and X rotating frame spin states are equal, so a transition involving the absorption of a radio frequency photon is compensated by a transition emitting a photon of the same energy on the other nucleus. Dipolar coupling causes then a redistribution of energy between the two heteronuclei keeping the energy of the system constant and due

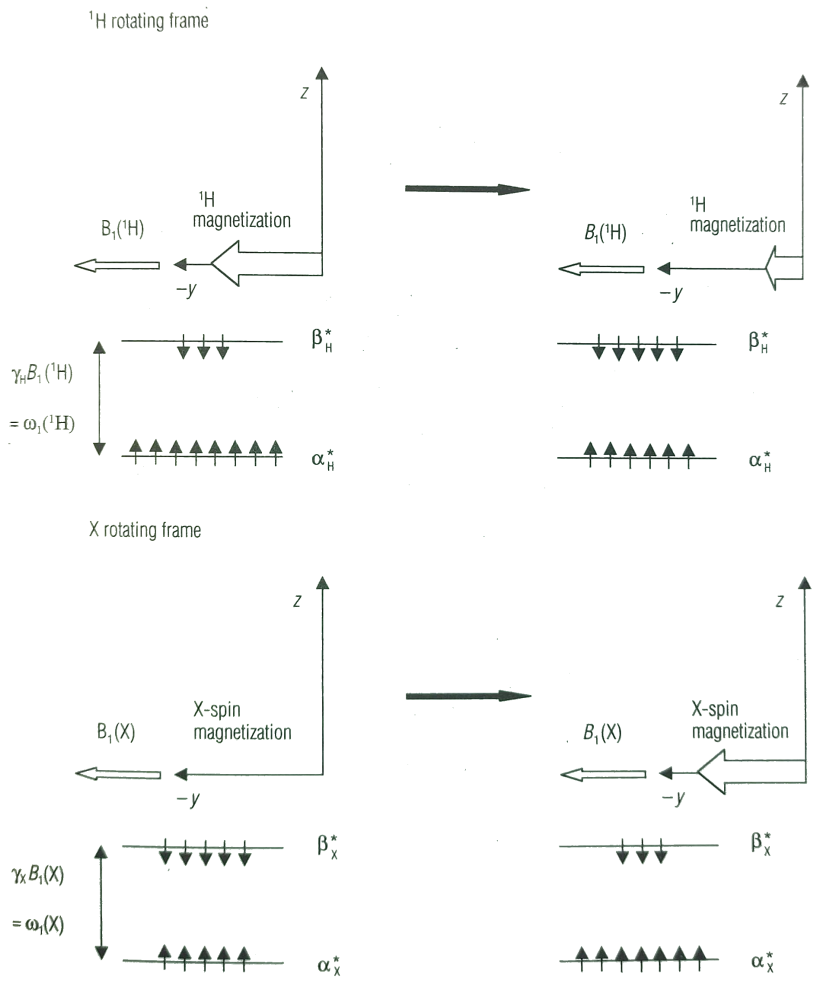

Figure 3.7: Schematics of CP experiment.

to the fact that every transition is counterbalanced, the net polarization of the system has also to be preserved. In particular the nature of this energy redistribution depends on the initial distribution of spins over the rotating frame states.

It is finally worth noticing that the ^1H longitudinal magnetization, which is now lying on the -y axis, is too big compared to the much smaller spin-lock field $\mathbf{B}_1(^1H)$. ^1H magnetization will then reduce over time by the presence of $\alpha^*_H \rightarrow \beta^*_H$ transition, simultaneously X magnetization will build up due to balancing $\beta^*_X \rightarrow \alpha^*_X$ transitions.

The detailed dynamics of cross-polarization are complicated, especially under MAS [56], [21]. The initial transfer involves closest ^1H and X spins and in case of isolated spins, magnetization oscillates back and forth at a rate determined by the dipolar coupling strength. If a ^1H network of spin is also present, subsequently the ^1H magnetization redistribute among this network and recharges the ^1H spins close to X nuclei so that the coherent transfer continues. One of the complications is related to the fact that the spin-locked ^1H magnetization will inevitably decrease due to loss of coherence guided by

a characteristic time constant $T_{1\rho}$ reducing the efficiency of polarization transfer.
The rate of magnetization transfer in cross-polarization transfer depends on the strength of heteronuclear coupling which is influence by the distance between the two coupled nuclei by a factor $1/r^3$. The rate of transfer will thus be higher for closer nuclei. Last effect that can influence the rate of transfer is how quickly the ^1H magnetization redistributes across the homonuclear coupled ^1H network; this is usually assumed to be very fast due to the high strength of the ^1H-^1H coupling. Finally, it is worth saying that anything that can disrupt dipolar coupling, such as molecular motion or magic angle spinning (specifically if the spinning frequency is comparable to dipolar coupling in frequency units), can make cross-polarization really unlikely to happen. To compensate inefficiency related to magic angle spinning, variable-amplitude contact pulses can be used on one of the two spins. Commonly used pulses have ramped shape being more robust under mismatches of Hartman-Hahn matching condition. Finally, magic angle spinning modifies Hartman-Hahn (zero-quantum) matching condition in the following way:

$$\gamma_H \mathbf{B}_1(^1H) - \gamma_X \mathbf{B}_1(X) = \pm n\omega_r$$

where ω_r is rotor spinning frequency and n is an integer number. This shows that polarization transfer, once$\omega_1 = \gamma_X \mathbf{B}_1(X)$ is fixed, can be in principle obtained for an infinite number of resonance frequencies on the ^1H channel, but in real experiments only $n = \pm 1, \pm 2$ resonances are observed.

3.4.2. Magic angle spinning influence on CP

In presence of MAS heteronuclear dipolar coupling can be averaged out depending on the spinning frequency with respect to the coupling strength. In principle, $^1H - X$ CP is expected to lead to a signal enhancement on X nucleus equal to $\frac{\gamma_{1_H}}{\gamma_X}$ but MAS and non idealities in the experimental apparatus can compromise this sensitivity amplification. In addition, at high spinning frequency, a new type of matching condition may arise in addition to conventional: double-quantum matching condition conditions.

$$\gamma_H \mathbf{B}_1(^1H) + \gamma_X \mathbf{B}_1(X) = n\omega_r$$

This particular regime of CP is reached when spinning frequency becomes higher than the power applied on the X nucleus as reported in Figure 3.8b. In case this matching condition is fulfilled, on X nucleus, a negative intensity signal builds up. As final remark, in order to increase CP efficiency, several strategies can be adopted. Using ramps that span over a narrower range of powers will make the involved nuclei feel for a longer time a power

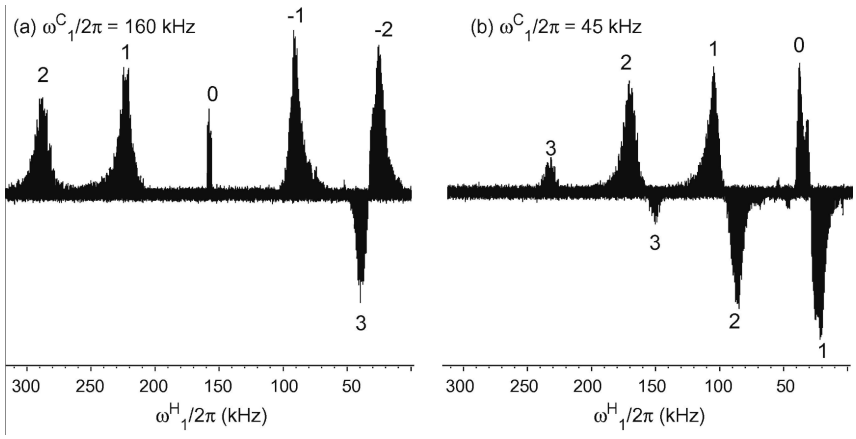

Figure 3.8: ^{13}C CP profiles of 2-(^{13}C)-l-alanine at 68 kHz MAS. The intensity of the C_α carbon signal is monitored in a CP experiment (1 ms contact time) where the field strength $\omega_1^C/2$ on the carbon channel is set to 160 kHz (a) or 45 kHz (b), and proton rf-field strength $\omega_1^H/2$ is varied from 320 to 2 kHz [21].

closer to the needed matching condition leading to a CP signal intensity improvement. This also will have the effect of narrowing the matching conditions resonances during the acquisition of the matching curve due the higher selectivity. In particular, in the case of a 90-100 ramp for example, power applied on one of the two nuclei involved CP is spun between 0.9 and 1.0 of the maximum value of the power applied to the channel. This means that, in case a maximum in signal intensity is recorded in the matching curve, the actual optimal power corresponds to 0.95 times the value of the measured optimal power. Another way to improve CP efficiency is to perform experiments at lower temperature. This will reduce molecular motion, increasing the strength of dipolar coupling. As a consequence of this a more efficient polarization transfer process is expected. Finally, depending on the involved nuclei (i.e. quadrupolar nuclei) dedicated pulse sequences which are different than the conventional one previously explained can be used [5], [39].

4 | Electrochemical characterization

4.1. Electrochemical characterization and cycling of NMC622 and silicon electrodes

Before running experiments on ex-situ samples, electrochemical characterization has been performed on both silicon and NMC622 electrodes. Specifically, electrode material was provided by LITEN laboratory (CEA) and consisted of NMC622 cathodes with areal load of 26.13 $mg\ cm^{-2}$, deposited on Al current collector. Silicon nanoparticles were used as active anodic material on Cu current collector with the addition of a binder (PAA 15%), and active carbon (CNTs 0,67%). The latter additives were used in order to in order to increase the adhesion between particles and improve conductivity guaranteeing efficient current collection. The net areal of the anode load is 4.80 $mg\ cm^{-2}$.
The used electrolyte was $LiPF_6$ 1M in EC:DEC 1:1 with 10% FEC and 2% VC. Ex-situ samples were then prepared using a coin cell configuration. Half cells (NMC/Li and Si/Li) were cycled in order to characterize the electrode material and derive specific capacity of both anode and cathode. After this, full cells were assembled and galvanostatic cycling at constant current was ran.
Since the aim of the project is based on calibration and optimization of ex-situ NMR experiments for further operando NMR measurements, also operando NMR cells were assembled and cycled in order to verify the capability of such kind of cells to sustain electrochemical measurements.

Coin cells NMC622 and silicon electrodes were punched with a circular shape of 14 mm diameter, dried for one night in a Büchi oven at 100° C under vacuum and then transferred into a glove box under Ar atmosphere. Celgard 2325 separator was punched in circles of 16 mm diameter, dried into a Büchi oven at 60°C under vacuum for two days and put into a glove box. Both half and full cells were assembled under Ar atmosphere

inside a glove box according to the scheme showed in Figure 4.1.

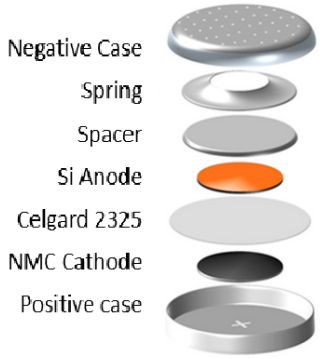

Figure 4.1: Schematic of full coin cell.

In the case of NMC and silicon half cells, Li electrodes were punched directly inside the glove box in circles of 15 mm diameter and used as anode while for NMC and as cathode for silicon. 20 μL of electrolyte were added in two stages: below and on top the Celgard separator (in total 40 μL of electrolyte). As final remark, in order to have better electrical contact between current collector and external cycling circuit, 3 steel spacer were used in NMC-Li half cell and 2 spacers were used in Si-Li half cell (due to the higher thickness of silicon electrodes) hence increasing mechanical pressure inside the battery. Once coin cells were assembled, they were galvanostatic cycled under constant current.
During galvanostatic cycling a constant current is applied to the cell and voltage across the cell is measured versus time. External current is applied until an upper (lower) threshold voltage is reached by the NMC half cell (Si half cell) and once this happens the polarity of the current is reversed. Again, external current flows through the battery until a lower (upper) threshold voltage is reached by the NMC half cell (Si half cell) and once again current polarity is reversed and a new charge-discharge cycle begins. In case the cell is not able to reach the desired threshold voltage under constant current, current polarity is anyway reversed after a well defined amount of time. Both half and full cells were cycled using C/20 cycling rate, meaning that the external applied current is calculated in such a way that, during the first charge, the theoretical capacity is accumulated in the anode after 20 hours.
The current that has to be applied to the cell is defined by the lowest capacity electrode and depends on the mass of the active material involved. The latter is simply given by multiplying the areal load and the surface of the electrode itself. Finally, the theoretical capacity that can be stored in the electrode material is calculated as:

$$C_{th} = m_{el}\ C_{th}^{spec}$$

Theoretical specific capacities of used electrodes are $C_{th,Si}^{spec} = 3570 mAh\ g^{-1}$ for silicon while for NMC $C_{th,NMC}^{spec} = 200 mAh\ g^{-1}$. Finally in lithium metal $C_{th,Li}^{spec} = 3860 mAh\ g^{-1}$. Knowing masses of active electrode material $m_{NMC} = 26.2\ mg$, $m_{Si} = 7.4\ mg$, $m_{Li} = 5.3\ mg$ it is possible to evaluate all C/20 rates needed as shown in Table 4.1.

	maximum theoretical capacity [mAh]	C/20 rate [mA]
NMC-Li	5.23	0.26
Si-Li	26.42	1.32
NMC-Si	5.23	0.26

Table 4.1: Cycling rates used for galvanostatic cycling in half and full cells.

NMC-Li half cells were cycled in a potential range from 3 V to 4.2 V while for Si-Li half cells a potential range from 0 V to 1 V was used.

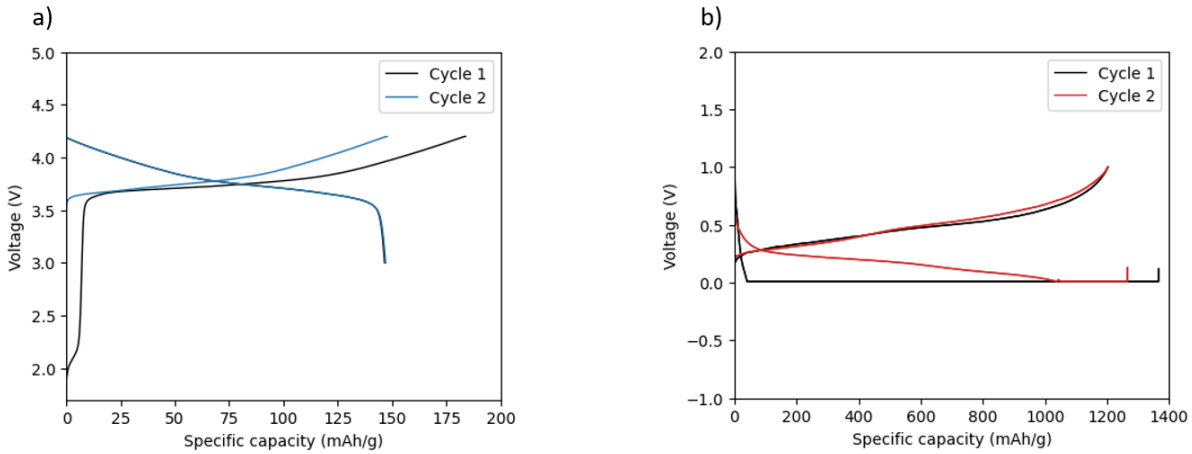

Figure 4.2: a) electrochemical cycling data of NMC-Li half cell b) electrochemical cycling data of Si-Li half cell. Both cells were ran at ambient temperature and atmosphere. Here reported two cycles at C/20 rate.

The choice of using C/20 cycling rates lies in the fact that at such applied current we expected to see a gradual and stable formation of the SEI. For instance, this particular kind of cycles are called formation cycles.
Electrochemical characterization shows that for NMC-Li half cell we were able to retrieve a first charge specific capacity of 180 $mAh\ g^{-1}$ while for Si-Li half cell a first charge

capacity of about 1300 $mAh\ g^{-1}$ was measured as shown in Figure 4.2. In the case of the Si-Li half-cell, the greater thickness of the electrode material makes Li-ion diffusion more challenging. As a result, the cell exhibits higher resistance, causing the voltage to quickly reach the 0 V threshold. To prevent lithium plating while still allowing lithiation, a voltage hold at 0,05 V is applied. During this phase, the current gradually decreases until it reaches a lower cut-off, set at half the applied C-rate. To better compensate for the cell strong capacity retention, this cut-off should have been set at a lower value, ensuring continuous alloying throughout the voltage hold period and avoiding lithium plating.
Once electrode were characterized, a full Si-NMC cell was assembled and cycled with a C/20 cycling rate for 10 cycles in order to maximize the SEI formation.

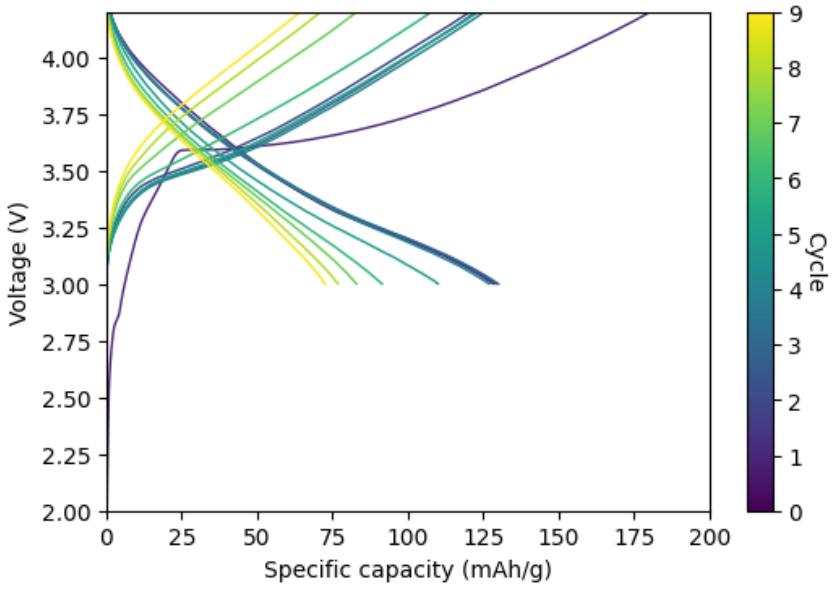

Figure 4.3: Electrochemical cycling data of NMC-Si full cell. Here reported ten cycles at C/20 rate.

Capacity fade is an evident issue for this kind of cell due to the use of C/20 cycling rate. At this current, the most favored thermodynamical process involved is SEI formation and consequently a progressive loss of active Li ions is observed as illustrated in Figure 4.3. These ions specifically form organic and inorganic components of the SEI.

NMR ex-situ sample preparation Before running ex-situ NMR experiments, the full coin cell in a delithiated stage was disassembled using a decrimper without being rinsed from residual electrolyte. Active anode material was scratched away from the copper current collector and inserted into a 1.3 mm rotor already filled with teflon into a glove box under Ar atmosphere. The choice of using a 1.3 mm rotor and teflon filling was

dictated by the expected small quantity of material obtained after electrochemical cycling ($\sim$ 3 mg).

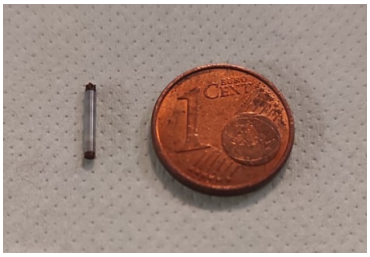

Figure 4.4: 1.3 mm rotor filled with ex-situ sample.

Operando NMR cells In addition to coin cells, an operando NMR cell was also assembled and cycled to confirm that this specific battery configuration can support electrochemical cycling. The electrode materials, separator, and electrolyte used in the operando cells were the same as those in the coin cells. However, unlike coin cells, the operando cell featured rectangular-shaped electrodes and a separator. Electrodes were cut with surface 1.4x0.4 cm^2 while separator was cut with 1.5x0.5 cm^2 surface. Before assembly into a glove box, all capsule cell components were dried for one night into a oven at 60° C temperature.

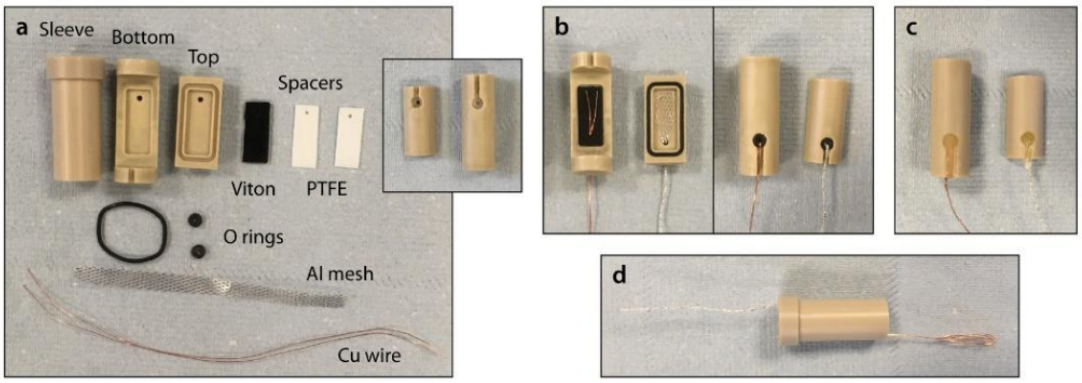

Figure 4.5: Images of the operando NMR cell utilized in this study. (a) The capsule cell along with its additional components; the inset displays the reverse side of the top and bottom pieces. (b) The bottom piece is equipped with spacers and two thin copper wires, while the top piece is fitted with an O-ring and an aluminum mesh (left image). Small O-rings are placed inside the current collector holes (right image). (c) The current collector holes are sealed using epoxy glue. (d) The fully assembled cell after completion inside a glove box under Ar [37].

Figure 4.5 illustrates the conventional assembly of an operando cell. In this work, rolled

Cu mesh was used both as a wire on one side and as a current collector junction on the other, ensuring a reliable electrical connection between the Cu anode current collector and the Cu mesh. Additionally, only a single layer of Teflon was used in the assembly, and a smaller amount of electrolyte (30 μL in total, distributed above and below the Celgard separator) was employed. Unlike the setup in Figure 4.5, the operando cell shown in Figure 4.6b does not include O-rings or Cu wires.
Since the area of active material is different from the case of coin cells, also the external current applied to the cell has changed. Specifically for a full NMC-Si full cell a C/20 cycling rate of 95μA was used at room temperature.

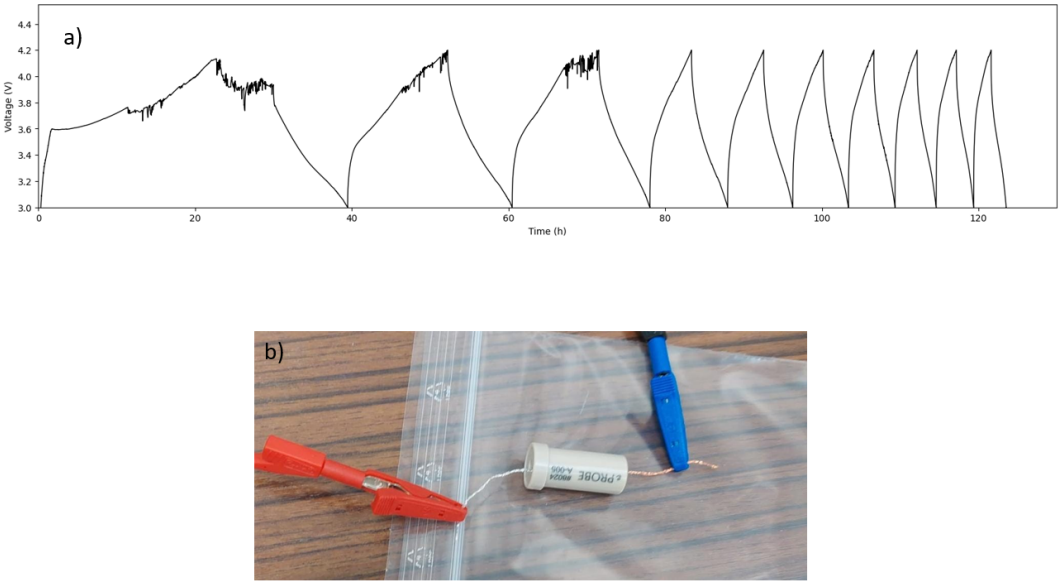

Figure 4.6: a) NMC622-Si operando cell galvanostatic cycling data at C/20 rate and room temperature b)Physical operando cell under cycling at room temperature.

The electrochemical cycling data in Figure 4.6a reveal an imperfect assembly, as indicated by unusual features during the initial cycles, likely caused by a loss of electrical contact. This outcome suggests that the assembly procedure is not yet fully optimized, which is expected given that this approach is less established compared to coin cells. After three cycles, the charge and discharge processes stabilize; however, noticeable capacity fade continues to affect the cell. Overall, these results highlight the need for further optimization of the cell assembly to guarantee reliable performance in future operando NMR experiments.

5 | ssNMR Experimental methods

5.1. Experimental setup

In this section are presented the experimental apparatus and methodologies regarding solid state NMR experiments that were adopted in this work. The nuclei excited were ^1H and ^7Li characterized by a Larmor frequency of 200 MHz, 77.8 MHz respectively. All experiments were performed on a 200 MHz Bruker Avance III spectrometer using a double channel probe H-X with magic angle spinning (MAS) and variable temperature (VT) facilities.

Spectrometer

NMR spectrometer reported in Figure 5.4 is characterized by:

- ^1H channel (yellow)
- ^7Li channel (blue)
- Bearing gas (red)
- Drive gas (green)

From the physical point of view, both channels ^1H and ^7Li are cables connected to a preamplifier (right bottom in Figure 5.4) in turn connected to an amplifier. Due to the fact that NMR signal is extremely weak, in the order of nanovolts or microvolts, the preamplifier is used to amplify the analog signal coming from the probe without introducing too much noise. After the preamplifier, the signal is further amplified by a main amplifier to ensure that the detected signal is strong enough to be processed by the data acquisition system. For multi-channel NMR probes it is essential to implement filters on the RF channels in order to ensure clean and efficient signal transmission and reception according to the scheme shown in Figure 5.1. In a more detailed way, filters prevent interference between different transmission and reception channels, ensuring efficient coupling between nuclei without distortion. In particular, for multi-nuclear experiments band-pass filters are used to select only the frequency range coming from a specific nucleus, reducing

interference. Finally, filters also protect the receiver from overloading or damage due to the high power of the transmitted RF pulse.

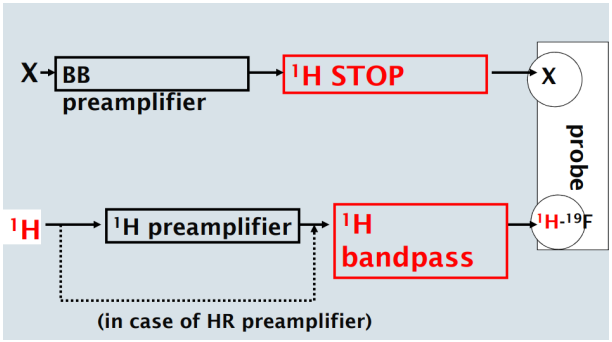

Figure 5.1: Schematics of filters.

Since X channel is the one on which detection is performed, it is necessary to apply a spike-filter such that no contribution from ^1H can interfere. For what concerns ^1H channel, due to the lower Larmor frequency of the X channel compared to the one of ^1H, a band pass filter is also sufficient.

MAS and VT

In order to run MAS experiments bearing and drive gas lines pumping compressed air have to be connected to the probe as shown in Figure 5.2. Precisely, bearing gas acts on the rotor making it float in order to ensure frictionless spinning. Simultaneously drive gas on the wings of the rotor makes the latter rotate. In particular, in order to guarantee stable spinning at 40 kHz on a 1.3 mm rotor (the one that will be used for all next MAS experiments) bearing and drive gas pressures have to be set to 3000 mbar and 1100 mbar respectively.

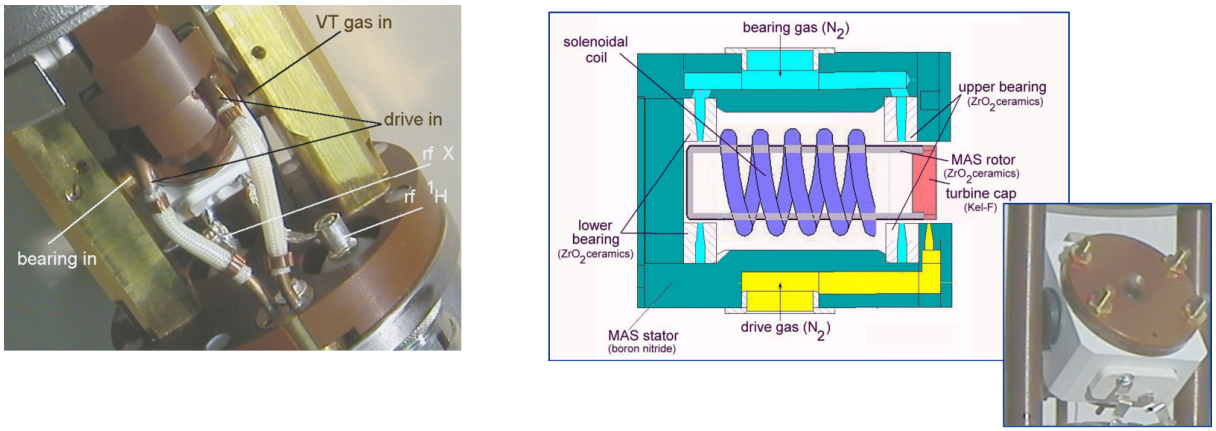

Figure 5.2: Schematics of MAS gas lines.

It is worth noticing that on the used probe VT facility is present. N_2 flows through a chiller that decreases its temperature and is then sent to a heater directly collocated on the probe that adjusts the gas temperature in order to bring the sample to the desired one. Target temperature is reached by setting proper gas flow. In particular, the lower the target temperature the higher the gas flow so that heat exchange of N_2 with the environment is less likely to happen.

Wobbing

Finally, considering that NMR probes are characterized by RF coils behaving as both transmitters and receivers of signal, in order to run experiments on resonance, such that the power of RF pulses is fully transferred to the sample, so called wobbing has to be done. The resonant overall LC circuit of the probe has to be tuned in order to produce a resonance frequency identical to the Larmor frequency of the RF pulse used to excite desired nuclei for both ^1H and ^7Li channels. This is manually done by screwing so called matching and tuning rods until the minimum of wobble curve of reflected power falls exactly at the Larmor frequency of the interested nucleus as shown in Figure 5.3.

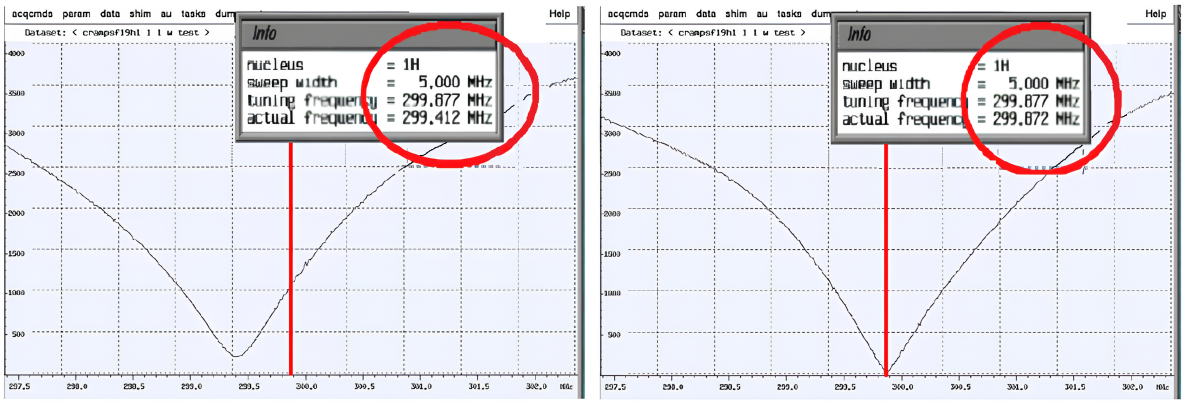

Figure 5.3: Example of not tuned (left) and tuned (right) probe on a 300 MHz NMR spectrometer.

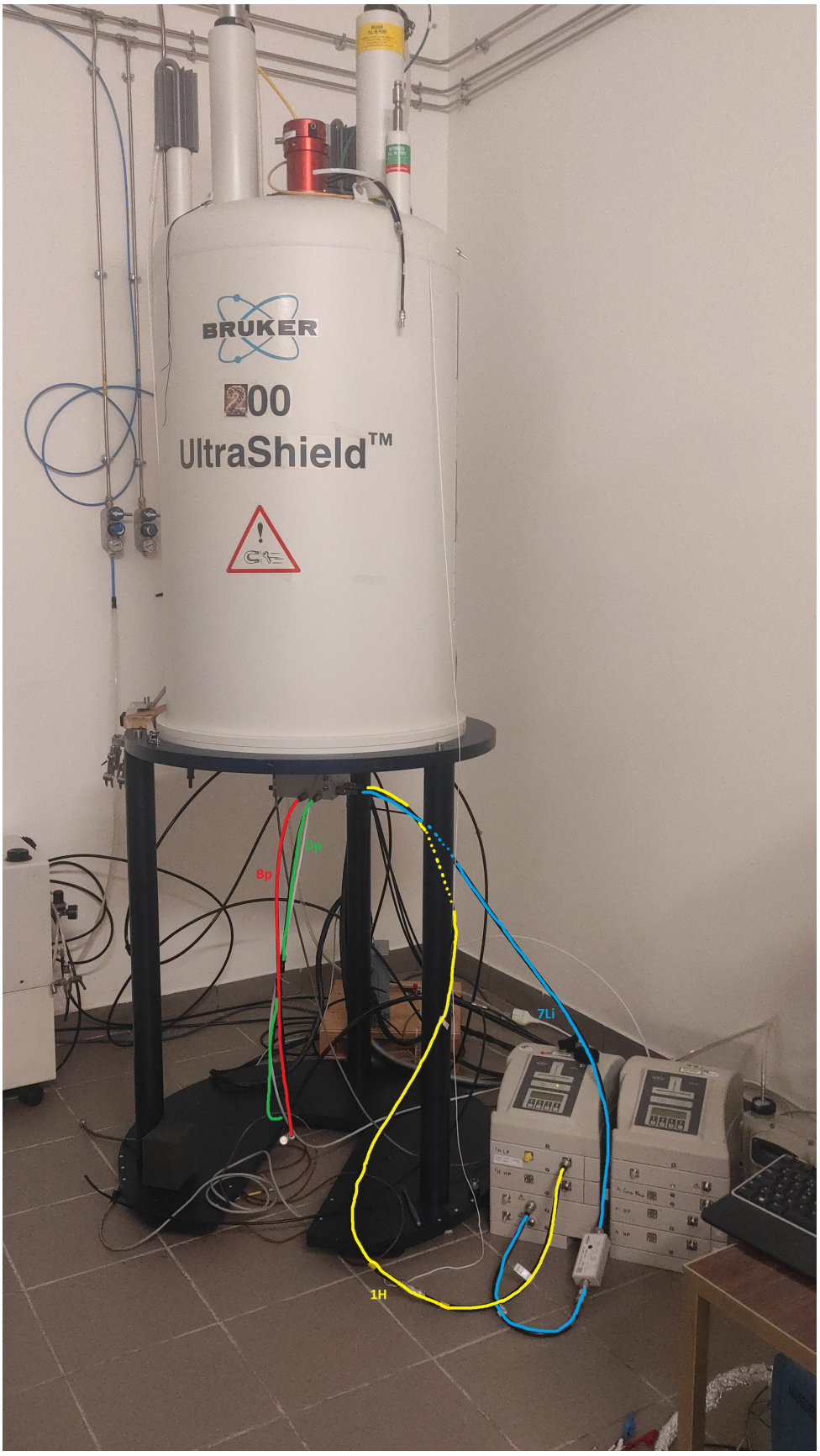

Figure 5.4: 200 MHz NMR spectrometer with MAS and VT facilities.

5.2. 90° pulse length calibration

Such kind of experiments require one single channel to be irradiated and use the following pulse sequence scheme characterized by so called presaturation and 90° pulses as shown in Figure 5.5.

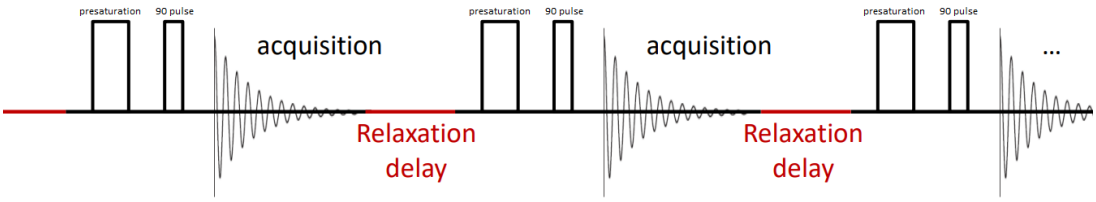

Figure 5.5: Pulse scheme used for ^{7}Li pulse calibration.

Presaturation has the role of randomize the spin system in order to guarantee reproducibility between consecutive scans while the 90° pulse is used to rotate the longitudinal magnetization by a 90° angle. This builds up the transverse magnetization and after this, free induction decay of the system is recorded. Due to low intrinsic sensitivity of ssNMR spectroscopy, this procedure is applied as many times as defined by the number of scans. This process is aimed at summing signal contributions and averaging out noise over time. From the practical point of view, once the power of the pulses is set for both pulses it is necessary to calibrate the duration of the 90° pulse such that the magnetization is effectively rotated by 90° onto the transverse plane. This is achieved by running consecutive experiments in which the duration of the 90° pulse is progressively varied as shown in Figure 5.6.

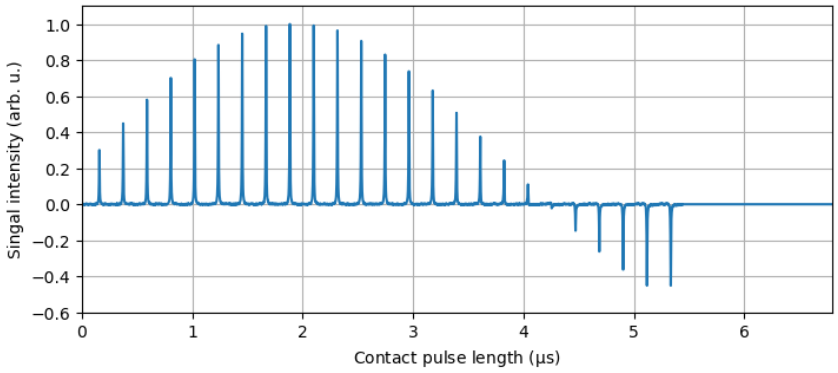

Figure 5.6: 90° pulse calibration on Li citrate

The obtained result represents the so called nutation curve from which the optimal 90° pulse length is derived by looking at which duration the signal intensity is approximately

zero. This value defines the duration of the 90° pulse such that rotates longitudinal magnetization by an angle of 180°. As a consequence no transverse magnetization is built up hence no signal is detected. The optimal 90° pulse duration is thus calculated as:

$$t_{90} = \frac{t_{180}}{2}$$

Furthermore this measure allows to calculate the nutation frequency of a nuclei at a fixed power:

$$\nu_{nut} = \frac{1}{2t_{180}}$$

This value defines which is the frequency at which the equilibrium magnetization rotates around the RF 90° pulse axis for a fixed applied radio frequency power.

Pulse sequence showed in Figure 5.1 is the one used for ^7Li nuclei, but in case of ^1H nuclei a different pulse sequence containing so called refocusing pulse is adopted according to the Hahn-Echo scheme shown in Figure 5.7. This particular pulse sequence is used for high-γ nuclei which have the highest sensitivity to external field variation. Such variations, related to inhomogeneities of the applied radio frequency field or dipolar coupling, make spins precess at different Larmor frequencies. This can cause an overall loss of coherence. Thanks to this this pulse sequence, this effect can be overcome.

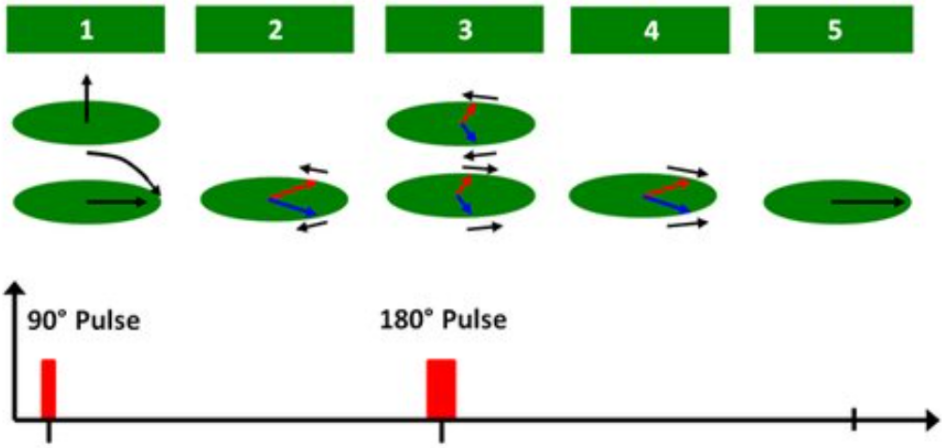

Figure 5.7: Hahn-echo pulse sequence

The calibration procedure is the same as in the previous case: 90° pulse length is progressively changed and nutation curve is recorded. The only difference with respect to the previous case is that once the transversal magnetization is built up after the first 90° pulse, inevitable spin coherence loss can lead to a reduction of the amplitude of transverse

magnetization. To overcome such problem, after the first 90° pulse, a time interval called rotor period, given by the reciprocal of the spinning frequency $1/\nu_{MAS}$, has to be waited to let the spin system spontaneously dephase. After one of rotor period, a 180° pulse acts on the system by rotating spins by a 180° angle in the transverse plane. The system evolves again for one rotor period until transverse magnetization builds up again along one of the axes in the transverse plane. Overall, according to this procedure, the system returns to the starting point where transverse magnetization in generated by the first 90° pulse .

As final remark, it is important to run pulse calibration measurements also to monitor the status of the probe, independently on the used pulse sequence. Indeed, when a specific nucleus is irradiated, a well define power is sent to a specific nucleus independently on the chemical compound. It is therefore expected to measure the same 90° pulse length. As an example consider ^7Li in different compounds irradiated with the same power. If the probe is correctly working, the expected t_{90} should be reasonably the same for each compound.

5.3. Saturation recovery

As discussed in the NMR theory section, T_1 is the time constant associated to the build-up of equilibrium magnetization. This parameter is crucial for NMR experiments since it sets so called recycle delay (or relaxation delay) as shown in Figure 5.1. This represents the time that we need to wait between the end of the acquisition of an FID and the immediately subsequent presaturation pulse.

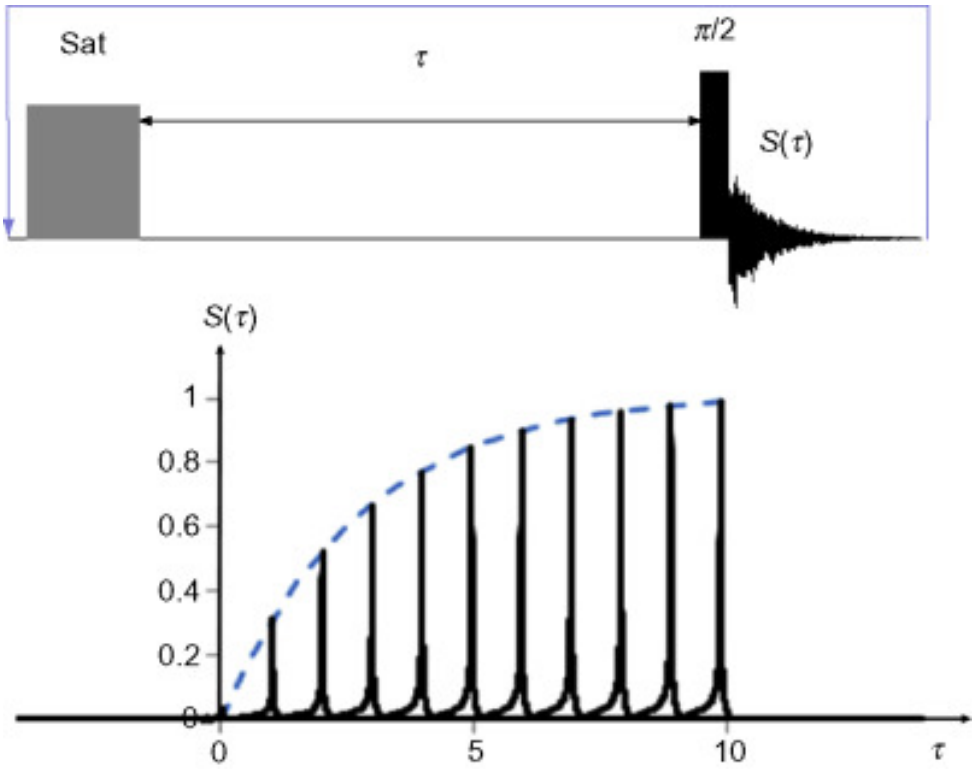

Figure 5.8: Saturation recovery pulse scheme (top) and magnetization build up over time(bottom)

The significance of T_1 lies in the fact that, between successive acquisitions, the equilibrium magnetization must properly rebuild and fully align along the z-axis, as defined by the static magnetic field of the spectrometer. To estimate T_1 for the nucleus of interest, saturation recovery experiments can be conducted. These involve acquiring multiple spectra with varying recycle delays between the presaturation pulse and the 90° pulse, following the pulse sequence scheme reported in Figure 5.8. The spectra are then integrated over a selected frequency range, for each set recycle delay. From the integral of the spectrum at different recycle delays, a multi-exponential fit is applied to analyze magnetization recovery over time:

$$M(t) = M_0(1 - \sum_i w_i e^{-\frac{t}{T_{1i}}})$$

where w_i is the weight of the i-th exponential component, associated to the estimated T_{1i}, used for the fit. The time constant with the highest weight of the fitting ultimately provides an estimate of the longitudinal relaxation time T_1. Once T_1 is determined, the recycle delay (RD) can be set, for the next experiments, to RD=$1.3\times T_1$ to maximize the signal-to-noise ratio per square root of time or to RD=$5\times T_1$ to obtain quantitative spectra. It is important to mention that in NMR spectroscopy, the signal-to-noise ratio

per square root of time serves as a key measure of sensitivity for a given chemical species.

5.4. Cross-polarization calibration

Cross-polarization requires irradiation on both probe channel and employs the pulse scheme shown in Figure 5.9

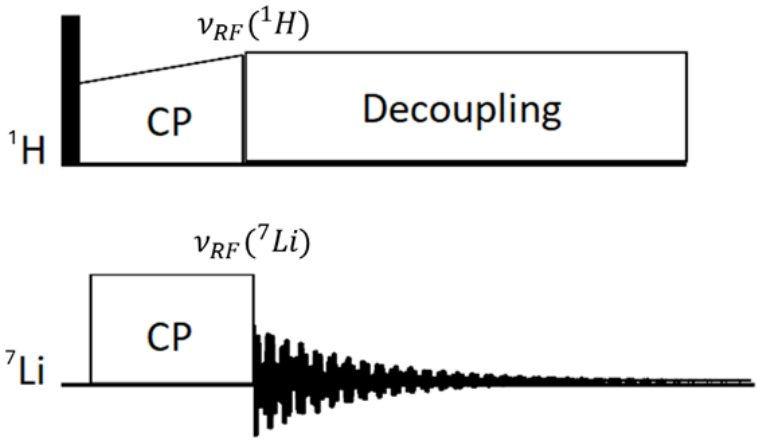

Figure 5.9: $^1H - ^7Li$ cross polarization pulse scheme using a ramped pulse on ^1H channel.

Calibration of cross-polarization can be done in two steps: contact pulse amplitude and contact pulse length calibration. During amplitude calibration step ^7Li channel is irradiated at constant well defined power $\nu_{RF}(^7Li)$ and ^1H channel is irradiated using a ramped pulse whose maximum is set by $\nu_{RF}(^1H)$. The ramp is used to compensate magnetic field inhomogeneities in the rotor and make each involved nucleus nutates at the same desired frequency. In practice, several experiments are ran keeping $\nu_{RF}(^7Li)$ fixed and linearly varying the maximum $\nu_{RF}(^1H)$ of the ramp. Once the contact pulse amplitude calibration is done, the so called *matching curve* is retrieved in which signals at maximum intensity should appear close to the Hartman-Hahn matching condition. The $\nu_{RF}(^1H)$ associated to maximum signal intensity is considered as the optimal power for cross-polarization detection. For all following experiments, reported power for CP calibration are the ones obtained by multiplying the measured optimal $\nu_{RF}(^1H)$ by 0.95. This is due to the use of a 90-100 ramp on the ^1H channel. In particular, at high spinning frequencies double quantum matching condition characterized by negative intensity can also appear as discussed in solid state NMR theory section.
As second optimization step, contact pulse duration is calibrated in order to maximize the acquired signal. To do this, spectra at different contact time are recorded and, as

previously done, contact time corresponding to maximum signal intensity is considered as optimal contact pulse length. In addition, when performing this second stage of experiments a gradual decay, with time constant $T_{1\rho}$, of the signal intensity is observed for longer pulse durations. This is due to the spontaneous dephasing of spin-locked nuclei.

5.5. Heteronuclear decoupling optimization

^1H heteronuclear decoupling is aimed at removing heteronuclear dipolar coupling between ^1H and ^7Li leading to a reduction of line broadening and an increase of signal intensity. As discussed in solid-state NMR theory section, ^1H heterounclear decoupling efficiency depends on spinning frequency. Precisely, when using high spinning frequency the optimal decoupling low $\nu_{RF}(^1H)$ on the ^1H channel is used. Such kind of decoupling approach can reduce overheating of the sample. When moving to static experiments continuous wave pulses can be used at high power.
Decoupling optimization is executed by acquiring spectra using double channel excitation. Specifically a pulse scheme identical to the one shown in figure 5.1 is applied on ^7Li channel, while continuous wave pulse is applied on ^1H channel simultaneously to the ^7Li acquisition stage.

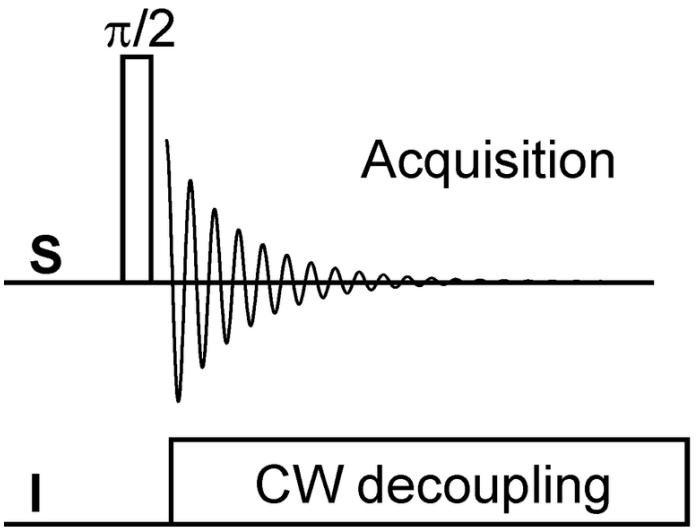

Figure 5.10: 1H CW decoupling pulse sequence. 7Li is considered ad S nucleus, 1H is assumed as I nucleus

Again, the optimal power to be applied is considered as the one associated to signal with maximum intensity. It is worth mentioning that the power that can be used could be even lower than the optimal one, providing that the signal intensity is comparable to the one

associated to the optimal decoupling power. This choice can be understood thinking that decoupling pulses have duration in the order order of ms and power of tens of kHz. Under these conditions, long time acquisition experiments can stress the probe and eventually damage the sample.

6 | Results and discussion

In this work calibration and optimization experiments are firstly executed on reference compound as Li hydroxide ($LiOH$), Li citrate ($Li_3C_6H_5O_7$), Li fluoride (LiF), Li carbonate (Li_2CO_3) and Li oxide (Li_2O). In particular Li hydroxide and Li citrate are used for CP and ^1H decoupling calibration due to the presence of $^1H -^7 Li$ proximity. Once the optimal experimental parameters are retrieved, acquisitions of spectra with reasonable high number of scans are ran both under magic angle spinning (MAS) and static conditions in order to obtain good sensitivity spectra. The choice of these reference compounds is related organic SEI composition. Indeed, as previously mentioned in the introduction section, SEI is composed by Li organic and inorganic salts. NMR spectra are acquired under MAS in order to retrieve information about chemical shifts and have a comparison with literature values [30]. Furthermore, static condition detection is conducted to assess the extent of spectral resolution loss in the absence of MAS.
In view of future operando NMR experiments for selective detection of organic SEI species under static condition, it will be important to firstly find a representative reference compound of Li organic salts. This compound will allow reliable $^1H -^7 Li$ CP calibration also for future experiments. As second target, it will be crucial to prove feasibility of CP under static conditions on ex-situ sample. Finally, given the small amount of expected SEI, the resulting signal intensity is anticipated to be low. To address this challenge, it will be essential to employ appropriate CP signal enhancement techniques, such as heteronuclear decoupling and low-temperature experiments. If selectivity is achieved on ex-situ samples, it will be possible to install an operando NMR probe and run experiments on working electrochemical cells.

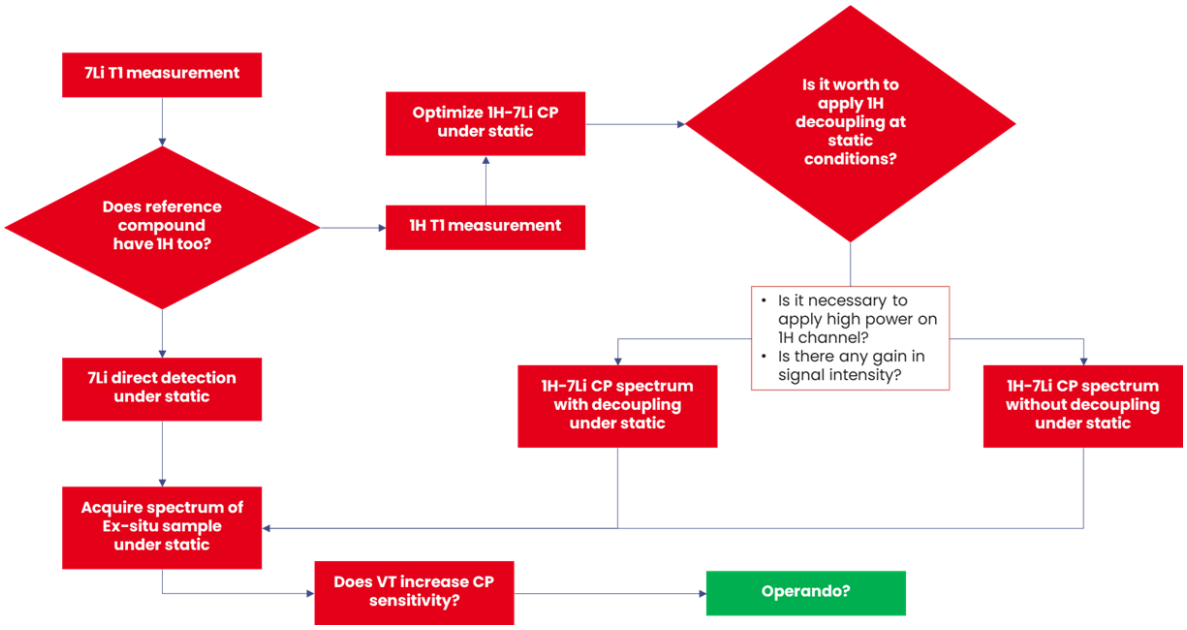

Figure 6.1: Flow chart of experiments

6.1. 90° pulse length calibration

Nutation curves were recorded for all of the reference compounds on both ^{1}H, ^{7}Li and ^{19}F nuclei under MAS at 40 kHz. Specifically 18 W were irradiated on ^{7}Li for each compound, while 15 W were used for ^{1}H in LiOH and 12 W Li citrate. Finally 12 W were used also for ^{19}F.

	$^{1}H[\mu s]$	$^{7}Li[\mu s]$	$^{19}F[\mu s]$
Li hydroxide	1.4 (0.1)	2.7 (0.1)	
Li citrate	1.4 (0.1)	2.1 (0.1)	
Li fluoride		2.3 (0.1)	1.4 (0.1)
Li carbonate		2.0 (0.1)	
Li oxide		2.0 (0.1)	

Table 6.1: 90° pulse calibration of reference compounds with reported error of 0.1 μs.

By looking at Table 6.1, for the same nucleus it is expected to measure same optimal 90° pulse length of 1.4 μs when irradiating ^{1}H with 15 W, 1.7 μs when irradiating with 12 W and 2.1 μs when using 18 W for ^{7}Li independently on the analyzed compound. Li hydroxide was the first reference compound to be calibrated and, as it is evident from the

measure 90° pulses, deviation from the expected calibration value indicates a non-optimal status of the experimental set-up. As consequence, due to non-linearity of the probe electronics, the expected irradiating power is not coincident to the real power irradiating the sample.

6.2. T_1 measurements

In order to set up recycle delays for later direct ^7Li excitation and $^1H -^7 Li$ CP experiments T_1 relaxation time constant were estimated using saturation recovery technique and subsequent multi-component exponential fitting.

Compound	$T_1(^1H)$[s] (w_i)	$T_1(^7Li)$[s] (w_i)	$T_1(^{19}F)$[s] (w_i)
Li Hydroxide	• 60 (0.80) • 0.68 (0.28)	• 470 (2.10) • 8 (0.12)	
Li Citrate	• 2 (0.94) • 0.1 (0.01)	• 77 (0.004) • 12 (5.63)	
Li Fluoride		• 266 (1.57) • 10 (0.003)	• 118 (1.01) • 40 (0.006) • 11 (0.004)
Li Carbonate		• 116 (0.93) • 13 (0.17) • 2 (0.002)	
Li Oxide		• 91 (1.50) • 14 (0.21) • 3 (0.004)	

Table 6.2: T_1 measurement of reference compound. Experiments werte ran under MAS. For each nucleus, are reported T_1 of each component and its associated weight w_i of the multi-component exponential fit for saturation recovery $M(t) = M_0(1 - \sum_i w_i e^{-\frac{t}{T1_i}})$. For each fit the RSS is in the order of 10^{-5}

.

For all next experiments, T_1 was chosen according to the estimated value associated to the highest weight w_i for the fit. Estimated T_1 in Table 6.2, are in the range of expected

Li diamagnetic salts [13]. Despite this, it is worth noticing the difference of T_1 in Li citrate and Li hydroxide. This discrepancy will strongly impact the sensitivity of next experiments. Indeed, this difference will result in shorter recycle delays for Li citrate compared to Li hydroxide. As a consequence, for the same experimental time, a higher number of scans is expected for the former compound. This, in turn, leads to an improved signal-to-noise ratio per square root of the total experimental time.

6.3. ^7Li direct acquisition under MAS and static conditions

Once T_1 relaxation time of each reference compound is known, ^7Li direct excitation measurement is performed with a recycle delay set to 1.3*$T_1(^7Li)$ in order to maximize signal sensitivity using the pulse sequence shown in Figure 5.1. The number of scans for each experiments is set to obtain high sensitivity spectra. To determine the number of scans, an initial acquisition was performed with 8 scans for each compound to assess the signal intensity after 8 scans, both under MAS and static conditions. Based on this preliminary evaluation, the final number of scans was then established.

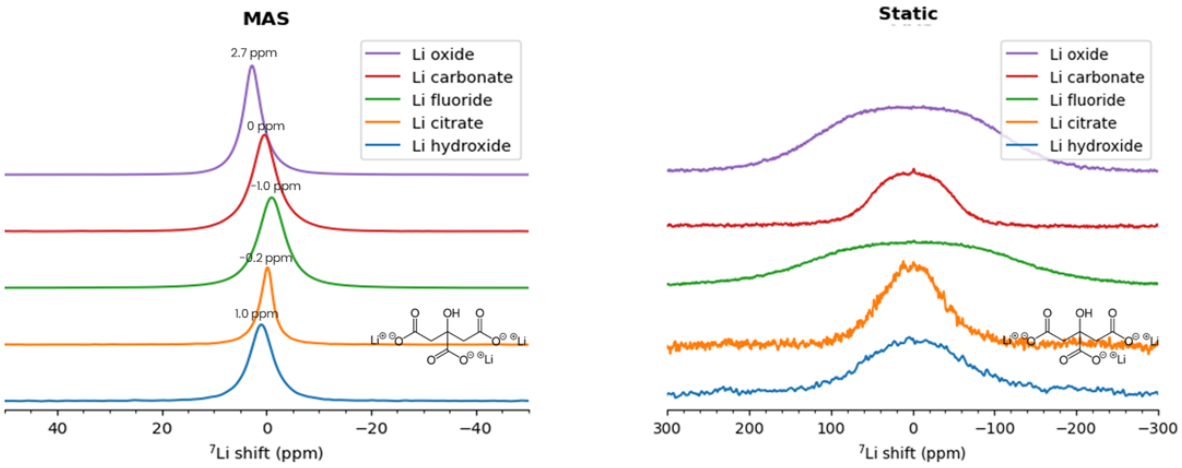

Figure 6.2: MAS (40 kHz) and static acquisition of reference compound with recycle delay set to 1.3*$T_1(^7Li)$.

Using chemical shift calibration with respect to ^7Li in LiF set to -1 pmm, we retrieved chemical shifts associated to each reference compound. Obtained results are in agreement in particular with the expected tabulated ones [30]. The fact that each of them is close to 0 ppm, along with the significant line broadening, makes it very challenging to differentiate between SEI species. This issue becomes even more pronounced when switching to static

acquisition, where a noticeable decrease in spectral resolution and reduced sensitivity are observed, as anisotropic interactions are not averaged out by MAS as shown in Figure 6.2 (left). As a result, a broad signal from the SEI is expected in static experiments of ex-situ samples, making it impossible to distinguish between the organic and inorganic salts of the SEI. This issue will be addressed through the use of CP.
It is worth to show comparison between ^{7}Li direct excitation of Li hydroxide and Li citrate MAS spectra.

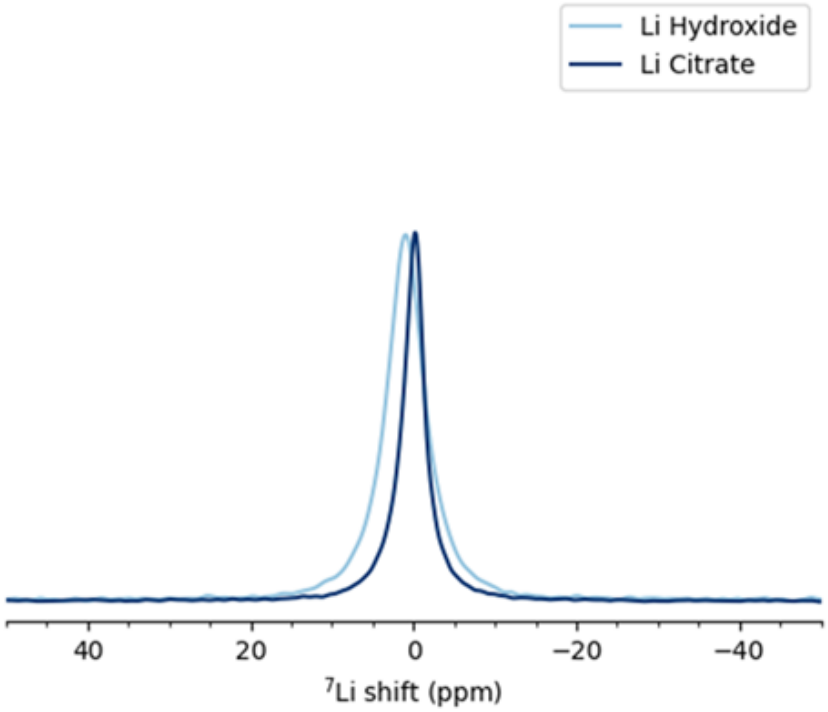

Figure 6.3: 7 Li direct detection comparison between Li hydroxide and Li citrate. 8 scans for Li citrate and 32 scans for Li hydroxide. Scaled per number of scans.

$\frac{SNR}{\sqrt{time}}(Li\ citrate) = 34.16$ and $\frac{SNR}{\sqrt{time}}(Li\ hydroxide) = 1.43$ show that sensitivity on Li citrate is higher due to the shorter $T_1(^{7}Li)$. As a consequence, a shorter experimental time is foreseen and because of this, faster calibration and optimization experiments can be performed.

6.4. $^{1}H - ^{7}Li$ CP calibration

Using CP pulse sequence shown in Figure 5.9 ^{7}Li magnetization builds up thanks to polarization transfer from ^{1}H nuclei. Such phenomenon occurs only in rigid chemical environments characterized by $^{1}H - ^{7}Li$ proximity as in the case of organic SEI species.

Once optimized, this methodology provides a powerful tool to selectively detect signal coming from the latter on ex-situ sample. Before doing so it is necessary to verify the feasibility of $^1H - ^7Li$ polarization transfer on reference compound in which both ^1H and ^7Li nuclei are present: Li hydroxide and Li citrate.

6.4.1. Li hydroxide CP calibration under MAS

a)

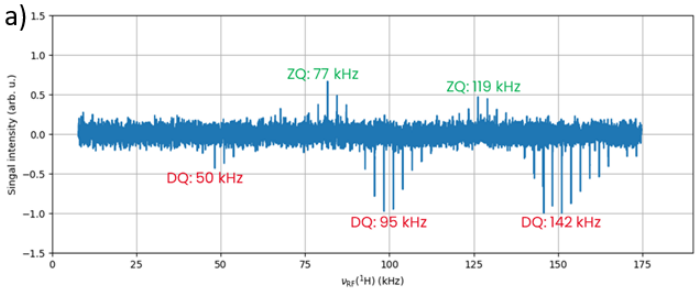

b)

n	ZQ[kHz]	DQ[kHz]
0	30	/
+1	70	10
+2	110	50
+3	150	90

Figure 6.4: a) CP matching curve in LiOH with reported experimental values of ^1H nutation frequencies associated to maximum intensities. 8 scan per experiment b) Table reporting expected zero-quantum and double-quantum matching condition frequencies. Experiments were ran under MAS (40 kHz). 8 scans per spectrum were acquired. Experimental time: 1 h 52 min.

^1H contact pulse amplitude optimization

$\nu_{RF}(^7Li)$ is set to 30 kHz while $\nu_{RF}(^1H)$ is spanned from 10 to 175 kHz using 90-100 ramp on ^1H channel. This ramp is used also to retrieve sharper matching condition in the matching curve. Due to the high spinning frequency, double quantum matching conditions with negative intensity appear as shown in Figure 6.4a. A discrepancy between the theoretically expected matching condition frequency is observed as reported in Figure 6.4b, caused by the non-ideality of the electronics on the ^1H channel, meaning that the frequency does not vary linearly between two consecutive spectra as expected. Additionally, due to the long $T_1(^1H)$ in LiOH, the equilibrium magnetization buildup takes a considerable amount of time, significantly extending the experimental duration. This also results in a smaller signal-to-noise ratio per square root of time. Finally, the decision to use 8 scans per spectrum was made to conduct this optimization experiment within a reasonable time frame.

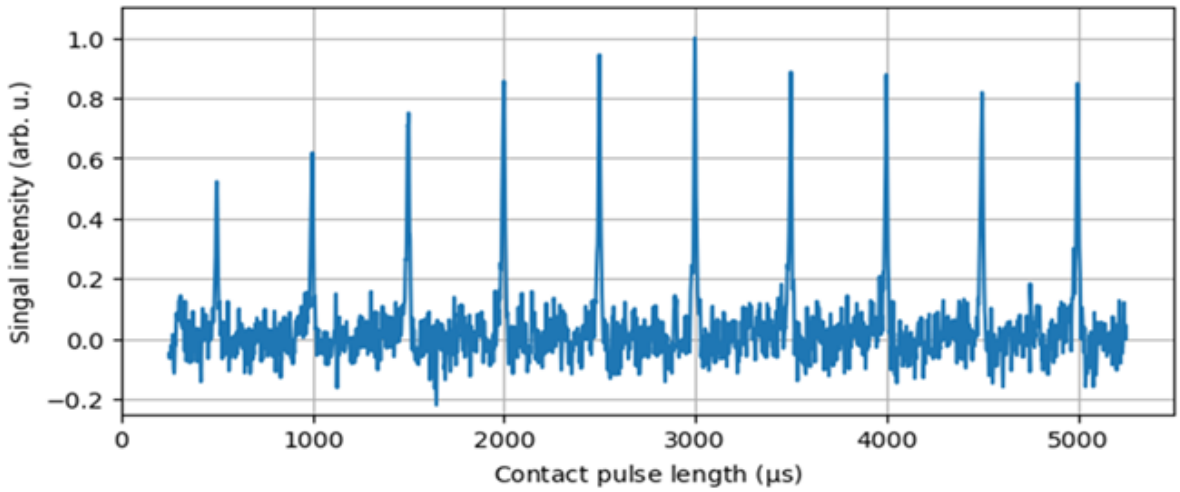

Figure 6.5: Contact pulse duration optimization at 142 kHz on ^{1}H channel and 30 kHz on ^{7}Li. Experiments were ran under MAS (40 kHz). 8 scans per spectrum were acquired. Experimental time: 17 min.

^{1}H contact pulse duration optimization

After contact pulse amplitude with a 90-100 ramp is ran, contact pulse duration calibration is performed using optimal ^{1}H contact pulse power of 142 kHz and linearly changing contact pulse duration from 0.5 ms to 5 ms under MAS. For LiOH, optimal contact pulse occur at 3 ms and looking at Figure 6.5, intensity decay for longer contact pulse appears. This is due to spontaneous dephasing during spin-lock.

6.4.2. Li hydroxide CP calibration under static

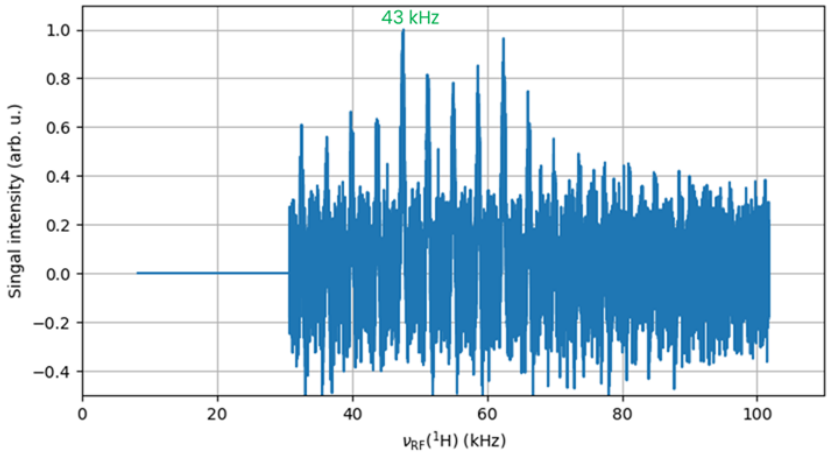

Figure 6.6: a) CP matching curve in LiOH with reported experimental values of ^1H nutation frequencies associated to maximum intensities. 8 scan per experiment b) Table reporting expected zero-quantum and double-quantum matching condition frequencies. Experiments were ran under static (0 kHz). 8 scans per spectrum were acquired. Experimental time: 1 h 52 min.

^1H contact pulse amplitude optimization

$\nu_{RF}(^7Li)$ is set to 30 kHz while $\nu_{RF}(^1H)$ is spanned from 10 to 100 kHz using 90-100 ramp on ^1H channel. Since MAS is not used, it is expected to observe one single zero quantum matching condition at $\nu_{^1H} = \nu_{^7Li}$. Again, due to non linearity of ^1H amplifier, a significant mismatch from the expected theoretical value is observed as shown in Figure 6.6.

Following these preliminary experiments, we concluded that the long experimental time required for CP calibration made the use of Li hydroxide unfeasible. As a result, an alternative reference compound for $^1H^7Li$ CP calibration was selected: Li citrate.

6.4.3. Li citrate CP calibration under MAS

The calibration of ^1H and ^7Li 90° pulses, T_1 measurements, and ^7Li direct excitation on Li citrate were conducted sequentially, following the CP calibration of Li hydroxide and prior to the CP calibration on Li citrate. After completing these preliminary experiments, the ^1H amplifier was replaced, and a probe cortab was performed to restore the linearity of electronics in the experimental apparatus. Following these adjustments, new

90° pulse calibrations for both ^1H and ^7Li were conducted, and the ^7Li direct excitation spectrum was re-recorded. A comparison of the ^7Li spectra before and after the cortab and amplifier replacement revealed a decrease in signal intensity. This issue was resolved by disconnecting the ^1H filter between the probe and the amplifier. From that point onward, all experiments were conducted without the ^1H filter connected.

a)

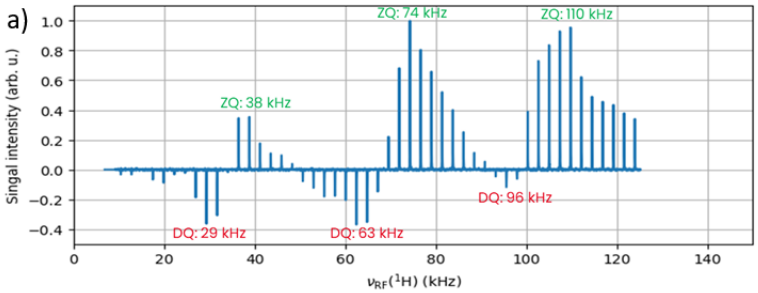

b)

n	ZQ[kHz]	DQ[kHz]
0	36	/
+1	76	4
+2	116	44
+3	156	84

Figure 6.7: a) CP matching curve in Li citrate with reported experimental values of ^1H nutation frequencies associated to maximum intensities. 8 scan per experiment b) Table reporting expected zero-quantum and double-quantum matching condition frequencies. Experiments were ran under MAS (40 kHz). Experimental time: 17 min.

^1H contact pulse amplitude optimization

$\nu_{RF}(^7Li)$ is set to 36 kHz while $\nu_{RF}(^1H)$ is spanned from 10 to 120 kHz using 90-100 ramp on ^1H channel. Since experiments were ran under MAS at 40 kHz double quantum matching conditions are expected with negative intensity.

It is clear that once linearity was restored, discrepancy between experimental matching condition and theoretical expected ones is drastically reduced comparing Figures 6.7a-b. Furthermore, matching curve quality for Li citrate is clearer than the one of Li hydroxide due to shorter $T_1(^1H)$. Shorter $T_1(^1H)$ implies the amount of time needed to record the matching curve to be inevitably smaller, making CP calibration under MAS recordable in a much reasonable time.

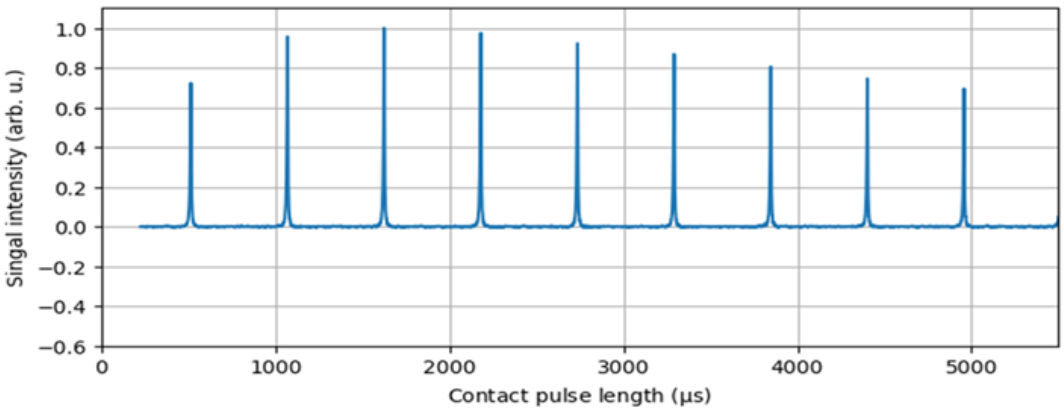

Figure 6.8: Contact pulse duration of Li citrate optimization at 74 kHz on ^1H channel and 36 kHz on ^7Li. Experiments were ran under MAS (40 kHz). 8 scans per spectrum were acquired. Experimental time: 3 min.

^1H contact pulse duration optimization

Using optimal ^1H contact pulse power of 74 kHz and linearly changing contact pulse duration from 0.5 ms to 5 ms under MAS, contact pulse calibration curve was recorded. Optimal contact pulse duration is reached at about 1.5 ms as reported in Figure 6.8. This calibration curve also shows a faster spin-lock dephasing attributable to the shorter T_1 of both ^7Li and ^1H. It is worth noticing that, under MAS, optimal contact pulse duration is shorter than in the case of Li hydroxide (3 ms). This can be understood assuming a stronger $^1H-^7Li$ dipolar coupling in Li citrate, leading to a faster polarization transfer.

6.4.4. Li citrate CP calibration under static

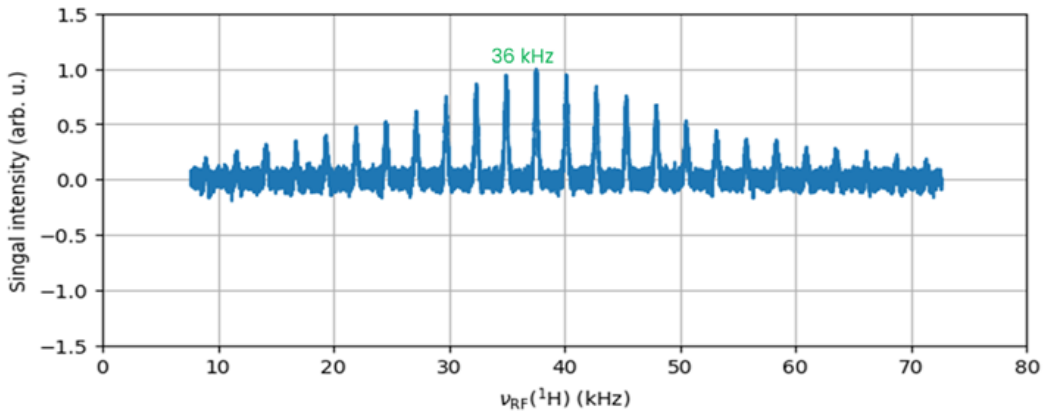

Figure 6.9: a) CP matching curve in Li Citrate with reported experimental values of ^1H nutation frequencies associated to maximum intensities. 8 scan per experiment.Experiments were performed under static (0 kHz). 8 scans per spectrum were acquired. Experimental time: 34 min.

^1H contact pulse amplitude optimization

$\nu_{RF}(^7Li)$ is set to 36 kHz while $\nu_{RF}(^1H)$ is spanned from 10 to 70 kHz using 90-100 ramp on ^1H channel. For static experiments one single zero quantum matching condition is expected at $\nu_{RF}(^7Li) = \nu_{RF}(^1H)$. The recorded matching curve in Figure 6.9 shows an optimal $\nu_{RF}(^1H)$ for contact pulse of 36 kHz, exactly coincident to the one applied on ^7Li.

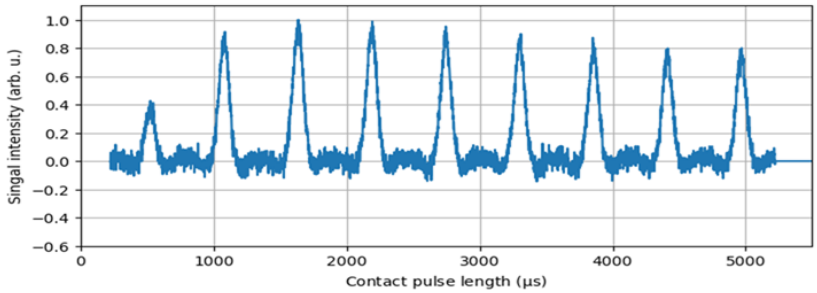

Figure 6.10: Contact pulse duration of Li citrate optimization at 36 kHz on ^1H channel and 36 kHz on ^7Li. Experiments were ran under static (0 kHz). 8 scans per spectrum were acquired. Experimental time: 7 min.

^1H contact pulse duration optimization

For completeness, also contact pulse duration with the optimal experimental measured powers was finally performed. Contact pulse duration was varied from 0.5 ms to 5 ms. Also in the case of static experiments, optimal contact pulse duration of Li citrate remains fixed at 1.5 ms as reported in Figure 6.10.

These results demonstrate that $^1H - ^7Li$ CP is indeed achievable under static conditions. This makes it possible to perform CP experiments on ex-situ samples using optimized experimental parameters. Furthermore, the shorter experimental time and improved sensitivity observed with Li citrate suggest that this compound represents a more suitable candidate than Li hydroxide for future $^1H - ^7Li$ CP calibrations.

Beside this, it is important to observe that, on reference samples, the use of CP gives rise to a worsening in sensitivity as can be noticed from comparisons between reference compounds direct detection and CP, under both MAS and static conditions as illustrated in Figure 6.11. This is in contradiction to expected theoretical $\frac{\gamma_{1H}}{\gamma_{7Li}}$ signal enhancement of CP experiments.

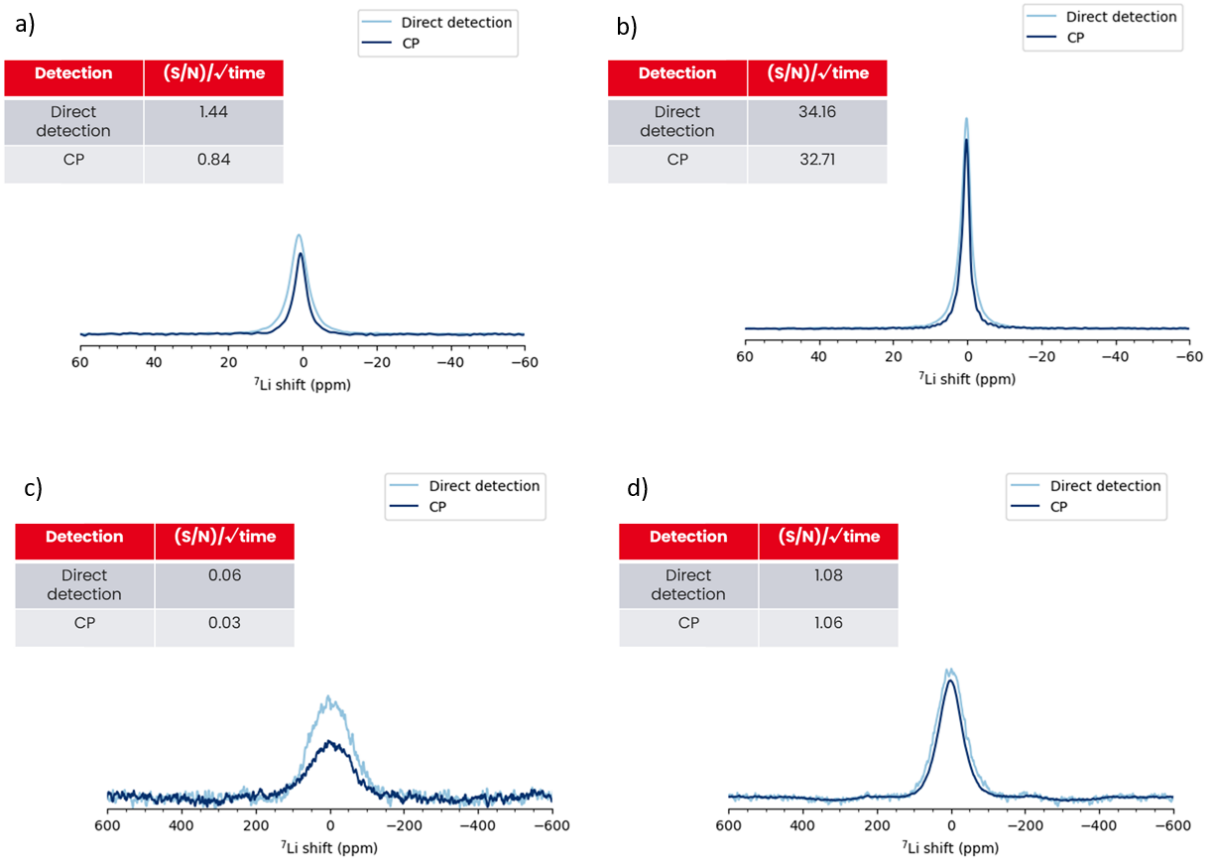

Figure 6.11: a) Li hydroxide comparison between CP and direct detection under MAS (40 kHz) b) Li citrate comparison between CP and direct detection under MAS (40 kHz) c) Li hydroxide comparison between CP and direct detection under static (0 kHz) d) Li citrate comparison between CP and direct detection under static (0 kHz). For all comparison are reported SNR per square root of time as measure of sensitivity. Scaled per number of scans.

As can be observed, for all comparisons CP leads to a worsening of SNR per square root of time. Reasons behind this result could be several. First, in the case of CP-MAS experiments, the use of 40 kHz as spinning frequency might not be the optimal one. The choice of this spinning frequency is justified by the fact that a 1.3 mm rotor remains stable at this frequency. Second, for $^{1}H-^{7}Li$ CP experiments the expected signal enhancement is $\frac{\gamma_{1H}}{\gamma_{7Li}} = 2.6$ in turn lower than common used CP nuclei $^{1}H-^{13}C$. For the latter case we expect an enhancement factor $\frac{\gamma_{1H}}{\gamma_{13C}} = 4$. Finally, it should be noted that ^{7}Li is a quadrupolar nucleus with a $3/2$ nuclear spin. This creates challenges during spin-lock pulses, reducing the efficiency of polarization transfer and making CP pulse scheme shown in Figure 5.9 less effective for such nuclei. However, conventional CP was still used due

to the relatively small quadrupolar coupling constant of ^{7}Li, which makes it behave more like a spin-1/2 nucleus.

6.5. ^{1}H heteronuclear decoupling optimization under static

As previously discussed, CP measurements lead to a decrease in signal sensitivity, making it essential to find a method to mitigate this issue. ^{1}H decoupling was investigated under static conditions with the aim of implementing it in operando experiments. This investigation was carried out on the Li citrate reference compound, where spectra were initially recorded with and without ^{1}H decoupling using continuous wave on the ^{1}H channel during acquisition, followed by optimization.

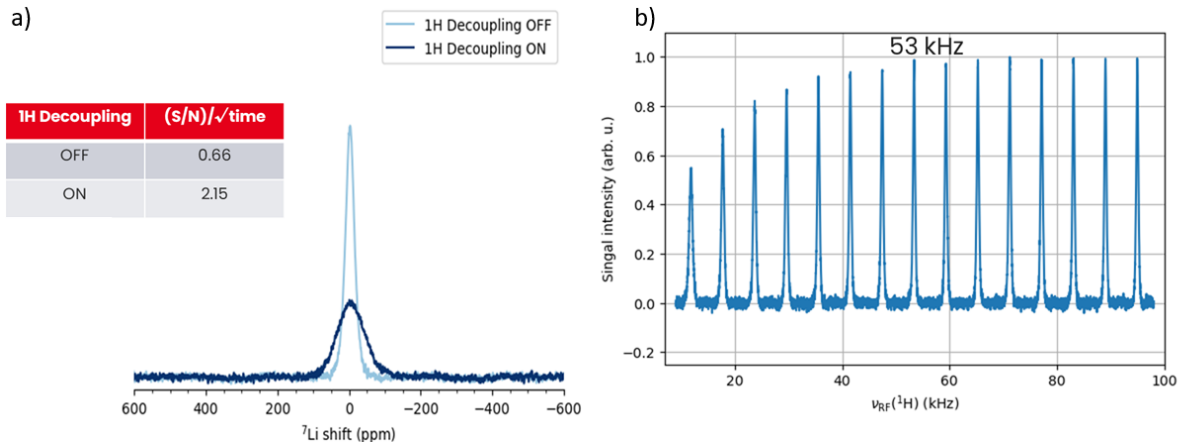

Figure 6.12: a) Comparison between ^{7}Li direct detection with (100 kHz on ^{1}H) and without decoupling. SNR per square root of time for both experiments are reported b) ^{1}H decoupling power optimization. Experimental time: 10 min 30 sec.

Final conclusion from these experiment on Li citrate reference sample is that ^{1}H decoupling can be in principle useful to retrieve lost sensitivity due to CP inefficiency. More important, as a overall result from experiments on reference samples, CP under static condition has been verified to selectively detect ^{7}Li signal in close proximity to ^{1}H. As further step, ex-situ sample experiments were ran.

Observing Figure 6.11a it appears evident that the application of ^{1}H decoupling improves signal sensitivity due to the removal of heteronuclear dipolar coupling between ^{1}H and ^{7}Li. Once this first result was obtained, decoupling optimization was ran at different

$\nu_{RF}(^1H)$ from 0 to 100 kHz. The reported $\nu_{RF}(^1H)$ in figure 6.11 b represents the optimal decoupling power. This choice is understandable, considering that in operando NMR experiments a functioning battery will cycle for an extended period, and NMR experiments need to be carried out simultaneously. This means that the probe will endure significant stress if high power is used. Reducing the power (even below 53 kHz) while still retaining the sensitivity benefits of decoupling will be advantageous for the experimental setup.

6.6. Ex-situ sample experiments

As preliminary analysis of ex-situ samples 90°calibration for ^7Li was verified with MAS (40 kHz) experiment and secondly T_1 relaxation time were conducted on both ^7Li and ^1H using saturation recovery experiments.

$T_1(^1H)$[s] (w_i)	$T_1(^7Li)$[s] (w_i)
• 0.42 (0.72) • 0.02 (0.25)	• 0.33 (0.56) • 0.02 (0.42)

Table 6.3: T_1 measurement of ex-situ sample compound. Experiments were ran under MAS (40 kHz). For each nucleus, are reported T_1 of each component and its associated weight w_i of the multi-component exponential fit for saturation recovery $M(t) = M_0(1 - \sum_i w_i e^{-\frac{t}{T1_i}})$. For each fit the RSS is in the order of 10^{-5}

.

As observed from the Table 6.3 a net decrease of T_1 relaxation time for both nuclei can be noticed and ascribable to high chemical heterogeneity that is more likely to lead to local magnetic field fluctuations

After this first measurements, quantitative spectra with recycle delay set to $5*T_1(^7Li)$ were performed for ^7Li direct excitations while recycle delay set to 1s was used for CP experiments.

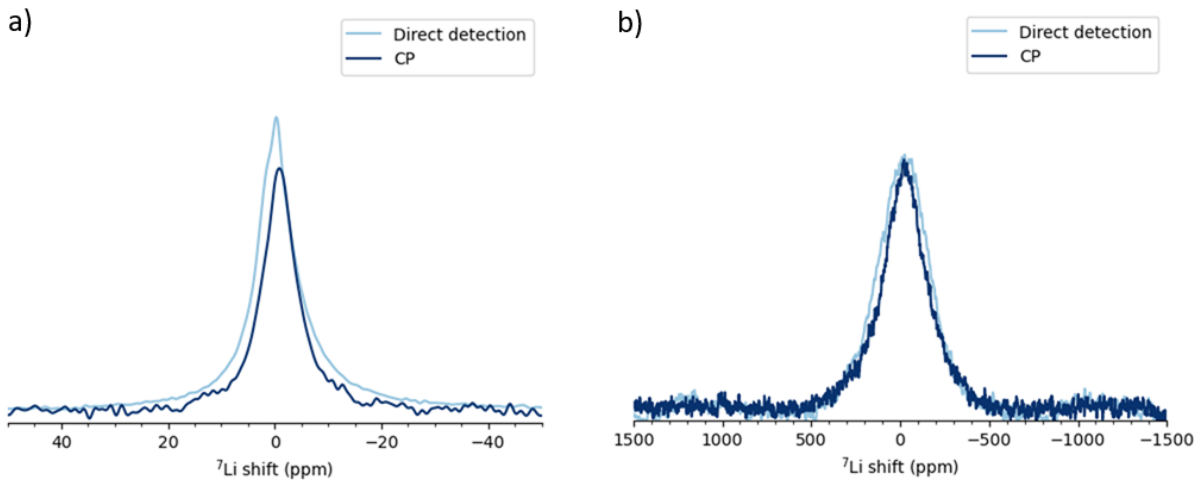

Figure 6.13: a) Comparison between ^7Li direct quantitative excitation and CP under MAS (40 kHz). Experimental time: 2 min (direct ^7Li detection), 16 h 5 min (CP) b)Comparison between ^7Li direct quantitative detection and CP under static (0 kHz). Experimental time: 1 h 6 min (direct ^7Li detection), 21 h 8 min (CP)

In ^7Li direct excitation, nuclei belonging to both organic and inorganic species of the SEI are detected (lithium silicide crystalline phases are not observed since a delithiated sample is used). By using CP, calibrated with the experimental contact pulse parameters obtained from the Li citrate optimization, only the signal from the organic SEI is observed at negative ppm. Selectivity is confirmed by the fact that CP peak is not sufficient to recreate the exact lineshape detected with ^7Li direct excitation as shown in Figures 6.13a-b. The remaining contributions to the signal come from inorganic SEI salts (e.g LiF ,Li_2O, Li_2CO_3, $LiOH$).

As final remark, it can be noticed the presence of an asymmetry at the left base of the peak which might be explained by the occurrence of CP also for Li hydroxide. Comparison illustrated in Figure 6.13 a) shows that once ^1H decoupling is applied, a small increase of signal in the negative ppm side of the spectrum is observed thus verifying the idea that organic SEI is characterized by a chemical shift in the negative range of the spectrum. As final result, Figure 6.13 b) shows that application of ^1H decoupling produces a small gain in intensity. Despite this, observed ^1H decoupling effect is not as significant as in the case of Li citrate.

The assumption that the organic SEI is characterized by a negative ppm chemical shift is further supported by experiments in which ^1H heteronuclear decoupling effects were compared using $\nu_{RF}(^1H)$ calibrated from previous experiments as reported in Figures 6.14a-b.

To interpret these results, it is important to consider that in Li citrate, the ^{7}Li nuclei are surrounded by a homogeneous and symmetrical environment, which leads to an electric field gradient close to zero, effectively canceling out quadrupolar coupling and associated anisotropic line broadening. Furthermore, since the Li citrate reference sample consists of a single compound, chemical shift anisotropy effects are expected to be minimal. In conclusion, the primary source of line broadening in Li citrate is heteronuclear dipolar coupling. By applying ^{1}H decoupling, the $^{1}H-^{7}Li$ dipolar interaction is removed, resulting in line narrowing and improved sensitivity. When moving to actual ex-situ samples, the increased electric field inhomogeneity and chemical heterogeneity make quadrupolar and CSA line broadening effects more pronounced compared to a pure, homogeneous sample. As a result, due to the reduced contribution of line broadening from heteronuclear coupling, ^{1}H decoupling does not lead to a significant improvement in sensitivity.
After these initial experiments, we concluded that selective detection of organic SEI species was achieved, despite the high noise levels caused by the small amount of material detected. The final step in the experiments was to find a more effective way to enhance the organic SEI signal. To accomplish this, experiments at lower temperatures were conducted using an NMR probe chiller.

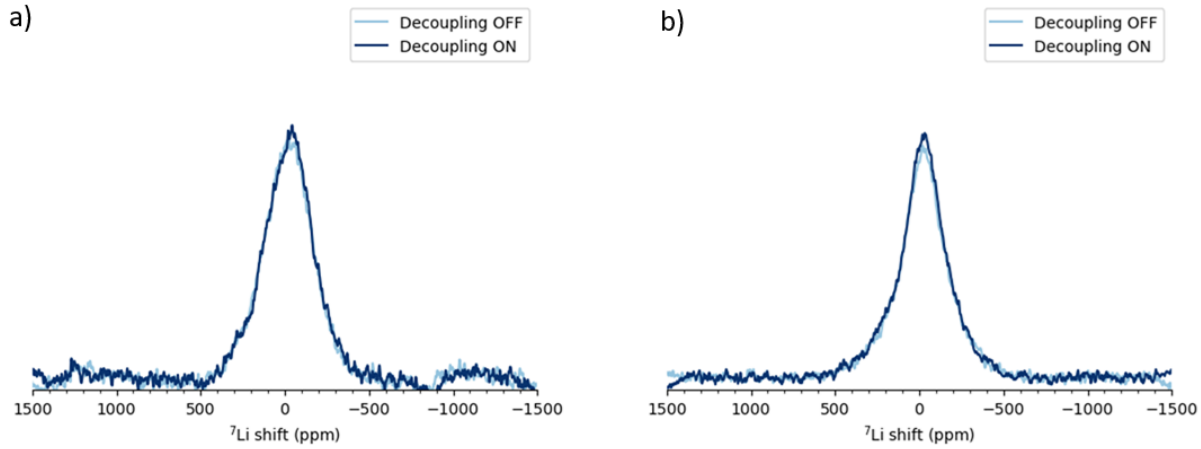

Figure 6.14: a) Comparison between ^{7}Li direct quantitative detection with and without optimized ^{1}H decoupling under static (0 kHz) b)Comparison between CP with and without decoupling under static (0 kHz). Scaled per number of scans.

6.7. Ex-situ sample experiment with variable temperature

6.7.1. ^{7}Li Direct detection

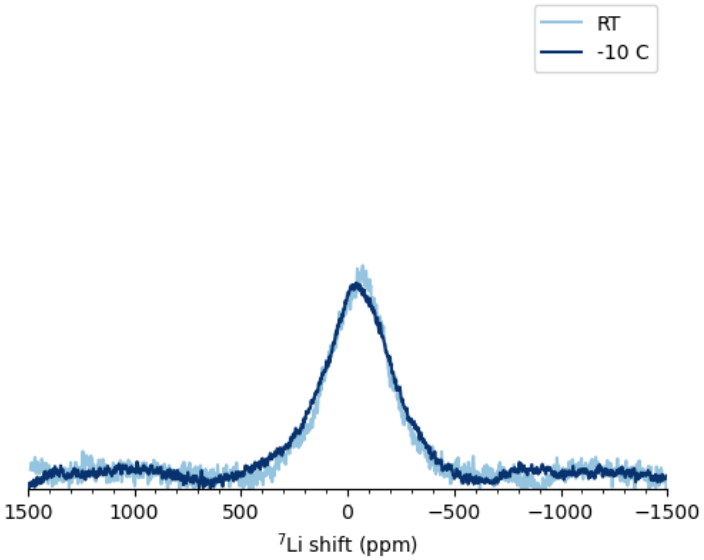

Figure 6.15: Comparison between ^{7}Li direct detection at room temperature (light blue) and -10°C (dark blue) scaled per number of scans.

By looking at the reported comparison in Figure 6.15 between ^{7}Li direct detection at room temperature and at -10°C with optimal ^{1}H decoupling, two main effects are evident. As a overall, by lowering temperature the net line broadening has increased due to reduction of molecular motion leading to a strengthening of heteronuclear dipolar coupling between ^{1}H and ^{7}Li. This suggestion is further supported by examining the baseline corrections at the edges of the spectra. At room temperature, since no signal is detected in this region, the baseline corrections do not distort the spectrum. However, at -10°C, the baseline corrections significantly distort the spectrum, indicating that a signal is detected even at higher frequencies. Additionally, it can be observed that at low temperature, ^{1}H decoupling does not produce the same effect as observed in the room temperature measurements, as shown in Figure 6.13a, where an intensity enhancement is seen in the organic SEI region. This discrepancy may be due to the fact that power levels in the probe are temperature-dependent, and optimizing ^{1}H decoupling at -10°C could have helped recover the expected increase in SEI signal.

6.7.2. $^{1}H - ^{7}Li$ CP

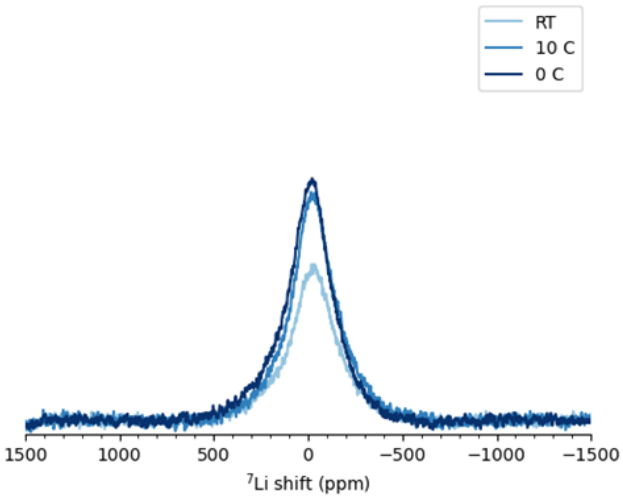

Temperature [°C]	(S/N)/√time
20	0.104
10	0.157
0	0.160

Figure 6.16: Comparison between $^{1}H - ^{7}Li$ CP detection at room temperature (light blue), 10°C (blue) and 0°C (blue) scaled per number of scans. Here reported also SNR per square root of time. Experimental time: 17 h 35 min (RT), 15 h 38 min (10°C), 19 h 11 min (0°C).

CP experiments comparison in Figure 6.16, using both $\nu_{RF}(^{7}Li)$ and $\nu_{RF}(^{1}H)$ set to 36 kHz, show a gain in sensitivity when low temperature is used. This confirms the idea that lower temperature helps reducing residual mobility boosting dipolar coupling between ^{1}H and ^{7}Li. It is worth noting in conclusion that the sensitivity improvement between experiments conducted at 10°C and 0°C is not significant, indicating that the effects observed at both temperature regimes are nearly identical. This last result represents an important breakthrough for future CP operando NMR experiments. Electrochemical cycling stability at 10°C is maintained [8], allowing operando measurements without compromising battery kinetics and performance. Ideally, experiments at even lower temperatures could be conducted, but to avoid cycling issues, in-situ experiments should be performed where the cell is first cycled, then stopped, measured at low temperature, and cycled again at room temperature. It is easy to see that such an approach would be impractical from an experimental standpoint.

7 | Conclusions and future developments

$^1H-^7Li$ cross-polarization calibration under static conditions on reference samples showed that polarization transfer between these nuclei can occur. Transferring the optimized $^1H-^7Li$ cross-polarization powers on reference samples to ex-situ sample, revealed the feasibility of selective organic SEI detection under static condition. As a consquence, it is firstly possible to conclude that selective detection of organic SEI species exploiting $^1H-^7Li$ CP under static condition can work on a standard double-channel probe. As additional consideration, it is worth mentioning that in this work SEI signal enhancement methodologies have been also investigated for the first time on a standard double channel probe.

^1H heteronuclear decoupling

^1H decoupling using a CW (continuous wave) pulse at room temperature was attempted, showing on reference Li citrate reference compound a tripled gain in sensitivity under static conditions. Transferring the optimal ^1H decoupling power to the ex-situ sample, such enhancement was not been observed due to the higher chemical heterogeneity and complexity of interactions involved. A solution aimed at recovering higher sensitivity could be for example the implementation of different pulse sequences for ^1H heteronuclear decoupling instead of using a simple continuous wave pulse on ^1H channel. It has to be noticed that for operando experiments, experimental time are expected to be inevitably longer due to the presence of electrochemical cycling. Therefore ^1H heteronuclear decoupling power will have to be properly set to avoid stress on the probe and overheating of the sample.

Variable temperature

Cross-polarization experiments at low temperature represent a solution for signal enhancement without resulting detrimental for the probe, or the sample. By moving from room temperature experiments to 10°C, an improvement of 33 % was observed. This represents a very promising result for future operando experiments since at such temperatures, electrochemical cycling is not expected to be compromised.

Future operando experiments

From the results obtained with ex-situ experiments, and verified feasibility of polarization transfer for selective detection of organic SEI under static condition, operando measurement can be ran.

The first step is to optimize the assembly of the capsule operando cell, as the prototype of the full NMC-Si operando cell has shown unusual electrochemical cycling. Once the proper assembly protocol is defined, well-established ^{7}Li operando direct detection of Si half-cells can be performed to monitor the evolution of the ^{7}Li spectrum during lithiation and delithiation. Under these conditions, SEI selectivity will not be achieved, and consequently, the only expected signals will come from the crystalline phases of Li silicides and electrolyte. Before conducting CP experiments under operando conditions, $^{1}H - ^{7}Li$ CP calibration has to be performed on Li citrate to test CP feasibility on the opeando NMR probe. The challenges with this particular probe will stem from strong magnetic field inhomogeneities present in the operando cell sample. These inhomogeneities are inevitable when large samples, such as operando cells, are involved. Therefore, robust pulse sequences that can handle these inhomogeneities will be needed to be applied. After calibrating the experimental parameters for $^{1}H - ^{7}Li$ CP on Li citrate, SEI species in aged electrodes can be detected without cycling, to verify the viability of CP under operando NMR conditions. Once the calibration is complete, operando NMR experiments can be run under electrochemical cycling conditions to monitor organic and inorganic SEI formation. The results from these experiments will not only represent a significant breakthrough in the field of solid-state NMR operando spectroscopy but will also enable specific, non-invasive monitoring of SEI formation under operando conditions, an area that remains unexplored in the current state of the art. This will pave the way for comparative studies across different battery chemistries, enabling the tailored design of electrodes, electrolytes and additives to guarantee high-performance levels for various applications.

Bibliography

[1] L. Beaulieu, D. Larcher, R. Dunlap, and J. Dahn. Reaction of li with grain-boundary atoms in nanostructured compounds. *Journal of the Electrochemical Society*, 147(9): 3206, 2000.

[2] P. G. Bruce. Energy storage beyond the horizon: Rechargeable lithium batteries. *Solid State Ionics*, 179(21-26):752–760, 2008.

[3] K. K. Chandrasiri, C. C. Nguyen, B. S. Parimalam, S. Jurng, and B. L. Lucht. Citric acid based pre-sei for improvement of silicon electrodes in lithium ion batteries. *Journal of The Electrochemical Society*, 165(10):A1991, 2018.

[4] N. Chawla, N. Bharti, and S. Singh. Recent advances in non-flammable electrolytes for safer lithium-ion batteries. *Batteries*, 5(1):19, 2019.

[5] M. Duer. *Solid State NMR Spectroscopy*. Royal Society of Chemistry, Cambridge, UK, 1st edition, 2008.

[6] V. Etacheri, R. Marom, R. Elazari, G. Salitra, and D. Aurbach. Challenges in the development of advanced li-ion batteries: a review. *Energy & environmental science*, 4(9):3243–3262, 2011.

[7] M. Gao, H. Li, L. Xu, Q. Xue, X. Wang, Y. Bai, and C. Wu. Lithium metal batteries for high energy density: Fundamental electrochemistry and challenges. *Journal of Energy Chemistry*, 59:666–687, 2021.

[8] Z. Gao, H. Xie, X. Yang, W. Niu, S. Li, and S. Chen. The dilemma of c-rate and cycle life for lithium-ion batteries under low temperature fast charging. *Batteries*, 8 (11):234, 2022.

[9] J. B. Goodenough. Evolution of strategies for modern rechargeable batteries. *Accounts of chemical research*, 46(5):1053–1061, 2013.

[10] J. Graetz, C. Ahn, R. Yazami, and B. Fultz. Highly reversible lithium storage in nanostructured silicon. *Electrochemical and Solid-State Letters*, 6(9):A194, 2003.

[11] J. Graetz, C. Ahn, R. Yazami, and B. Fultz. Nanocrystalline and thin film germanium electrodes with high lithium capacity and high rate capabilities. *Journal of The Electrochemical Society*, 151(5):A698, 2004.

[12] D. Iaboni. *Li15Si4 Formation in Thin Film Si Negative Electrodes for Li-ion Batteries*. PhD thesis, 2015.

[13] A. J. Jacobson and M. S. Conradi. *Lithium NMR: From Basic Principles to Applications*. Magn Reson Chem, 2013.

[14] G. J. Kearley and V. K. Peterson. *Neutron applications in materials for energy*. Springer, 2015.

[15] B. Key, R. Bhattacharyya, M. Morcrette, V. Seznec, J.-M. Tarascon, and C. P. Grey. Real-time nmr investigations of structural changes in silicon electrodes for lithium-ion batteries. *Journal of the American Chemical Society*, 131(26):9239–9249, 2009.

[16] B. Key, M. Morcrette, J.-M. Tarascon, and C. P. Grey. Pair distribution function analysis and solid state nmr studies of silicon electrodes for lithium ion batteries: understanding the (de) lithiation mechanisms. *Journal of the American Chemical Society*, 133(3):503–512, 2011.

[17] J. Kim, J. G. Lee, H.-s. Kim, T. J. Lee, H. Park, J. H. Ryu, and S. M. Oh. Thermal degradation of solid electrolyte interphase (sei) layers by phosphorus pentafluoride (pf5) attack. *Journal of The Electrochemical Society*, 164(12):A2418, 2017.

[18] J. Kim, O. B. Chae, and B. L. Lucht. Perspective—structure and stability of the solid electrolyte interphase on silicon anodes of lithium-ion batteries. *Journal of The Electrochemical Society*, 168(3):030521, 2021.

[19] S. A. Krachkovskiy, M. Reza, A. R. Aguilera, I. C. Halalay, B. J. Balcom, and G. R. Goward. Real-time quantitative detection of lithium plating by in situ nmr using a parallel-plate resonator. *Journal of The Electrochemical Society*, 167(13):130514, 2020.

[20] S. A. Krachkovskiy, M. Reza, A. R. Aguilera, I. C. Halalay, B. J. Balcom, and G. R. Goward. Real-time quantitative detection of lithium plating by in situ nmr using a parallel-plate resonator. *Journal of The Electrochemical Society*, 167(13):130514, 2020.

[21] S. Laage, J. R. Sachleben, S. Steuernagel, R. Pierattelli, G. Pintacuda, and L. Emsley. Fast acquisition of multi-dimensional spectra in solid-state nmr enabled by ultra-fast mas. *Journal of Magnetic Resonance*, 196(2):133–141, 2009.

[22] D. Larcher and J.-M. Tarascon. Towards greener and more sustainable batteries for electrical energy storage. *Nature chemistry*, 7(1):19–29, 2015.

[23] B.-S. Lee. A review of recent advancements in electrospun anode materials to improve rechargeable lithium battery performance. *Polymers*, 12(9):2035, 2020.

[24] J. G. Lee, J. Kim, J. B. Lee, H. Park, H.-S. Kim, J. H. Ryu, D. S. Jung, E. K. Kim, and S. M. Oh. Mechanical damage of surface films and failure of nano-sized silicon electrodes in lithium ion batteries. *Journal of The Electrochemical Society*, 164(1): A6103, 2016.

[25] H. Li, X. Huang, L. Chen, Z. Wu, and Y. Liang. A high capacity nano si composite anode material for lithium rechargeable batteries. *Electrochemical and solid-state letters*, 2(11):547, 1999.

[26] J. Li, R. Lewis, and J. Dahn. Sodium carboxymethyl cellulose: a potential binder for si negative electrodes for li-ion batteries. *Electrochemical and Solid-State Letters*, 10(2):A17, 2006.

[27] J. Li, R. Lewis, and J. Dahn. Sodium carboxymethyl cellulose: a potential binder for si negative electrodes for li-ion batteries. *Electrochemical and Solid-State Letters*, 10(2):A17, 2006.

[28] J. Li, N. J. Dudney, J. Nanda, and C. Liang. Artificial solid electrolyte interphase to address the electrochemical degradation of silicon electrodes. *ACS applied materials & interfaces*, 6(13):10083–10088, 2014.

[29] A. Louis-Joseph et al. Comptes rendu chimie. 22(9-10), 20219.

[30] D. R. MacNeil, A. F. K. P. Liu, and A. S. Gordon. Nuclear magnetic resonance studies of the solid electrolyte interphase in lithium-ion batteries. *J. Phys. Chem. C*, 127(21):A1824–A1832, 2023.

[31] F. Markets. Global lithium ion battery market is expected to reach usd 107.6 billion by 2025: Fior markets, 2019. URL `http://www.fiormarkets.com/`. Accessed October 21, 2019.

[32] E. Markevich, K. Fridman, R. Sharabi, R. Elazari, G. Salitra, H. Gottlieb, G. Gershinsky, A. Garsuch, G. Semrau, M. Schmidt, et al. Amorphous columnar silicon anodes for advanced high voltage lithium ion full cells: dominant factors governing cycling performance. *Journal of The Electrochemical Society*, 160(10):A1824, 2013.

[33] E. Markevich, K. Fridman, R. Sharabi, R. Elazari, G. Salitra, H. Gottlieb, G. Ger-

shinsky, A. Garsuch, G. Semrau, M. Schmidt, et al. Amorphous columnar silicon anodes for advanced high voltage lithium ion full cells: dominant factors governing cycling performance. *Journal of The Electrochemical Society*, 160(10):A1824, 2013.

[34] E. Markevich, G. Salitra, F. Chesneau, M. Schmidt, and D. Aurbach. Very stable lithium metal stripping–plating at a high rate and high areal capacity in fluoroethylene carbonate-based organic electrolyte solution. *ACS Energy Letters*, 2(6): 1321–1326, 2017.

[35] E. Markevich, G. Salitra, Y. Talyosef, U.-H. Kim, H.-H. Ryu, Y.-K. Sun, and D. Aurbach. High-performance linio2 cathodes with practical loading cycled with li metal anodes in fluoroethylene carbonate-based electrolyte solution. *ACS Applied Energy Materials*, 1(6):2600–2607, 2018.

[36] R. May, K. J. Fritzsching, D. Livitz, S. R. Denny, and L. E. Marbella. Rapid interfacial exchange of li ions dictates high coulombic efficiency in li metal anodes. *ACS Energy Letters*, 6(4):1162–1169, 2021.

[37] K. Marker, C. Xu, and C. P. Grey. Operando nmr of nmc811/graphite lithium-ion batteries: structure, dynamics, and lithium metal deposition. *Journal of the American Chemical Society*, 142(41):17447–17456, 2020.

[38] M. T. McDowell, S. W. Lee, W. D. Nix, and Y. Cui. 25th anniversary article: understanding the lithiation of silicon and other alloying anodes for lithium-ion batteries. *Advanced materials*, 25(36):4966–4985, 2013.

[39] M. Mehring. *Principles of high resolution NMR in solids*. Springer Science & Business Media, 2012.

[40] A. L. Michan, G. Divitini, A. J. Pell, M. Leskes, C. Ducati, and C. P. Grey. Solid electrolyte interphase growth and capacity loss in silicon electrodes. *Journal of the American Chemical Society*, 138(25):7918–7931, 2016.

[41] T. Nagaura. Lithium ion rechargeable battery. *Progress in Batteries & Solar Cells*, 9:209, 1990.

[42] B. Nguyen, S. Chazelle, M. Cerbelaud, W. Porcher, and B. Lestriez. Manufacturing of industry-relevant silicon negative composite electrodes for lithium ion-cells. *Journal of Power Sources*, 262:112–122, 2014.

[43] C. C. Nguyen and B. L. Lucht. Comparative study of fluoroethylene carbonate and vinylene carbonate for silicon anodes in lithium ion batteries. *Journal of the Electrochemical Society*, 161(12):A1933, 2014.

[44] C. C. Nguyen, T. Yoon, D. M. Seo, P. Guduru, and B. L. Lucht. Systematic investigation of binders for silicon anodes: interactions of binder with silicon particles and electrolytes and effects of binders on solid electrolyte interphase formation. *ACS applied materials & interfaces*, 8(19):12211–12220, 2016.

[45] M. Nie, D. P. Abraham, Y. Chen, A. Bose, and B. L. Lucht. Silicon solid electrolyte interphase (sei) of lithium ion battery characterized by microscopy and spectroscopy. *The Journal of Physical Chemistry C*, 117(26):13403–13412, 2013.

[46] M. Nie, D. Chalasani, D. P. Abraham, Y. Chen, A. Bose, and B. L. Lucht. Lithium ion battery graphite solid electrolyte interphase revealed by microscopy and spectroscopy. *The Journal of Physical Chemistry C*, 117(3):1257–1267, 2013.

[47] N. Nitta, F. Wu, J. T. Lee, and G. Yushin. Li-ion battery materials: present and future. *Materials today*, 18(5):252–264, 2015.

[48] V. S. Nysted. The galvanostatic intermittent titration technique for silicon-based li-ion battery anodes: theory and experimental validation. Master's thesis, Norwegian University of Life Sciences, Ås, 2020.

[49] K. Ogata, E. Salager, C. Kerr, A. Fraser, C. Ducati, A. J. Morris, S. Hofmann, and C. P. Grey. Revealing lithium–silicide phase transformations in nano-structured silicon-based lithium ion batteries via in situ nmr spectroscopy. *Nature communications*, 5(1):3217, 2014.

[50] V. Pop, H. J. Bergveld, P. Notten, and P. P. Regtien. State-of-the-art of battery state-of-charge determination. *Measurement science and technology*, 16(12):R93, 2005.

[51] D. Rovnyak. Tutorial on analytic theory for cross-polarization in solid state nmr. *Concepts in Magnetic Resonance Part A: An Educational Journal*, 32(4):254–276, 2008.

[52] J. Ryu, D. Hong, H.-W. Lee, and S. Park. Practical considerations of si-based anodes for lithium-ion battery applications. *Nano Research*, 10:3970–4002, 2017.

[53] S. Schweidler, L. De Biasi, A. Schiele, P. Hartmann, T. Brezesinski, and J. Janek. Volume changes of graphite anodes revisited: a combined operando x-ray diffraction and in situ pressure analysis study. *The Journal of Physical Chemistry C*, 122(16): 8829–8835, 2018.

[54] H. Sclar, O. Haik, T. Menachem, J. Grinblat, N. Leifer, A. Meitav, S. Luski, and D. Aurbach. The effect of zno and mgo coatings by a sono-chemical method, on the

stability of limn1. 5ni0. 5o4 as a cathode material for 5 v li-ion batteries. *Journal of the Electrochemical Society*, 159(3):A228, 2011.

[55] M. Sina, J. Alvarado, H. Shobukawa, C. Alexander, V. Manichev, L. Feldman, T. Gustafsson, K. J. Stevenson, and Y. S. Meng. Direct visualization of the solid electrolyte interphase and its effects on silicon electrochemical performance. *Advanced Materials Interfaces*, 3(20):1600438, 2016.

[56] A. Šmelko, J. Blahut, B. Reif, and Z. Tošner. Performance of cross-polarization experiment at conditions of radiofrequency field inhomogeneity and slow to ultrafast mas. *Magnetic Resonance Discussions*, 2023:1–28, 2023.

[57] S. Sturniolo, T. F. Green, R. M. Hanson, M. Zilka, K. Refson, P. Hodgkinson, S. P. Brown, and J. R. Yates. Visualization and processing of computed solid-state nmr parameters: Magresview and magrespython. *Solid state nuclear magnetic resonance*, 78:64–70, 2016.

[58] Y.-K. Sun, S.-T. Myung, B.-C. Park, J. Prakash, I. Belharouak, and K. Amine. High-energy cathode material for long-life and safe lithium batteries. *Nature materials*, 8 (4):320–324, 2009.

[59] K. Tan, M. Reddy, G. S. Rao, and B. Chowdari. High-performance licoo2 by molten salt (lino3: Licl) synthesis for li-ion batteries. *Journal of Power Sources*, 147(1-2): 241–248, 2005.

[60] A. Ulus, Y. Rosenberg, L. Burstein, and E. Peled. Tin alloy-graphite composite anode for lithium-ion batteries. *Journal of The Electrochemical Society*, 149(5):A635, 2002.

[61] C. A. Vincent. Lithium batteries: a 50-year perspective, 1959–2009. *Solid State Ionics*, 134(1-2):159–167, 2000.

[62] Y. Wang, M. Satoh, M. Arao, M. Matsumoto, H. Imai, and H. Nishihara. High-energy, long-cycle-life secondary battery with electrochemically pre-doped silicon anode. *Scientific reports*, 10(1):3208, 2020.

[63] M. S. Whittingham. Electrical energy storage and intercalation chemistry. *Science*, 192(4244):1126–1127, 1976.

[64] M. S. Whittingham. Lithium batteries and cathode materials. *Chemical reviews*, 104 (10):4271–4302, 2004.

[65] H. Wu and Y. Cui. Designing nanostructured si anodes for high energy lithium ion batteries. *Nano today*, 7(5):414–429, 2012.

[66] D. Xia, H. Jeong, D. Hou, L. Tao, T. Li, K. Knight, A. Hu, E. P. Kamphaus, D. Nordlund, S. Sainio, et al. Self-terminating, heterogeneous solid–electrolyte interphase enables reversible li–ether cointercalation in graphite anodes. *Proceedings of the National Academy of Sciences*, 121(5):e2313096121, 2024.

[67] K. Xu. Nonaqueous liquid electrolytes for lithium-based rechargeable batteries. *Chemical reviews*, 104(10):4303–4418, 2004.

[68] K. Xu. Electrolytes and interphasial chemistry in li ion devices. *Energies*, 3(1): 135–154, 2010.

[69] Z. Xu, J. Yang, H. Li, Y. Nuli, and J. Wang. Electrolytes for advanced lithium ion batteries using silicon-based anodes. *Journal of Materials Chemistry A*, 7(16): 9432–9446, 2019.

[70] H. D. Yoo, E. Markevich, G. Salitra, D. Sharon, and D. Aurbach. On the challenge of developing advanced technologies for electrochemical energy storage and conversion. *Materials today*, 17(3):110–121, 2014.

[71] H. D. Yoo, E. Markevich, G. Salitra, D. Sharon, and D. Aurbach. On the challenge of developing advanced technologies for electrochemical energy storage and conversion. *Materials today*, 17(3):110–121, 2014.

[72] Y. Yuan, K. Amine, J. Lu, and R. Shahbazian-Yassar. Understanding materials challenges for rechargeable ion batteries with in situ transmission electron microscopy. *Nature communications*, 8(1):15806, 2017.

[73] C. Zhang, Y.-L. Wei, P.-F. Cao, and M.-C. Lin. Energy storage system: Current studies on batteries and power condition system. *Renewable and Sustainable Energy Reviews*, 82:3091–3106, 2018.

[74] Y. Zhang, D. Krishnamurthy, and V. Viswanathan. Engineering solid electrolyte interphase composition by assessing decomposition pathways of fluorinated organic solvents in lithium metal batteries. *Journal of The Electrochemical Society*, 167(7): 070554, 2020.

[75] Q. Zhong, A. Bonakdarpour, M. Zhang, Y. Gao, and J. Dahn. Synthesis and electrochemistry of linixmn2- x o 4. *Journal of the Electrochemical Society*, 144(1):205, 1997.

[76] Q. Zhong, A. Bonakdarpour, M. Zhang, Y. Gao, and J. Dahn. Synthesis and electrochemistry of linixmn2- x o 4. *Journal of the Electrochemical Society*, 144(1):205, 1997.

[77] H. Zsiborács, N. H. Baranyai, A. Vincze, L. Zentkó, Z. Birkner, K. Máté, and G. Pintér. Intermittent renewable energy sources: The role of energy storage in the european power system of 2040. *Electronics*, 8(7):729, 2019.

[78] C.-X. Zu and H. Li. Thermodynamic analysis on energy densities of batteries. *Energy & Environmental Science*, 4(8):2614–2624, 2011.

[79] X. Zuo, J. Zhu, P. Müller-Buschbaum, and Y.-J. Cheng. Silicon based lithium-ion battery anodes: A chronicle perspective review. *Nano Energy*, 31:113–143, 2017.

List of Figures

List of Tables

Acknowledgements

I'd like to thank Dr. Katharina Märker for being my guide during these months at CEA, without her, none of this would have been possible. I'd like thank also for being the person believing in me since the first interview more than one year ago.

Vorrei sommamente ringraziare il prof. Rafael Omar Ferragut per aver accettato di essere il mio relatore, per avermi accompagnato in questo progetto e per essere sempre stato gentile e disponibile nonostante la distanza.

Un personale ringraziamento alla professoressa Maria Enrica Di Pietro per l'interesse nei confronti del mio progetto e aver accettato di essere la mia controrelatrice.

Un ringraziamento ai miei genitori per tutti i sacrifici fatti, per avermi insegnato i valori dell'umiltà, del lavoro e per il loro costante aiuto e supporto. Grazie.

Ringrazio Christian, artefice della mia stupidità, per essere sempre in grado di farmi ridere e aver condiviso assieme momenti indimenticabili (buonasera). Ringrazio Nicole per essere stata per me quasi una sorella, per avermi sempre sorretto nei momenti di difficoltà ed essere stata la prima a vedere "La svolta di Samu". Ringrazio Christian e Nicole per aver dato al mondo la piccola Bianca, sempre presente sulla mia scrivania pronta a farmi tornare il sorriso nei momenti di malinconia.

Grazie a te Lara. Tu che da anni ormai sei la persona con cui ho condiviso tutte le mie gioie. Tu che sai sempre schiarire le mie giornate. Un grazie alle domeniche assieme, ai viaggi, ai concerti, a tutte le nostre piccole cose. A te che mi hai sempre sostenuto in ogni momento, a te che hai sempre creduto in me. Senza di te tutto questo avrebbe alcun senso. Grazie a te Lara.

Un grazie a tutta la mia famiglia: nonno Bruno, nonna Marisa, nonna Capano, zio Mario, zio Dori, zia Nana, zio Alfre, zia Simona, Marta, Sara, Chiara, Gaia, Sara, Lorenzo, Sofia;

sempre interessati ai miei studi e a gioire assieme a me per i traguardi raggiunti

Caro Francesco, questo lavoro è dedicato a te. Tu che sei stato una delle migliori persone che abbia mai conosciuto. Sei sempre stato per me come un fratello. Abbiamo riso, scherzato e passato sempre dei momenti indimenticabili assieme. D'altronde il biliardo è anche questo.

Un ringraziamento ai miei amici da una vita: Teo, Noah, Ste, Pippo, Mala. Alle serate al GP, alle grigliate, alle cene assieme, al Rebel, allo Scorpion. Momenti incredibili, fondamentali per tirarmi su di morale durante le interminabili sessioni d'esame.

Un ringraziamento ai miei compagni colombiani: Mevar, Anto, Papi, Fufo, Filo, Franci, Bucco. Compagni di viaggio incredibili durante questi sei mesi a Grenoble.

Un ringraziamento a tutti i miei amici dell'università, al Team Mexico, al Team Panama, al Team Lazarus, alla macchinata Portenlo per avermi fatto trascorrere 5 anni incredibili tra le pause pranzo al porchetto, le ore di progetto da consigliere, viaggi della speranza per Grenoble

Un grazie a Paolo, Simona, Michele, Edvige per essere sempre stati miei sostenitori per tutti questi anni di università.

I'd like to thank all people from NMR LAB at CEA:Gaël, Sabine, Katharina, Paul, Pierre-Alain, Tamali, Quentin, Lana, Ankan, Zoe, Stasa, Nico; for the countless joyful and funny moments at the canteen, in the office and all unforgettable FooDNPub nights together. Bravo!

Un grazie a Mattia e ai suoi coinquilini Francesca, Ana e Alberto per i giovedì sera post calcetto. Grazie a voi, le sconfitte del calcetto si sono sempre trasformate in serate passate a ridere assieme.

Un grazie a Rudy, sempre presente durante le sessioni di studio, sempre lì a tenermi compagnia durante le lezioni a distanza.